EXAMINATION OF CORONAL LOOPS BETWEEN QUIESCENT ACTIVE REGIONS

by

Marika Isabel McCarthy

A dissertation submitted in partial fulfillment
of the requirements for the degree

of

Doctor of Philosophy

in

Physics

MONTANA STATE UNIVERSITY
Bozeman, Montana

July 2021

©COPYRIGHT

by

Marika Isabel McCarthy

2021

All Rights Reserved

DEDICATION

To Mom, Dad, and Liam.
And for my Nanny Annie.

ACKNOWLEDGEMENTS

To my advisor, Professor Dana Longcope. I have been grateful to have received outstanding mentorship, and to have been intellectually challenged throughout my graduate career.

And to Dr. David McKenzie, for selecting me for the 2015 Montana State Solar Physics REU. Thanks to you, I am a Sun scientist.

The data used herein were products of the SDO and STEREO missions and obtained with the Virtual Solar Observatory.

This work was supported in part by NASA's HGI program.

TABLE OF CONTENTS

1. OVERTURE 1

1.1 The Sun: A Primer 2
1.1.1 Solar Interior 3
1.1.2 Solar Atmosphere 4
1.2 Sunspots 6
1.3 Active Regions and Coronal Loops 8
1.4 Magnetic Reconnection 11
1.4.1 Interacting Active Regions 13
1.5 Thematic Overview 13

2. MEASURING AND MODELING THE RATE OF SEPARATOR RECONNECTION BETWEEN AN EMERGING AND AN EXISTING ACTIVE REGION 18

2.1 Introduction 21
2.2 Potential Field Model 24
2.3 Interconnecting Flux Evident in AIA 30
2.3.1 Cataloging Coronal Loops 32
2.3.2 Loop Properties 36
2.4 Nonpotential Force-free Field Modeling 41
2.5 MCT Model with Nonzero Twist 47
2.6 Loop Locations in the Plane Defined by the Slit and the Line of Sight 49
2.7 Discussion and Conclusions 52

3. MULTISPACECRAFT OBSERVATIONS OF CORONAL LOOPS TO VERIFY A FORCE-FREE FIELD RECONSTRUCTION AND INFER LOOP CROSS SECTIONS 56

3.1 Introduction 59
3.2 Data Set Acquisition 62
3.3 Alignment of Model with Data 64
3.4 Qualitative Comparison of Tracks to EUVI Images 67
3.5 Quantitative Analysis of Loops Using Gaussian Fitting 74
3.5.1 Methodology 75
3.5.2 Centroid 82
3.5.3 FWHM 82
3.5.4 Diameter and Intensity Comparison 88
3.6 Conclusions and Outlook 91
3.7 Acknowledgments 94

TABLE OF CONTENTS – CONTINUED

4. TEMPERATURE EVOLUTION OF CORONAL FLUX OBSERVED THROUGH MULTIPLE EXTREME ULTRAVIOLET WAVELENGTHS 95

4.1 Motivation and Background 98
4.2 Data Set Compilation 100
4.2.1 Synthetic Emission Measure Comparisons 102
4.3 Comparisons Across Passbands 107
4.3.1 Time Delay 113
4.3.2 Flux Budget Comparison 115
4.3.3 Brightness Trends 120
4.4 Discussion 125

5. CODA 127

REFERENCES CITED 130

LIST OF TABLES

Table Page

4.1 Properties of loops identified in each of the three band passes, as determined from the cataloging procedure. 108

LIST OF FIGURES

Figure Page

2.1 Line-of-sight magnetogram from which the quadrupolar MCT model is constructed, and subset of the subsequent magnetic domains 27

2.2 Fluxes determined from the MCT model 28

2.3 An image from SDO/AIA showing the active regions of interest with virtual slit location overlaid 31

2.4 Time/space stack plot built from the virtual slits extracted from AIA images 33

2.5 Local maxima identifier used for rows in the stack plot with results plotted on top of an EUV image 34

2.6 Histograms denoting the properties of the 205 loops interconnecting the two ARs 37

2.7 Integrated reconnection electric field 38

2.8 A 3D rendering of loops reconstructed from LFFF models 42

2.9 Histogram of α values for all loops obtained through the LFFF models 45

2.10 Magnetic field strengths obtained from the LFFF models 45

2.11 Flux plot with interconnecting loop flux added 46

2.12 Comparison of interconnecting flux for various values of α 48

2.13 Locations of loops where they cross the plane of the virtual slit with resulting hot spots 50

2.14 Locations of the separatrix (MCT model) and loops (LFFF model) from similar times 51

2.15 Locations of loops crossing the virtual slit plane binned by time 52

3.1 Example depicting how cataloged loops (AIA data), α-h fits, and STEREO data are related 63

3.2 Image from AIA showing a selection of α-h fits overplotted 63

LIST OF FIGURES – CONTINUED

Figure Page

3.3 Schematic of the α-h fits in the tangent plane approximation and the deformation applied to map the rectilinear box's lower boundary to the solar surface 66

3.4 Example image from EUVI-A with tracks overplotted 69

3.5 Example image from EUVI-B with tracks overplotted..... 69

3.6 Example of tracks assigned to the excellent match category 71

3.7 Example of tracks assigned to the maybe match category 72

3.8 Example of tracks excluded from visual analysis..... 73

3.9 Example 1 76

3.10 Example 2 77

3.11 Method of obtaining loop diameters along (and informed by) the track..... 79

3.12 An example Gaussian fit using the edges identified using the method shown in Figure 3.11 79

3.13 Comparison of the method in this work to that of interpolating along a line to "straighten" the loop 81

3.14 Analysis of Example 1 83

3.15 Analysis of Example 2 83

3.16 Analysis of one track/loop observed with EUVI-A, EUVI-B, and AIA simultaneously 84

3.17 Anticorrelated behavior between intensity and diameter for Example 1 89

3.18 Comparison of loop lengths between this work and Klimchuk & DeForest (2020)..... 90

4.1 Temperature response functions of the passbands of AIA.....103

4.2 Characteristics of emission peaks identifying loops in each wavelength.....105

LIST OF FIGURES – CONTINUED

Figure Page

4.3 Histogram of observed and synthesized intensities as would be observed in 193 Å 106

4.4 Time-space stack plot showing all cataloged loops 109

4.5 Examples of morphological differences 111

4.6 Labeling schema of the active regions' polarities and schematic of morphological trends 112

4.7 Flux budget comparison with characteristic B 117

4.8 Voltage trends 118

4.9 Brightness trends of the 171 Å data 121

4.10 Brightness trends of the 193 Å data 122

4.11 Brightness trends of the 211 Å data 123

4.12 Comparison of the brightness fraction and brightening rate across all three band passes 124

ABSTRACT

Active regions are dynamic and constantly evolving portions of the Sun, where the magnetic field emerges from beneath the solar surface and expands into the corona. Hot, dense plasma is aligned to these field lines and these brightly emitting structures are called coronal loops. These loops are the direct manifestations of solar magnetic fields, and thus observations of them can be used to investigate the structural evolution of the corona. As an active region is believed to be a single, isolated magnetic system, any flux linkage between multiple active regions must be formed in the corona post-emergence. Direct observations of new loops can provide evidence of this when using a two-active region system as a laboratory. Loops in such a system were examined in a variety of ways. First, interconnecting loops between two active regions over a 48-hour period were cataloged, testing the assumption that all interconnecting loops are new instance of flux linkage. The flux was significantly over-counted, which could be attributed either to the modeling technique used therein or the assumed structure (e.g., cross-sectional shape) of the loops. Both of these possibilities were tested by supplementing the catalog with data from a second observational line-of-sight (LOS). The results of this study contends that some loops have non-circular cross-sections, and some might even be less structured such that they do not have enough emission along the second LOS to be observed. Another possible reason for the overcounting of flux could be attributed to a loop brightening multiple times. We test this by looking at properties of loops from the same interconnecting region, but observed in different temperatures.

CHAPTER ONE

OVERTURE

The Great American Eclipse in August 2017 took place in the week between sitting for my written comprehensive exam and learning the results. While sitting on a rooftop in Jackson, WY almost two decades into the new millennium, I felt a distinct kinship to the long-gone observers of the Sun since time immemorial. I, too, was an observer of solar atmosphere in all of its brilliance, accompanied by a cacophony of sound swelling from birds who could not comprehend why night was falling in the middle of the day. I left the experience with the profound appreciation that — as the glint of Baily's beads indicate the Sun will emerge from behind the Moon — that the Sun will rise tomorrow and the next day, and the next, ad infinitum. And how lucky I was, to be becoming a Sun scientist.

Totality of a total solar eclipse, wherein the disk of the Moon obscures the Sun such that the observer is entirely within the Moon's shadow, provides the rare opportunity to see the Sun's atmosphere by those on Earth. It appears to the naked eye as a bright, glowing halo extending out to several solar radii. The Spanish astronomer José Joaquín de Ferrer, from his observations of the 1806 Solar Eclipse from Kinderhook, NY, concluded that this structure was part of the Sun rather than the Moon. Perhaps more influentially, in his description of the bright solar atmosphere as the *luminous corona* from the Latin word meaning crown, de Ferrer named the Sun's atmosphere[1] (de Ferrer, 1809; Vaquero & Vázquez, 2009).

The corona, however, it is not merely a diffuse, glowing orb; it has structure. That structure is ever evolving, waxing and waning in proportion to the magnetic activity of the

[1]Staring in the spring of 2020, however, connotations of the word *corona* have morphed to take on a new meaning, thanks to the novel coronavirus responsible for the COVID-19 pandemic.

Sun (Carroll & Ostlie, 2017; Lang, 2001). In accounts of eclipse observations during the era of the Maunder Minimum (1645–1715) — a time in which there is evidence for a lack of solar magnetic activity — there is also a lack of reported structure observed within the corona (Eddy, 1976). Magnetism is at the heart of solar processes, manifesting in many forms, and extending throughout various spatial and temporal scales.

Much has changed since the observations of de Ferrer[2], allowing modern solar astrophysicists to work on finer spatial and time scales than ever before. The development of observational and modeling techniques have enabled the investigation into many different questions about our nearest star, and with finer detail than in the era in which the eye or Galilean telescopes were an astronomer's primary tools. The work herein uses adjacent active regions as the laboratory in which we seek insight about activity on the Sun, and the mechanisms that may be driving them. Specifically, this is done through observations of the building blocks of the solar atmosphere, called coronal loops. The aim of this introduction is to give the reader an understanding of both this work's title and general solar physics background, before clearly defining which questions we wish to answer — and assumptions we wish to challenge — through the subsequent chapters.

1.1 The Sun: A Primer

The Sun is a G-type main-sequence star at the center of our solar system (Carroll & Ostlie, 2017). It has bathed our planet in light since the dawn of time. The impact the Sun has on daily life cannot be overstated — including the very delineation of what constitutes a day. It is easy to conclude from stepping out of the shade, that the Sun provides energy — one can feel the warmth on one's skin. Further, this energy that the Sun provides leads to a whole host geophysical phenomena. It is the intimately intertwined nature of the Sun-Earth

[2]De Ferrer himself had much improved technology contemporarily, in comparison to ancient observatories like Stonehedge (Hawkins, 1963)

connection, as well as the relative ease with which it can be observed, that has continued to drive humankind's need to understand the Sun.

When thinking about its general structure, the Sun can be primarily divided into two regimes: the interior and the atmosphere. As magnetism is the primary driver of solar activity (Priest & Forbes, 2000; Schrijver & Siscoe, 2009), we shall follow it throughout the solar structure, and note some of its particular manifestations. Within the interior, the magnetic field is created. After, the field then breaches the surface into the atmosphere. Eventually the magnetic field extends beyond what we think of as the Sun. It stretches into the solar wind, heliosphere, and beyond into the interstellar medium (Lang, 2001; Schrijver & Siscoe, 2009).

1.1.1 Solar Interior

The origin of the solar magnetic field — and that of stars like it with an inner radiative zone surrounded by an outer convective zone — begins within the star itself (Rempel, 2009). It is widely accepted that there is a dynamo responsible for generating the large scale magnetic field (Phillips, 1995; Priest, 2014). Motion of an electrically conducting fluid is converted to magnetic energy (Phillips, 1995). The inner workings of the dynamo have historically been hard to investigate, as photons are unable to escape from these depths. As a result, we are unable to make direct observations of what is hidden within. A simplistic explanation about the basic ingredients for the solar dynamo involves differential rotation, wherein the plasma at the poles rotate slower than that at the equator (Carroll & Ostlie, 2017). The solar interior is a regime in which magnetic fields are dragged along by plasma motion (Gary, 2001; Priest, 2014). As a result, the field is deformed unevenly, leading to stretching and twisting of the field. Much like the twisting of a rubber band increases the tension, so too does the magnetic field strength increase with stretching and twisting as well (Rempel, 2009). More recently, work in the field of helioseismology has used oscillations

to probe new depths within the Sun. This revealed a shear layer between the radiative and convective zones called the tachocline (Spiegel & Zahn, 1992). This layer was of much interest for years, as many subscribed to the belief that it was at the tachocline where dynamo generation occurs (Carroll & Ostlie, 2017; Charbonneau, 2020; Priest, 2014). In recent years, however, a series of new conclusions have caused doubt to be cast onto whether the tachocline is an essential part of the Sun's magnetic field generation (Charbonneau, 2020).

Regardless of the mechanisms of their generation, magnetic fields are generated within the Sun. We are able to observe the effects they take as they emerge from the interior. These flux tubes generated by the dynamo are confined by the pressure around them. Thus, we can consider a flux tube as its own system, with no interaction with others that might exist concurrently within the solar interior. Flux tubes are also buoyant, and rise to breach the surface into the solar atmosphere (Fan, 2009).

1.1.2 Solar Atmosphere

The atmosphere of the Sun begins at its surface, called the photosphere. The photosphere is not a true surface, like the surface of the ocean or *terra firma* on Earth. However we call this the solar surface because this is the lowest altitudes from which emitted light can be observed. This is a very thin shell, having a pressure scale height of ~ 200 km. One might be skeptical of calling this a "thin" shell, but when compared to the solar radius ($\sim 700,000$ km), its relative thinness becomes apparent in context. This region becomes optically thin, meaning it is from these radii where photons can escape and make it to us for observation (or to other places of detection, like space-based telescopes; Carroll & Ostlie, 2017). The photosphere radiates like a black body with an effective temperature

of approximately 6000 K (Phillips, 1995). It is the brightest part of the Sun[3](Vaquero & Vázquez, 2009). Thus, observing the fainter parts of the atmosphere necessitates some obscuration. This can be done either physically (e.g., as in an eclipse, from the moon) or otherwise, as in through wavelength filtering.

The predominant driver of activity in the photosphere is convective motion, manifesting as an ever evolving pattern of granulation across the Sun's surface (Carroll & Ostlie, 2017; Phillips, 1995; Priest, 2014; Schrijver & Siscoe, 2009). The pattern is made up of individual granules, the tops of rising convective cells of hot gas, with dark downflow lanes between them (Phillips, 1995). The first data released from the ground-based Daniel K. Inouye Solar Telescope (DKIST) on the summit of Haleakalā on Maui, HI in January 2020 unveiled the highest resolution images of the Sun's surface and its granulation ever taken (National Solar Observatory, 2020).

Above the photosphere comes the chromosphere and transition region (Carroll & Ostlie, 2017; Priest, 2014). Through these layers, the density of the atmosphere decreases and, paradoxically, the temperature increases with height (Carroll & Ostlie, 2017; Schrijver & Siscoe, 2009). While the work herein does not focus within these particular layers, the advent of the DKIST will allow scientists to probe these regimes in new ways with unprecedented resolution.

The corona marks yet another new regime of the solar atmosphere. This outermost layer ultimately extends into the solar wind, which bathes the solar system in a stream of charged particles (Lang, 2008). Interactions of the solar wind throughout the solar system (and especially involving the Earth) is a field known as space weather. This connection can manifest, for example, as aurorae (Carroll & Ostlie, 2017). The solar wind eventually extends to the edge of our heliosphere, where it reaches the interstellar medium (Schrijver

[3]Due to surface brightness in combination with the astronomical objects they study existing far away, stellar astronomers consider a star's atmosphere synonymous with its photosphere.

& Siscoe, 2009). New missions like the Parker Solar Probe (PSP, launched August 2018) and Solar Orbiter (SO; February 2020) seek to make new, *in situ* measurements of the outer corona and solar wind. Between these missions and others, the solar wind has been studied from ~ 0.1 AU (PSP) to over 100 AU (Voyager 1 and 2, launched 1977).

The density and temperature trends from the chromosphere and transition region continue in the corona. In fact, the coronal plasma reaches temperatures of millions of kelvin, driving many inquiries into the mechanisms of the "coronal heating problem" (Klimchuk, 2006; Lang, 2008). But this regime is also markedly different from both those below it and the solar wind at higher altitudes: here in the corona, the magnetic pressure dominates over the plasma pressure and the magnetic field is no longer beholden to the convective whims of plasma. Now it is the field that plays shepherd, constricting the plasma along it.

1.2 Sunspots

Perhaps the most well-documented solar features throughout history are sunspots. These are dark mottles that appear on the photosphere, consisting of a dark penumbra ringed around the even darker umbra (Priest, 2014). Definitive historical accounts of such features exist dated as early as 165 BC from China (Phillips, 1995; Priest, 2014; Wittmann & Xu, 1987). Galileo is the most well-known observer of sunspots, among the first to use a telescope to make careful observations of such features and record them in a series of drawings (Vaquero & Vázquez, 2009). Since then and into modernity, there exists a record — albeit one that is patchy at times — detailing sunspots as they traverse the solar disk (Muñoz-Jaramillo & Vaquero, 2019). The historical record allows for contemporary, so-called astroarchaeologists to use these drawings to draw conclusions about the Sun as it was in the past (as in Hayakawa et al., 2020, for example). Such records also reveal a variation in sunspot prevalence over time, with number of sunspots being a strong indicator of solar activity that occurs on a cycle of about 11 years (Hathaway, 2015; Solanki, 2003).

In the first "butterfly diagram" — named for the apparent shape the data takes — Maunder (1904) showed the evolution of sunspot locations throughout the solar cycle, from high to low latitudes.

Hale (1908) first drew the conclusion that sunspots were strongly magnetized, and further were the first astronomical objects found to contain magnetic fields (Solanki, 2003). Using the facilities at the Mount Wilson Observatory, Hale capitalized on the Zeeman effect — spectral line splitting in the presence of magnetic field — to make this deduction (Hale, 1908; Zeeman, 1897). He went on to find that sunspots appear in pairs of opposite magnetic polarities. Within these bipolar regions is a leading (i.e., in the direction of solar rotation) polarity and trailing polarity of the opposite sign. The leading polarity's sign differs between the northern and southern hemispheres (van Driel-Gesztelyi & Green, 2015). Further, when taking the magnetism of sunspots into account, the solar cycle becomes twice as long to include the polarity reversal of the Sun. This is apparent in the switch of the leading polarity's sign (van Driel-Gesztelyi & Green, 2015). Both the hemispheric dependence on the sign of the leading polarity and the reversal after a solar cycle are encompassed in what is called *Hale's law* (Hale & Nicholson, 1925; van Driel-Gesztelyi & Green, 2015). The polarities are oriented primarily along the same line of latitude, though the leading spot is in general slightly closer to the solar equator in both hemispheres (Joy's law; Hale et al., 1919; van Driel-Gesztelyi & Green, 2015).

Through improved observational means over the past century, we are able to make magnetic maps of the photosphere (as with the Helioseismic Magnetic Imager, HMI; Scherrer et al., 2012). With this advancement, the scientific community is no longer reliant on only a sunspot observation in optical wavelengths to determine these areas of strong magnetic fields. In these maps, the sunspot might exist with a larger region that is magnetically active, referred to as an active region (AR; Priest, 2014; van Driel-Gesztelyi & Green, 2015). It is within these ARs that arguably give rise to some of the most interesting of solar phenomena.

1.3 Active Regions and Coronal Loops

The existence of bipolar ARs is widely accepted to be a result of the buoyant flux tubes created in the convection zone emerging from within the Sun (Moldwin et al., 2009; van Driel-Gesztelyi & Green, 2015). A portion of the tube — much like a bight of rope — now lives in the atmosphere. The locations where the flux intersects the photosphere are the areas where the magnetic polarities are strong. The corona above an AR is rife with activity due to these strong magnetic fields. Once a flux tube makes the transition from the interior to the atmosphere, it is no longer confined due to the pressure of the plasma around it (Fan, 2009). Much like the petals of a flower unfurl as it opens, so too does the field dynamically expand into the corona. As previously mentioned, the corona is distinct from other layers in that the plasma is confined along the magnetic field lines. Thus, at least for the corona, the magnetic field and the plasma aligned to it can be considered one and the same. As a result, these "coronal loops" are the direct manifestation of magnetic fields in the solar atmosphere. These can be thought of as the building blocks of an AR (Rosner et al., 1978).

While the Earth's atmosphere protects those within it from harmful, high-energy radiation, it is in those wavelengths (primarily in extreme ultraviolet (EUV) and x-ray) where the hot, coronal plasma can be best observed. Mankind's voyage into space has enabled a new age of space-based instrumentation. The first forays into observations taken from higher in Earth's atmosphere used sounding rockets, especially in x-ray wavelengths (Golub & Pasachoff, 1997; Vaiana et al., 1973). The advent of satellite-based observing missions (including Skylab, 1973; Yohkoh, 1991; SoHO, 1995; TRACE, 1998; SDO, 2010; STEREO, 2006; and others; Domingo et al., 1995; Handy et al., 1999; Kaiser et al., 2008; Lemen et al., 2012; Reeves et al., 1972; Tsuneta et al., 1991) have enabled an ever increasing amount and quality of data taken of ARs and the loops of which they are comprised. Advancements have not been limited to satellites: modern sounding rocket flights, like that of the High-

resolution Coronal Imager (Hi-C, Kobayashi et al., 2014; Rachmeler et al., 2019), have taken data with very high resolution. The abundance and quality of modern coronal observations can enable understanding of its structural properties and evolution, as well as the underlying mechanisms responsible.

The initial picture of these coronal building blocks come from observations in soft x-ray wavelengths (emission produced at temperatures greater than 2 MK), and were of a steadily heated, long-lived structure which satisfied static equilibrium scaling laws (Klimchuk, 2009). Observations in the relatively cooler EUV wavelengths (formed at $T \sim 1$ MK) brought forth that — though they exist at the same places the x-ray loops do — the properties of EUV loops are fundamentally different (Klimchuk, 2009). This discrepancy illustrates that the foundational aspects of coronal loops are more complex than first hypothesized.

As a result of the corona being optically thin, observers receive diagnostic information about the emitting plasma integrated along the observational line of sight (LOS). To make observation of these structures even more complicated, loops tend to overlap along the LOS within these bustling ARs. Observations of loops are also somewhat limited by the the instruments used to observe them. By choosing a specific wavelength around which to center an instrument's band pass, there is a natural selection bias that partitions loops by temperature. Due to these difficulties, it can be challenging to extrapolate whether properties inferred from one study are widely applicable to loops at large — whether the challenges are posed by limited sampling, or by selection effects within the data sets of individual studies (Reale, 2014). Generalizing results of loop studies can also be difficult as a result of not knowing what composes a coronal loop foundationally.

It would be easy to conceptualize a coronal loop as a monolithic structure (e.g., not composed of finer elements and behaving as one object), given the prevailing understanding that the loop is composed of coronal plasma aligned to a field line. However, this idea is disputed on the basis that observed cooling behavior is not consistent with this assumption.

Loop lifetimes (i.e., the amount of time they are visible) have been observed for time periods longer than the loop's theoretical cooling time (as in López Fuentes et al., 2007; Winebarger et al., 2003, among others). Were loops monolithic (and assuming they are heated impulsively; Klimchuk, 2015), their lifetimes and cooling times would be similar. This discrepancy lends support to the hypothesis that a single loop is composed of thin strands that have scales below current instrument resolution capabilities (Klimchuk, 2009; Reale, 2014).

Though it is hard to make sweeping generalizations of the properties of these building blocks, there are some common assumptions that permeate the field. Loops have been observed to have an arch shape, with lengths that span two orders of magnitude (Reale, 2014). Their high luminosity is a result of the confined plasma, which creates a density enhancement along the magnetic field. The conservation of magnetic flux (Priest & Forbes, 2000) along a loop's length leads to the expectation of cross-sectional expansion with height. That is, as the magnetic field strength weakens with altitude, the cross sectional area (i.e., diameter) of the flux tube should get larger to preserve the flux along its length. This expected phenomenon, however, is not well-observed. Studies have found that a loop's apparent diameter does not vary strongly along its length (i.e., with changing altitude; see Klimchuk et al., 1992; Watko & Klimchuk, 2000). This has been cited as evidence for loop cross sections being approximately circular. Recently, work from Malanushenko & Schrijver (2013) has called this common assumption of cross-sectional shape into question. This has brought forth new studies interested in elucidating the shape of coronal loop cross sections, with varying degrees of support for circularity (Klimchuk & DeForest, 2020; Kucera et al., 2019; McCarthy et al., 2021).

The convective motion at the photosphere induces change throughout the active region by dragging around the polarities, at which coronal loops are anchored. These locations are known as the loop's footpoints, or feet. This motion manifests in flux cancellation —

annihilation of positive and negative surface polarities, perhaps by a submerging loop — and dispersion of the AR (van Driel-Gesztelyi & Green, 2015). The magnetic field of the corona and the loops that comprise it then react in response. Constant evolution — both at the photosphere and, consequently, higher in the atmosphere — makes these regions dynamic.

1.4 Magnetic Reconnection

It is not a large logical leap to conclude that an evolving region of magnetic complexity would be home to a plethora of activity. It has been mentioned previously that an AR is such a place. The coronal plasma above an AR is highly conductive. Though the plasma is composed of charged particles, electrostatic fields in this regime are dissipated quickly, on the order of a plasma period (Longcope, 2017). As a result of its conductivity, field lines move with the plasma's motion as if they are frozen within the fluid (Alfvén, 1942; Priest & Forbes, 2000). This is called Alfvén's theorem, or the frozen-in flux condition. This idea can be extended from individual field lines to some closed curve in space that moves with the plasma (Longcope, 2009; Rempel, 2009). Because the field lines contained within the boundary are preserved under the closed curve's deformation, the changes of its surface area and the strength of the magnetic field within it are intimately related. It is this conservation of flux that is believed to be responsible for loop expansion with height, as mentioned in Section 1.3. For an infinitely conductive plasma, this frozen-in condition would disallow any change in field line configuration. However, coronal loops (which we have mentioned are the building blocks of the corona, and the manifestation of the coronal field) are observed to evolve in a variety of ways. This is not to mention various other activity that takes place concurrently on the Sun. Therefore, there must be some process driving the evolution of the corona. For the rapidly evolving structure of the coronal field, the proposed mechanism is called magnetic reconnection.

Reconnection is commonly cited as an explanation for various types of solar activity.

At its inception, the idea was proposed by Sweet (1958) to explain solar flares, which are the most energetic events in our solar system (Carroll & Ostlie, 2017). Though electrostatic fields are screened out quickly, motion of the plasma in conjunction with the frozen-in condition can lead to inductive electric fields (i.e., Faraday's law of induction; Jackson, 1998). These electric fields persist for long enough for field lines to be broken and rearranged (Priest & Forbes, 2000). At present, reconnection is still not fully understood due to its complexity. However, the mechanisms that underly this hypothesized explanation continually undergoes refinement and is widely used in describing solar phenomena — and, to a larger extent, astrophysical magnetic phenomena in general — at various scales. Flares have been previously mentioned to be a high-energy process for which reconnection is deemed to be responsible. However, reconnection is also hypothesized to be behind relatively small, impulsive heating events called nanoflares. Nanoflares are used in the context of coronal loops to explain how individual loops (or even the corona as a whole) can be heated (Klimchuk, 2006). As such, there are a variety of different types of situations in which we can examine the process of magnetic reconnection.

Magnetic reconnection changes the topology of field lines, and as a result, releases the magnetic energy into other forms like kinetic or thermal (Priest & Forbes, 2000). Topological equivalence is, in essence, when two things can be continuously deformed until they become the same (Messer & Straffin, 2006). (A common example is a donut and a coffee cup: both can be deformed into a torus, as they each have one hole.) For our purposes, we can consider two field lines topologically equivalent if the feet of one are anchored at the same locations as the other. These loops belong to the same sub-volume, called a magnetic domain (Longcope, 2005). Further, a field line would undergo topological change (i.e., be reconnected) if one (or both) of its footpoints were to change the flux concentration — and thus, change the photospheric location — at which it was anchored. As a result of reconnection, the field line changes topologically and thereafter occupies a new domain. Longcope et al. (2020)

reported evidence of loop formation at topological boundaries (i.e., the boundaries between different domains). Therefore, reconnection can be further examined through identification of loops in a particular sub-volume of the corona, where the particular domain is being newly populated. An AR pair provides an ideal laboratory for such investigations.

1.4.1 Interacting Active Regions

Though an AR is believed to be a discrete magnetic system, it does not evolve in isolation (van Driel-Gesztelyi & Green, 2015). Post emergence, the new flux must be incorporated into the existing coronal field, hypothesized to be a result of reconnection (Fan, 2009). Tarr et al. (2014) investigated such evolution of a solitary AR to infer the reconnection rate within. Analysis of that type of environment can be troublesome, due to the difficulty in distinguishing new flux from old.

A different laboratory in which the incorporation of new AR flux into the corona can be examined is within adjacent AR pairs. Particularly, in a new AR emerging adjacent to an existing one. Under the common assumption that each AR is itself a distinct flux tube, the two are thus magnetically independent from each other. While submerged within the solar interior, the surrounding plasma pressure confines these flux tubes. The new flux linkage must occur, therefore, from reconnection in the corona post-emergence. After which, there now exists coronal magnetic field lines between these two systems. The newly formed field lines can therefore directly be observed in the form of coronal loops. It is the investigation into interconnecting loops between AR that we will now detail.

1.5 Thematic Overview

The advent of modern solar observations have allowed for closer studies of our closest star. As with any avenue of scientific inquiry, probing deeper to answer questions inevitably opens the door for further exploration. The work herein uses a specific pair of adjacent active

regions as a laboratory in which to examine coronal loops and their subsequent properties. The examination of this two-AR system is done using a variety of approaches, informed and driven by puzzling prior results and the desire to explore those further. This kind of investigative saga gives a depth of knowledge about one specific system. These results can be compared to the breadth of knowledge of other studies of coronal loops in ARs, to give a fuller picture of the solar atmosphere.

The adjacent AR emergence event with which we are concerned happened over an approximately 48-hour period of time, from 2011 January 20-22, as NOAA AR11149 (new) emerged to the south of AR11147 (old). As the new region emerges, the pair rotate across 0° longitude in the northern hemisphere. The approximate latitudinal extent of the pair was from 20°–35° north. The longitudinal extent of the pair (approximately 40°) was determined from the width of larger, older AR11147. Throughout the event, the flux of the old AR remained balanced in both the leading, negative polarity, and the positive, trailing one. The aggregate strength of each polarity was roughly constant at $\pm 5 \times 10^{21}$ Mx. The new AR initially emerges at a rate of about 3.47×10^{16} Mx/s. It seems to have a series of new flux emergences over the 48-hr interval. At the end of the event, the aggregate strengths of the new AR's polarities are essentially the same as the old region's. The year 2011 was amidst the rising phase of Solar Cycle 24 (Space Weather Prediction Center).

Chapter 2 first uses the AR pair in order to establish a catalog of interconnecting loops, using EUV observations in 171 Å from the Atmospheric Imaging Assembly (AIA) aboard the Solar Dynamics Observatory. Through this, we not only catalog the loops themselves, but also capture a selection of their properties. Then, we establish a modeling framework, allowing the extraction of more sophisticated information that cannot be obtained from observations alone. At the intersection of the model and observation, we are able to infer reconnection rates and measure the interconnecting flux.

The findings within Chapter 2 contend that the interconnecting magnetic flux is

overcounted. That is, more flux was found within this domain than was available to populate this region. Reasons for this conclusion could be attributed to a variety of sources, all of which were ripe for further study. For example, Chapter 2 used the magnetic field strength of each loop from the magnetic model fitting, in conjunction with cross sectional areas inferred from loop diameters in observation. There exists the possibility that the model framework — while it seemed accurate throughout the processes in which we fit our loops — is somehow faulty, leading to large magnetic field strengths. Or, perhaps cross sections are not circular, as commonly assumed, but are misshapen. Further, this work was conducted under the assumption that a loop becomes bright when it is first reconnected to populate the interconnecting region. We previously only mentioned reconnection in the context of a topological change. Simplistically, we distilled each loop to belonging to either the old AR, new AR, or the domain between them. In this way, we called all the loops in the interconnecting region topologically equivalent. In reality, the topology of the field is much more complex. It is possible there is reconnection (topological change) that occurs within what we called the interconnecting region, such that a loop's footpoint locations change yet still lives in this interconnecting region. Thus, we would be counting "old" flux as newly reconnected. This miscounting of loop flux could also happen if a loop were to be brightened multiple times, perhaps through some relaxation process that brings the loop to a lower energy state.

The possibilities of inaccurate modeling and of non-circular cross sections are tested in Chapter 3. Through the use of a second LOS with which to examine the AR pair (provided by the STEREO mission and the EUVI instrument aboard each of these twin spacecraft) and the data set of the three-dimensional magnetic models from Chapter 2, both the fitting fidelity is tested and the diameters of these loops are examined stereoscopically. The fitting accuracy is found to be in good agreement with the data from the second LOS: approximately 70% of our fitted loops match to underlying features in the EUV image. We also find evidence

in support of some loops exhibiting characteristics that we call consistent with elliptical cross sections, lending support to a relatively new idea of anisotropic loop expansion proposed by Malanushenko & Schrijver (2013). Observational support for such loop anisotropy has, up until now, been either inconclusive or in opposition to the idea (Klimchuk & DeForest, 2020; Kucera et al., 2019). We further provide validation of the fitting method utilized in Chapter 2 by proposing that perhaps the "missing" 30% of models in this work have such anisotropic expansion that there is not enough of a density enhancement (brightness), and as a result these particular loops cannot be observed from the second viewpoint.

Both Chapter 2 and Chapter 3 use only 171 Å wavelength observations of the AR pair. Chapter 4 looks through multiple AIA passbands in an effort to investigate the last reason proposed in this section for flux overcounting: By looking through multiple wavelengths — and therefore, through multiple temperatures — successive brightenings of a single loop are sought. A proposed mechanism for coronal loop heating (brightening) is through nanoflares. If a nanoflare were to exist, then we expect it to behave similarly to a conventional flare observation. Thus, we look for signatures that have been observed commonly in flare scenarios. Namely, we look for a loop to be cooling through subsequently cooler and cooler temperatures. (We hypothesize the impulsive heating phase occurs, as we do not currently have the resolution to observe it.) While other studies seek to examine cooling through the usage of light curves, the work herein uses whole loops identified through the cataloging procedure.

We find lopsided statistics when comparing the compilation of loops between passbands, leading to new ideas about what might be influencing the processes as loops are brightened. Potentially, there are multiple phases of heating or loop relaxation that allows the distribution of loops that brighten to overlap in new and interesting ways. We find evidence of two loop populations: the first consists of loops that have been newly reconnected to populate that domain, while the other contains loops that have subsequently undergone another process

that causes them to brighten again. This result also suggests the possibility of partitioning the different temperature populations among different magnetic domains, based on their observed morphologies. Additional evidence is provided to strengthen this assertion, through various observations and inferences across the three band passes utilized in Chapter 4.

Finally, the *coda* of Chapter 5 brings to a close this body of work. It consists of a brief reprise of the major themes, and details the impact the results herein have on the understanding of coronal loops formed by reconnection. Remarks are then made on what new avenues one may take in efforts to advance the study of such loops. It concludes with possible extensions from this particular AR pair, to ARs more generally.

CHAPTER TWO

MEASURING AND MODELING THE RATE OF SEPARATOR RECONNECTION BETWEEN AN EMERGING AND AN EXISTING ACTIVE REGION

Contribution of Authors and Co-Authors

Manuscript in Chapter 2

Author: Marika I. McCarthy

Contributions: Implemented study design. Developed analysis pipeline for EUV observations. Implemented modeling. Wrote first draft of manuscript.

Author: Dana W. Longcope

Contributions: Conceived of study design. Provided feedback on manuscript drafts.

Author: Anna V. Malanushenko

Contributions: Developed the modeling code. Provided feedback on manuscript drafts.

Author: David E. McKenzie

Contributions: Conceived of study design. Provided feedback on manuscript drafts.

Manuscript Information

Marika I. McCarthy, Dana W. Longcope, Anna V. Malanushenko, and David E. McKenzie

The Astrophysical Journal

Status of Manuscript:
____ Prepared for submission to a peer-reviewed journal
____ Officially submitted to a peer-reviewed journal
____ Accepted by a peer-reviewed journal
_X_ Published in a peer-reviewed journal

American Astronomical Society
December 2019, ApJ 887, 140
10.3847/1538-4357/ab55f0

Abstract

Magnetic reconnection occurs when new flux emerges into the corona and becomes incorporated into the existing coronal field. A new active region (AR) emerging in the vicinity of an existing AR provides a convenient laboratory in which reconnection of this kind can be quantified. We use high time-cadence 171 Å data from *Solar Dynamics Observatory (SDO)*/AIA focused on new/old active region pair 11147/11149, to quantify reconnection. We identify new loops as brightenings within a strip of pixels between the regions. This strategy is premised on the assumption that the energy responsible for brightening a loop originates in magnetic reconnection. We catalog 301 loops observed in the 48 hr time period beginning with the emergence of AR 11149. The rate at which these loops appear between the two ARs is used to calculate the reconnection rate between them. We then fit these loops with magnetic field, solving for each loop's field strength, geometry, and twist (via its proxy, coronal α). We find the rate of newly brightened flux overestimates the flux that could be undergoing reconnection. This excess can be explained by our finding that the interconnecting region is not at its lowest energy (constant-α) state; the extrapolations exhibit loop-to-loop variation in α. This flux overestimate may result from the slow emergence of AR 11149, which allows time for Taylor relaxation internal to the domain of the reconnected flux to bring the α distribution toward a single value, providing another mechanism for brightening loops after they are first created.

2.1 Introduction

The solar corona is a dynamic region where both the coronal magnetic field and the plasma that traces it are constantly evolving. Complicated magnetic fields can lead to energetic events, particularly in regions of strong magnetic fields such as active regions (ARs), where the Sun's magnetic field breaches the surface. The mechanism believed to drive events like flares (Sweet, 1958), or the heating of the corona (Parker, 1972) is known as magnetic reconnection. In most theories of reconnection, energy is released as magnetic field line connectivity is rearranged (Parker, 1957; Petschek, 1964; Sweet, 1958). While there are many theories about how this process takes place, there are not so many quantifying observations.

Previous studies looked to ARs to provide observational evidence of magnetic reconnection. In several studies, the formation of coronal loops between two different ARs has been used as evidence of nonflaring reconnection in the corona (Sheeley et al., 1975; Tsuneta, 1996; Webb & Zirin, 1981). Work done by Tarr et al. (2014) examined quiescent reconnection within single NOAA AR11112 and inferred a reconnection rate therein. Analysis of a single AR, however, can be difficult to interpret, due to the ambiguity in distinguishing between old and new photospheric flux.

The emergence of a new AR in the vicinity of an existing one provides a good laboratory in which to study and quantify magnetic reconnection. Under the prevailing understanding, each AR originates as an isolated magnetic flux tube (Fan et al., 1994; Fisher et al., 2000; Magara & Longcope, 2001). This flux tube is buoyant; it rises and breaches the surface, then expands to fill a larger volume in the corona. Two ARs that are adjacent to each other will be distinct systems, yet expand into contact in the corona. Under this assumption, any coronal loops that interconnect the two ARs must be formed by magnetic reconnection; this is the process that allows the connectivities to change. This has been modeled in various

numerical magnetohydrodyamic (MHD) simulations of emerging flux interacting with other fields in a model corona (Galsgaard et al., 2007; MacTaggart, 2011; Toriumi & Takasao, 2017). The slower emergence, compared to impulsive reconnection in a flare, provides an extended opportunity to observe and make measurements of any reconnection that occurs during the event.

Longcope et al. (2005) performed this sort of two-active-region analysis with the *Transition Region and Coronal Explorer* (TRACE; Handy et al., 1999). They studied a single pair of ARs, and found no other suitable candidates for analysis in the TRACE archives. The limited field of view of that instrument required a deliberate pointing for an extended period of time to observe an emergence and the subsequent magnetic evolution. Longcope et al. (2005) reported that reconnection, measured using the newly formed loops observed between the ARs, did not occur at the rate they inferred from the magnetic evolution of the system. Instead, there was a delay of approximately 24 hr between emergence of the new AR and its reconnection to the overlying field based on loop measurements, while the magnetic modeling was suggestive of no delay between emergence and the onset of reconnection. An observation by Zuccarello et al. (2008) has also noted a delay of $\sim$12 hr between flux emergence within an existing AR and the first appearance of coronal loops between the old and new flux. Kobelski (2014) used SWAP (Halain et al., 2013; Seaton et al., 2013) to look at eight flux emergence events, and also observed a delay between emergence and coronal loops as evidence of reconnection to a nearby pre-existing AR. Those observed delays generally were around 25 hr. However, limitations on the temporal and spatial resolution of SWAP led to the interpretation of these values as an upper bound for the time delay. More observations are required before it is possible to further characterize the specific properties of flux emergence and subsequent reconnection.

The Atmospheric Imaging Assembly (AIA) on the *Solar Dynamics Observatory* (SDO; Lemen et al., 2012) observes the full solar disk every 12s, thus providing continuous, high-

cadence observation of AR emergence. With AIA, we need not wait for a serendipitous instrument pointing to "catch" this kind of emergence event, nor do we need to monopolize the instrument as the event occurs. As such, this mission offers many more candidates for analysis. This is ideal for elucidating how magnetic reconnection is involved when two ARs come into contact in the corona.

The present work analyzes data from 2011 January 20-22, wherein NOAA AR11149 emerged to the south of AR11147 as the two AR system crossed disk center in the northern hemisphere. We ultimately find that the reconnected flux inferred from the appearing coronal loops is comparable to the total flux in either AR, overestimating the reconnected portion of its flux. In order to explain this, we argue that a single flux element in the reconnected domain appears more than once, manifesting as rebrightening coronal loops. This interpretation constitutes a significant difference between the new case and that analyzed in Longcope et al. (2005). It is necessary to explore and understand the different scenarios represented by these two cases, if we are to ultimately form a general picture of coronal reconnection between ARs. In order to obtain the best estimates of reconnected flux, the present work replaces potential-field extrapolation with a linear force-free model of individual loops in the coronal field. The improved techniques detailed herein will later be applied in a larger set of 17 emerging/existing AR pairs to quantify reconnection between them.

We describe the analysis in the following sections. We build a potential field model from *SDO*/HMI data in Section 2.2, to produce a context calculation illustrating the separator reconnection process in which we are interested. Section 2.3 uses data from *SDO*/AIA to construct a time/space stack plot from which we determine the reconnection rate, computed from the identified interconnecting loops. The process of cataloging the loops is explained in that section, and their parameters are also reported therein. An improved method for determining magnetic field's structure and properties is detailed in Section 2.4. Loops are

observed in the plane of the sky (POS), and their POS projections are 2D curves. The POS curve of a coronal loop previously identified in the data is fit to a three-dimensional field line in a linear force-free field (LFFF) model. As a result, we obtain a three-dimensional model of that loop. These results are used in Section 2.5 to re-examine both the reconnection rate and the potential field context calculation. Reasons for discrepancies are then explored. With the benefit of the 3D tracks of coronal loops obtained through the LFFF modeling, in Section 2.6 we are able to use the line-of-sight (LOS) coordinate to show where the loops lie in a plane defined by the LOS and the pixels from which the stack plot was built. We find there is significant overlap of the catalog loops' cross sections in that plane, and we also explore various rates of brightening. We conclude in Section 2.7 with a discussion regarding possible rebrightening of magnetic flux tubes inside of the reconnected flux domain.

2.2 Potential Field Model

We construct a model of the magnetic field of the emerging and the existing AR system in order to precisely define the interconnecting flux between these two magnetic systems. Because it is common to assume that an AR is a distinct, internally connected magnetic system that emerges from within the Sun (Fan et al., 1994; Fisher et al., 2000), any flux linkage between two ARs must be formed by some process post-emergence. We construct a Magnetic Charge Topology (MCT) model that uses magnetic "charges" to represent the AR's polarities (Longcope, 1996). A potential field is subsequently extrapolated from these, to create a volume-filling field model. To do this, we utilized the MPOLE suite written in IDL (Longcope, 1996). As a potential field is the state of lowest possible magnetic energy, this simple case provides a good basis for comparison with the EUV imaging observations.

The magnetic charges in our model are constructed from a series of LOS magnetograms from the `hmi.M_720s` data series of *SDO*/HMI (Scherrer et al., 2012). A subregion that contains both ARs is selected from the full-disk magnetograms. Flux concentrations are

automatically identified from a smoothed version of the extracted magnetogram; the filtered field is the vertical field from a potential field extrapolation to a height of six pixels above the magnetogram surface (Longcope, 1996). Local extrema are identified and grouped with all surrounding, downhill pixels whose magnitudes are greater than 75 G. Regions smaller than 200 px in total pixel count are then discarded, to better isolate the regions of strong flux from the small flux concentrations that are scattered all over. Each flux concentration is then replaced by a magnetic charge located at its flux-weighted centroid, with net charge given by the integrated flux. This step also includes introducing a factor that accounts for the projection of the LOS field being a component of the radial. The results of this stage are referred to as the "many-poles" model.

We choose to reduce our many-poles model to a quadrupole in order to clarify and simplify the emergence scenario. As the flux concentrations are continuously combining and separating, there is no guarantee that any one pole exists continuously in the many-poles model. Tarr & Longcope (2012) took steps to remedy this by utilizing automated tracking algorithms to gain consistency as the sources evolve in time. Here, at the expense of losing some of the finer topological detail about the two-AR system, we gain continuity by reduction to a quadrupole. Loss of resolution is not a major problem, because we are concerned with interconnecting flux between the two regions. This information is retained in the simplification, as the emerging and existing AR polarities are still distinct.

To reduce the many-poles model to a quadrupole, we manually trace a boundary around the emerging AR at each time in the sequence. All poles within the boundary are reduced to a positive–negative pair, P1 and N1, by totaling the charges of each sign in the region and computing the flux-weighted centroid of them to determine the single charge's location. The poles outside this boundary are reduced similarly to P2 and N2. After the quadrupole reduction, the field is organized into four magnetic domains: P1–N1 (emerging), P2–N2 (existing), P1–N2 (interconnecting), and P2–N1 (also interconnecting). The global field is

extrapolated from the point sources at the photosphere and field lines are traced from a positive source to its termination at a negative source. As the quadrupole is not exactly flux-balanced, this can include sources at infinity. However, as we are concerned only with the AR–AR interaction, we consider the four topological domains previously mentioned for clarity. The first three domains can be seen in Figure 2.1 (bottom), along with the separator (black), which is the shared boundary between the four domains. For clarity, we do not show the fourth domain.

Creating a quadrupolar model of the ARs' polarities over a time period captures the emergence of the P1–N1 system and provides flux measurements that are used to characterize the active region emergence in this event. Beginning at mid-emergence (2011 January 21T09:58:10), we work backwards in time until the polarities from the emerging active region do not fit the criteria for the flux concentration selection (2011 January 20T23:46:10). This provides one crude definition of the onset of emergence. This model-building was done every 2 hr for 72 hr, until the flux of the emerging AR began to level off. During this time period, the P2 and N2 poles stay fairly constant in both their individual magnitudes and their differences — they are not quite flux-balanced, but differ by a median value of 8.9×10^{20} Mx (about 10% of the flux in either polarity). To determine the beginning of our emergence event, the rate of flux emergence in the P1–N1 active region was estimated by eye such that it reasonably fit the rate of both the positive and negative polarity emergences. We find that these fluxes grow at approximately 3.47×10^{16} Mx s^{-1} during the initial phase (from 2011 January 20T23:46 to 2011 January 21T19:58:10.50; see Figure 2.2, blue dotted line). We fit a straight line to the rate of change of the unsigned flux in each polarity; this line intersects the horizontal axis in Figure 2.2 on 2011 January 20 at 22:01. We will henceforth call this time the beginning of the emergence.

From this quadrupolar model, we calculate the interconnecting (IC) flux that connects the emerging positive (P1) to the existing negative (N2) polarity. This is the same as the

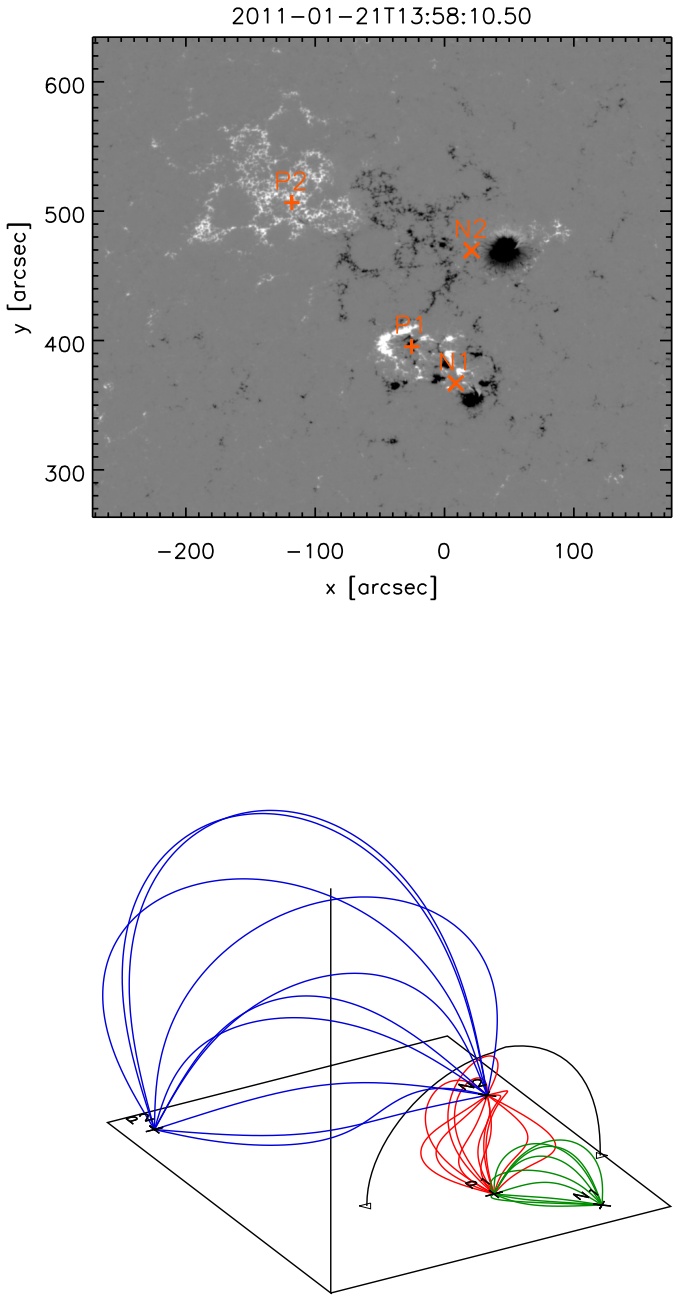


Figure 2.1: Top: Using the line-of-sight magnetogram from *SDO*/HMI, we build an MCT model (orange). The magnetogram is shown on a linear scale that saturates at ±700 G. Bottom: Three out of four total magnetic domains are illustrated — the existing AR (blue), the emerging AR (green), and the interconnecting flux between the new and old ARs (red). The separator, the junction at which the four magnetic domains meet, is shown in black.

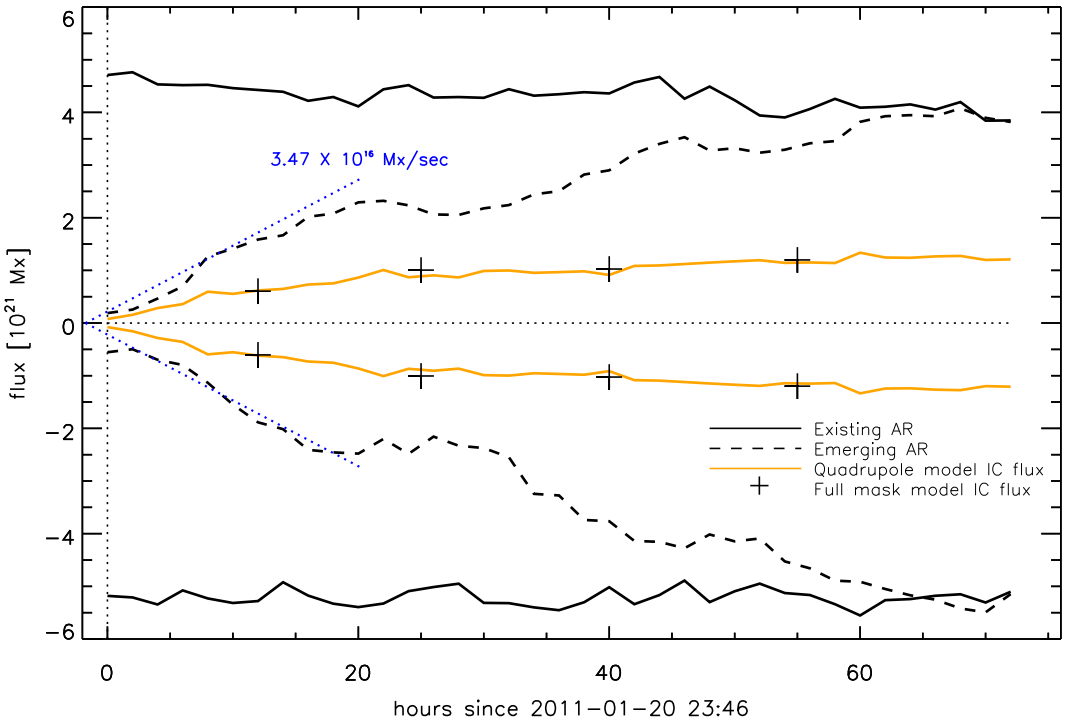


Figure 2.2: The fluxes from our MCT model are shown here. The flux of the active regions are shown in black: the flux of the existing AR (solid) is fairly constant in time, while the emerging AR flux (dashed) increases over a 72 hr period. The interconnecting flux from the quadrupolar MCT model is shown in orange. The crosses are the interconnecting flux determined from many magnetic charges before the reduction to a quadrupole, to make sure we did not lose information by doing the reduction of the model. The vertical dotted line denotes the first time of the MCT modeling, and the x-intercept of the blue dotted linear fit denotes what we call the time of emergence of the new active region.

flux through the surface bounded by the separator — the intersection of the separatrices, i.e., surfaces that divide topologically distinct regions — provided the separator curve is closed such that the P1 and N2 charges lie on opposite sides of this bounded surface (Longcope & Magara, 2004). We perform this calculation using a Monte Carlo method that uses randomized locations around each source to trace field lines (Barnes et al., 2005). The ratio of number of field lines that connect charges P1–N2 to the total amount of field lines traced around these charges determines the fraction of flux that connects them, and thereby determines the P1–N2 interconnecting flux. In Figure 2.1 (bottom), the red field lines belong to the interconnecting domain. Observe that these field lines go through the surface bounded by the separator (black). Figure 2.2 shows the results for the quadrupolar modeling over the emergence time in orange. The crosses shown in Figure 2.2 are instances where the interconnecting flux was determined with the many-poles model. When using the more complex model, the more complex topology requires us to consider the contributions from multiple poles between ARs which is much more computationally intensive. With the quadrupolar model, we only need to consider the P1 and N2 poles. Both the many-poles and quadrupolar models give approximately the same result, and thus we may use the computationally cheaper method at other times as well.

The interconnecting flux changes in time throughout our model. A time-evolving flux is described by Faraday's law:

$$\dot{\Phi} = -\oint \vec{E} \cdot d\vec{l} = -\mathcal{E}. \tag{2.1}$$

The presence of an electric field is of no consequence in a vacuum, since any electric field is allowed to be aligned with the magnetic field (Longcope & Silva, 1998). In a conducting plasma, however, this is not permitted and the electric field is required to be perpendicular to the magnetic field (Longcope & Silva, 1998). Thus, there must be a difference in the

mechanism causing the evolving interconnecting flux between our idealized, MCT model in vacuum and the reality in a conducting plasma. This mechanism is magnetic reconnection. A perfect conductor would not break magnetic field lines to rearrange the field topologically; the presence of the EMF, $\mathcal{E}$, violates the condition of a good conductor. Therefore, reality lies somewhere in between zero interconnecting flux and the interconnecting flux obtained through our MCT model. In the next section, we seek evidence of newly reconnected flux between the old and new ARs in coronal loops, using data from *SDO*/AIA to make measurements of this reconnection process.

2.3 Interconnecting Flux Evident in AIA

We use a series of *SDO*/AIA images to measure magnetic reconnection between the emerging and existing ARs. In most theories, reconnection is accompanied by an energy release (e.g. Parker, 1957, 1972; Sweet, 1958). We expect the plasma that traces the coronal magnetic field to be heated as a result of this reconnection and become bright in the EUV. We go further and assume that the only means by which loops are heated — and made visible — is the energy released by the reconnection, which creates interconnecting flux. This allows us to correlate the reconnected magnetic flux with the magnetic flux in newly brightened interconnecting loops. Longcope et al. (2005) used this same approach to quantify separator reconnection between an emerging AR and the overlying field, in the form of coronal loops between the two ARs. Magnetic reconnection is occurring in the present emergence event as well: we see the coronal loops between the two ARs in the AIA 171 Å images (see Figure 2.3). This is clear evidence of magnetic reconnection in the corona –and with the foregoing assumption, we can quantify its rate.

We make measurements of magnetic reconnection by quantifying the accumulated area of coronal loops crossing the surface bound by the separator at a given time. Ultimately, we obtain accumulated flux, manifesting itself in newly appeared interconnecting loops.

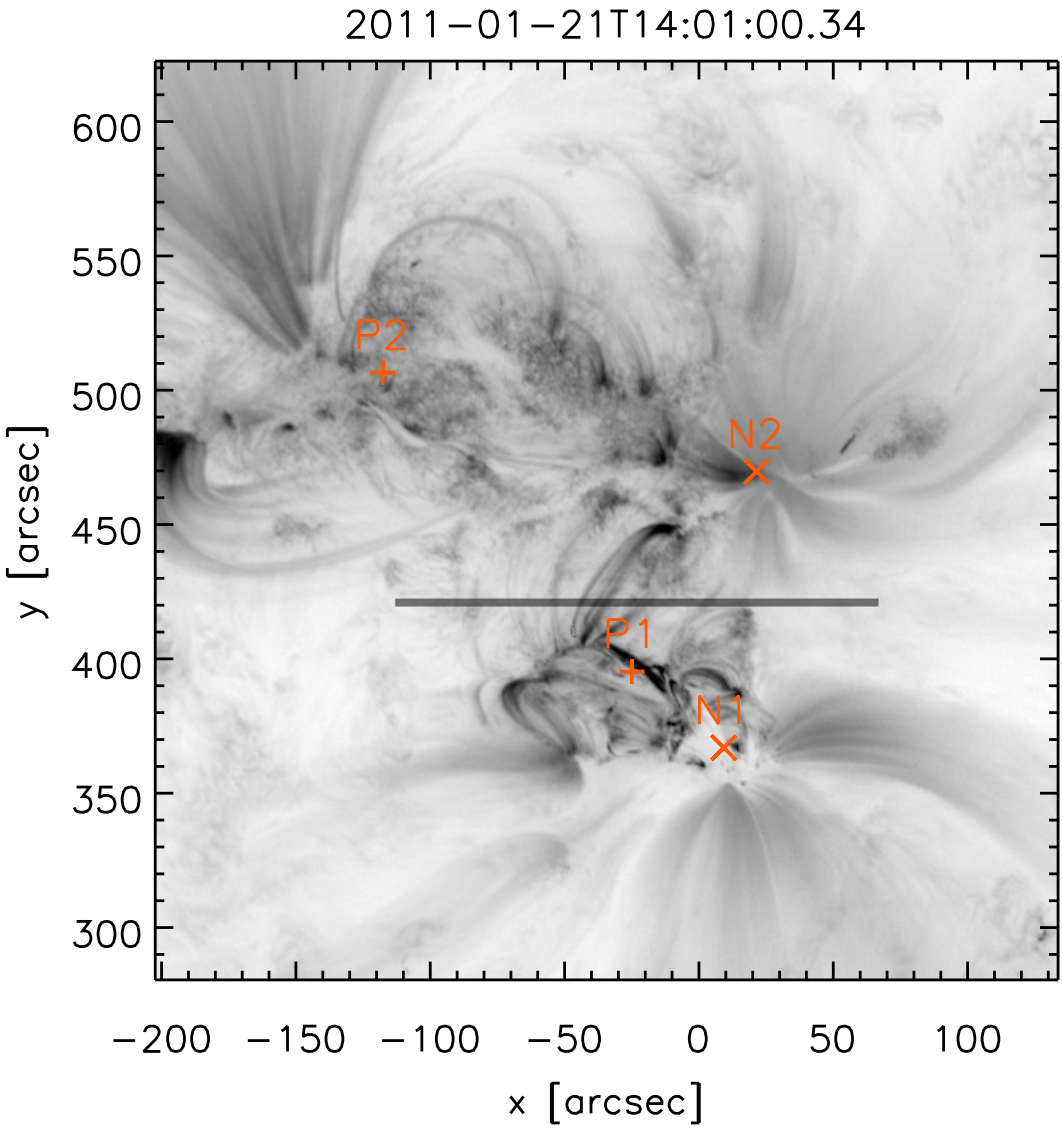


Figure 2.3: A 171Å image from *SDO*/AIA showing the emerging and existing active regions. Slit location is shown by the dark bar. We assume that any coronal loops connecting the two ARs will cross that slit. Figure is displayed with a reverse (light-to-dark) color scale, has been square root-scaled as to better see the coronal loops for reference, and saturates at $55(\mathrm{DN/s})^{-1/2}$. Quadrupolar MCT model is overlaid for reference, in orange.

By measuring the rate of change of the interconnecting flux, we determine the integrated reconnection electric field using Faraday's law (Equation 2.1). To make this measurement, we use 48 hr of AIA data in the 171Å channel with a one-minute cadence, starting at the time we identified in Section 2.2 as the beginning of the emergence. Although evolution of the emerging flux region continues beyond this, 48 hr was enough time to assure that measurable reconnection had taken place. The data were processed with the SolarSoft routine `aia_prep` to convert level 1 data to level 1.5 (Freeland & Handy, 1998). This included exposure normalization to convert intensities from DN to DN s^{-1}.

2.3.1 Cataloging Coronal Loops

A time/space stack plot is used in our analysis to catalog all the coronal loops that connect the two ARs. An array of pixels was extracted from each of the prepped AIA images (Figure 2.3). This was a horizontal array 300 pixels (180") wide and 5 pixels tall. The slit is positioned between the two ARs so that any interconnecting loop would be certain to cross it and no loops internal to ARs would. That array is averaged to a 300x1 pixel array, where each pixel was the mean of the five in the column extracted from the data. At the beginning of the data set (2011 January 20 at 22:01 as determined from the linear fit in Section 2.2), the lower left pixel of the slit was located at $[-250'', 420'']$ in Cartesian coordinates on the plane of the sky, where disk center is $[0'', 0'']$. The x-position was tracked with solar rotation thereafter in the data set. The intensity arrays were stacked to build the stack plot shown in Figure 2.4. As the coronal loops are bright, they will appear as local maxima in intensity in one row of the stack array (as seen in Figure 2.5), and will appear in the stack plot as persistent bright streaks in time[1].

Bright streaks are identified from the stack plot automatically, and subsequently visually

[1]Figures 2.3 — 2.5 use a reverse (light-to-dark) color scale, and thus our "bright streaks" of emission are dark in this color table. We choose to refer to the appearance of these loops from the onset of intense emission as "brightening" for consistency with common usage.

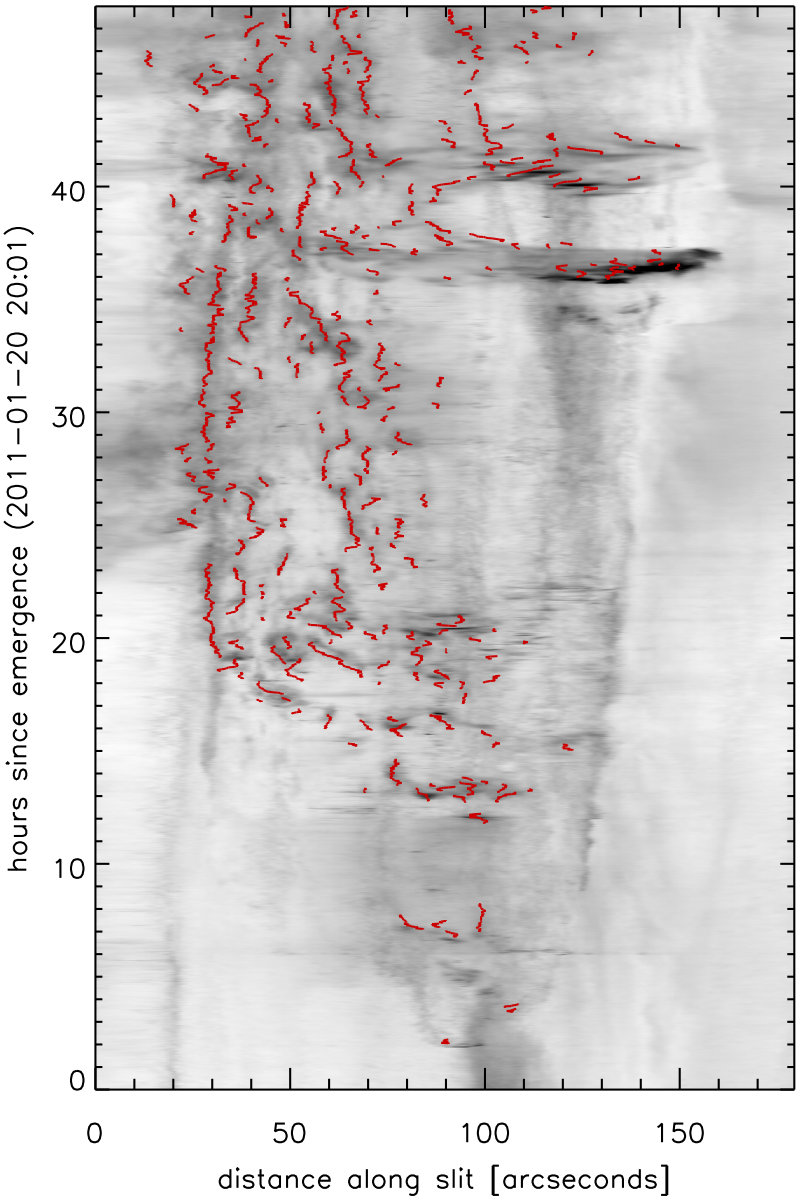


Figure 2.4: A time/space stack plot built from the virtual slits extracted from AIA images. Verified interconnecting coronal loops are plotted over the stack plot in red. The stack plot has been square root-scaled for this figure to better distinguish the streaks of strong emission; the data used in the analysis were not scaled in this way. The image's reverse color scale saturates at $55(\mathrm{DN/s})^{-1/2}$.

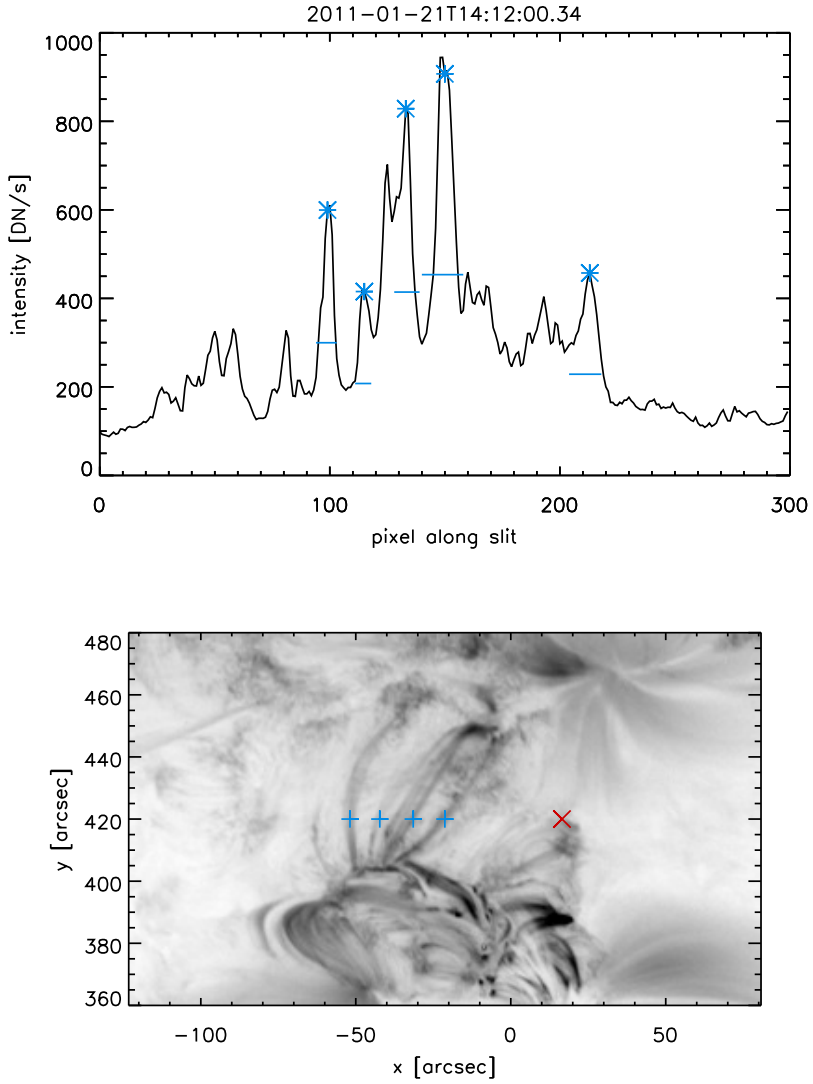


Figure 2.5: Top: a single row from our stack plot. Peaks from our local maxima finder are shown as asterisks, and the diameters are shown as horizontal bars.
Bottom: the peaks identified from the top panel are now plotted over the AIA image. Peaks indicated by blue crosses appear to correspond to interconnecting coronal loops; the red X does not, and would be discarded. The reference AIA image has been square root-scaled to more clearly visualize coronal loops in the data. The reverse color scale of the image saturates at $60(\mathrm{DN/s})^{-1/2}$.

confirmed to be coronal loops. For each time slice of the stack plot, bright peaks along the slit are determined. The intensity is boxcar smoothed with a kernel of 5 pixels along the artificial slit. A threshold is determined from taking an average of the intensity values along the slit; all pixels below the threshold are removed from consideration. Local maxima are then identified and the loop's "edges" are determined from their full width at half maximum (FWHM). From the identified edges, we obtain the diameter. A peak must be greater in smoothed intensity than 90 DN s^{-1} above the threshold to be included in the set of local maxima.

Successive intensity peaks at a similar location in the slit are linked together to turn individual peaks into sustained bright streaks, which are candidates for being interconnecting loops. In order to be linked, the subsequent peak (1 minute later) can have moved no more than 3 pix (1.″8) to either side. This is within a typical loop radius of 2″ in previous studies with *TRACE* (Aschwanden et al., 2000; Longcope et al., 2005) and AIA (Aschwanden et al., 2013). When there is no next peak to be linked to, this is the end of the bright streak. If in a given row there is a new maximum that does not link to any existing, "alive" loops, then that is considered the beginning of a new bright streak. We allow for a peak to temporarily disappear for one time step only, such that two bright streaks at the same location and which look to be the same loop but are separated by one slice in the stack plot are not counted as two distinct loops. There must be two successive images without linked peaks for a bright streak to truly end.

The properties of the streaks are interpreted as properties of loops. Through our maxima-linking procedure, we obtained both a lifetime (taken from the start and end of the bright streak in the stack plot) and a median diameter (median of all FWHMs during maxima identification) for every bright streak. At this point in the automatic selection process, we have 2259 loop candidates. Note that these candidates included 852 maxima that were not linked to another at a different time, and 394 streaks that only lasted 2 time

steps.

Of the 2259 bright streaks automatically selected, only 554 lasted five minutes or longer. This minimum-lifetime cutoff of five minutes was chosen to make the subsequent manual confirmation from a data set that did not include ephemeral bright streaks. We visually examine each of the remaining loop candidates to ensure that it is a true coronal loop. The automatic maxima finding and linking procedure identifies many candidates, and these can include features other than coronal loops, e.g., transition region moss (see Berger et al., 1999), that produce persistent bright streaks. For example, the rightmost peak in the top panel of Figure 2.5 is caused by the chromospheric moss feature marked with a red X in the lower panel. We use this kind of visual inspection to identify and discard bright streaks that are not loops. After this process, we have 301 verified interconnecting coronal loops, which are shown on the stack plot in Figure 2.4 in red.

2.3.2 Loop Properties

Each of the 301 identified loops is characterized by properties obtained from the stack plot. Lifetimes are determined from the stack plot slices that contain the birth and death of the loop. This is the length of time that there is a continuous (in time) peak in the intensity at nearby locations along the virtual slit. A loop's diameter is found from the median value over all times of the FWHM found in the local maxima-finding process. The histograms in Figure 2.6 show these values[2]. The shoulder on the low end of the lifetime distribution is an artifact of our minimum lifetime cutoff criteria. Loops have a median diameter 5.9 Mm (median of all medians), and the loops of the smallest diameter are well above the CCD pixel size of AIA (approx. 0.4 Mm). Loops usually last less than 30 minutes, with a median lifetime of 15 minutes.

We compare these observed lifetimes to a typical cooling time of a coronal loop.

[2]The lifetimes histogram cuts off a single outlier data point, a loop that lasts 202 minutes

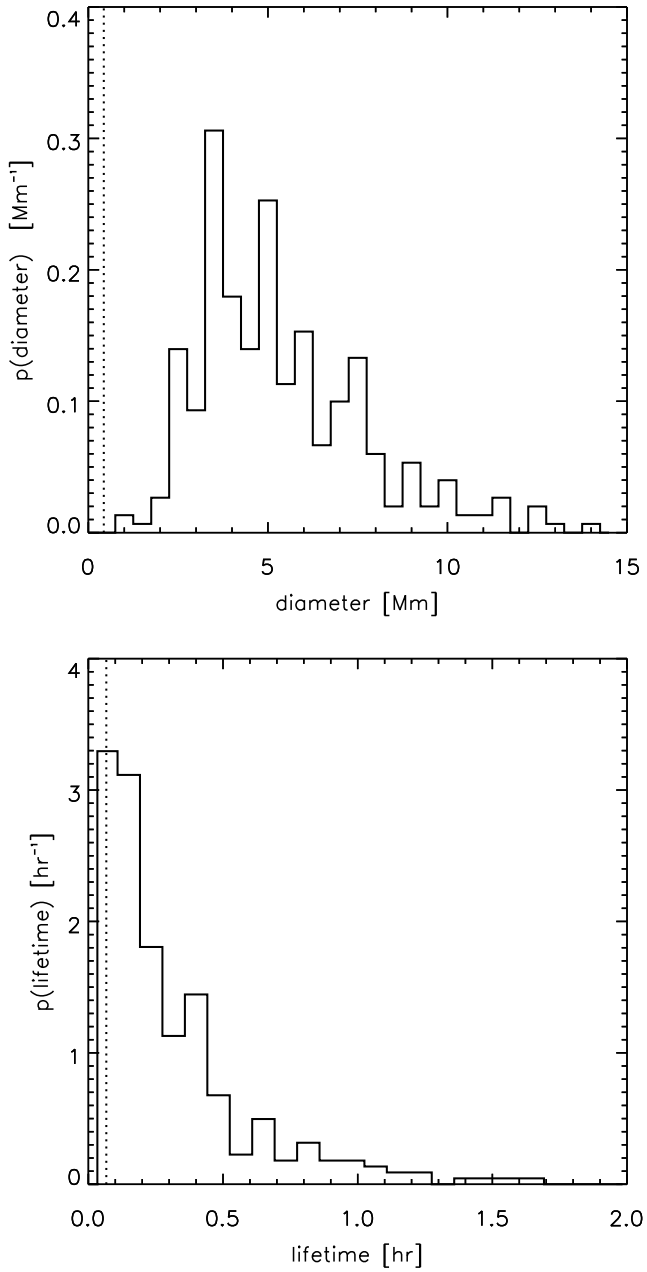


Figure 2.6: Histograms denoting the properties of the 205 loops interconnecting the two ARs. Top: median loop diameters in Mm. Dotted vertical line denotes the size of one AIA CCD pixel during this event (0.″6, 0.43 Mm). Bottom: loop lifetimes in minutes. This histogram cuts off one data point to better show the bulk of the distribution for clarity, whose lifetime of 202 minutes was much greater than the rest of the distribution. Vertical dashed line shows the threshold time (five minutes) for a loop to be included in our database. The abrupt drop at the lower end of the lifetime distribution is an artifact of our loop cutoff criterion.

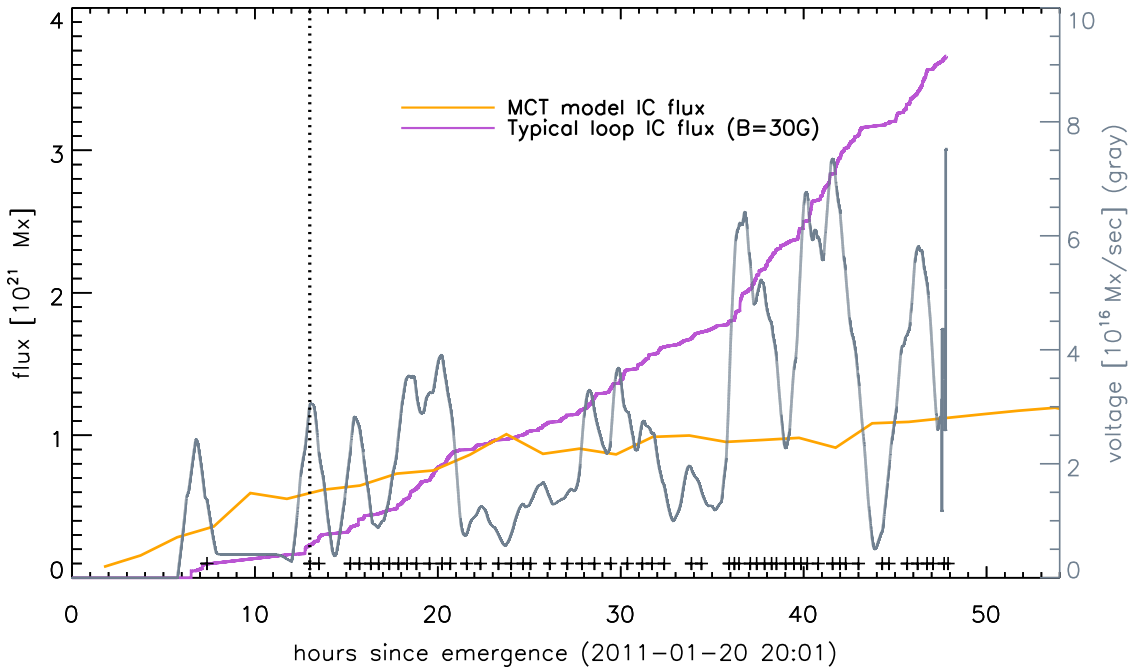


Figure 2.7: Integrated reconnection electric field. The mean voltage is 2.13×10^{16} Mx s^{-1} = 213 MV. Crosses at the bottom denote the times used for magnetic modeling in Section 2.4. Vertical dotted line denotes when the bulk of reconnection begins: a 13 hr delay from the emergence.

During its cooling phase, the loop will cool through a combination of radiation and thermal conduction. These processes operate on time scales given by

$$\tau_{\rm rad} = 2.3 \times 10^3\,{\rm s} \left(\frac{T}{10^6\,{\rm K}}\right)^{3/2} \left(\frac{n_e}{10^9\,{\rm cm}^{-3}}\right)^{-1} \tag{2.2}$$

$$\tau_{\rm cond} = 270\,{\rm s} \left(\frac{n_e}{10^9\,{\rm cm}^{-3}}\right) \left(\frac{T}{10^6\,{\rm K}}\right)^{-5/2} \left(\frac{L}{10^9\,{\rm cm}}\right)^{2}$$

where T and n_e are the temperature and electron density at the tube's apex, and L is its full length (Cargill et al., 1995). When the loop is sustained by uniform volumetric heating, i.e., RTV equilibrium (Rosner et al., 1978), or is cooling quasi-statically, the conductive and radiative cooling rates are equal. This condition can be used to eliminate the electron

density, n_e, and obtain a combined cooling time

$$\frac{1}{\tau} = \frac{1}{\tau_{rad}} + \frac{1}{\tau_{con}} = \frac{2}{\tau_{rad}} = \frac{2}{\sqrt{270 \cdot 2.3 \times 10^3} T_6^{-1/2} L_9}, \tag{2.3}$$

giving a cooling time

$$\tau = 6.5\, L_9 T_6^{-1/2}\,[\mathrm{min}], \tag{2.4}$$

where $L_9 = L/(10^9\,\mathrm{cm})$, and $T_6 = T/(10^6\,\mathrm{K})$. For a loop of length 60 Mm ($L_9 = 6.0$) and observed in the 171 Å passband at $T = 0.6$ MK ($T_6 = 0.6$), the cooling time $\tau = 50.3$ minutes. The lifetime range for our identified loops are typically of the same order of magnitude as this crude estimate. This is consistent with loops that have been heated impulsively (for example, by reconnection) and then undergo free cooling.

Our 301 loops have properties similar — but not identical — to the 43 found by Longcope et al. (2005), also during a 48 hr interval. The typical loop diameter we find (5.9 Mm) is approximately 60% larger than the value from Longcope et al. (2005), 3.7 Mm. It is possible the discrepancy arises from the artificial enhancement of our diameters due to the boxcar smoothing. The lifetimes found between that work and this one lie mostly within 90 minutes (1.5 hr), with both studies containing several loops that last much longer. As in Longcope et al. (2005), there was a delay between emergence and the bulk of reconnection. The delay in this case was 13 hr since the beginning of the emergence as determined in Section 2.3.1 (the vertical dotted line in Figure 2.7), compared to 24 hr in Longcope et al. (2005). Delays in the range of 12–25 hours have previously been observed (Kobelski, 2014; Longcope et al., 2005; Tarr et al., 2014; Zuccarello et al., 2008), but more investigation is required to confirm whether this seemingly common phenomena is ubiquitous in flux emergence. If we find that it is, we also wish to ascertain what properties of the system determine whether the delay is closer to 12 hr, as in this work, or to the 24 hr interval found in Longcope et al. (2005).

We use the loops and their properties to calculate the time-varying interconnecting flux. Under the assumption that the flux tube is a cylinder, we turn the identified diameters into cross-sectional areas. We define a cumulative area, $A(t)$, which jumps by the cross-sectional area where it crosses the slit of a particular loop at the instant that loop is born. To obtain interconnecting flux as a function of time, we multiply $A(t)$ by a characteristic magnetic field strength $B_{\rm char}$. We chose $B_{\rm char} = 30$ G as informed by our MCT model. We use the quadrupole model to find a typical field strength around the approximate location of the separator in the middle of our data set; reconnection occurs along that boundary to exchange flux between the magnetic domains. The interconnecting flux as a function of time is then:

$$\Phi(t) = \int \mathbf{B}_{\rm char} \cdot d\mathbf{A}(\mathbf{t}) = B_{\rm char} A(t), \tag{2.5}$$

which is shown as the purple line in Figure 2.7.

The integrated reconnection electric field was determined from Faraday's law (Equation 2.1) by taking a time derivative with respect to $\Phi(t)$. The voltage, $\dot{\Phi}$, is shown in Figure 2.7 as the gray line. Though this has been boxcar-smoothed over half-hour time intervals to eliminate some of the high-frequency variation (for clarity), this reconnection between the old and new ARs occurs in bursts similar to the observations of Longcope et al. (2005), impulsively heating these loops into the 171 Å passband.

The interconnecting flux obtained from accumulated coronal loops is larger than that from the MCT model presented in Section 2.2. This is despite possibly undersampling the coronal loops between the two ARs during our cataloging process by choosing a minimum loop lifetime of five minutes, as well as the fact that we are using 171 Å data only. While the effect of reducing our system of two ARs to a quadrupole was minimal with regard to the calculation of interconnecting flux, a more complete model of the field might lead to a characteristic field different than we obtained through our MCT model earlier in this section.

2.4 Nonpotential Force-free Field Modeling

It is possible to compute the flux more accurately than in Equation (2.5), which assumes that a single B value applies to every single loop at the location where it crosses the slit in this projection. If each coronal loop traces out a magnetic field line, each should have its own field strength as it crosses the slit. By using a more sophisticated modeling method, we can assign each loop identified in the stack plot its own field strength and calculate a more informed value for the interconnecting flux. The coronal magnetic fields of ARs are believed to be in a force-free state that satisfies

$$\nabla \times \mathbf{B} = \alpha(\mathbf{r})\mathbf{B} \tag{2.6}$$

(Nakagawa et al., 1971). A particular case of a force-free field is an LFFF, or a constant-α field, in which $\nabla\alpha = 0$. We use this condition along with $\nabla \cdot \mathbf{B} = 0$ to transform Equation (2.6) into a Helmholtz equation for $\mathbf{B}$. We will fit a coronal loop to a field line in an LFFF to determine its three-dimensional structure and properties, using the technique from Malanushenko et al. (2009). However, the superposition of LFFF lines with different values of α is not an LFFF field itself. Thus, a global field containing these LFFF extrapolations is not necessarily a force-free field itself.

The method of Malanushenko et al. (2009) utilizes magnetogram data to create a set of volume-filling LFFFs, and then uses a traced coronal loop in an EUV image to determine the most likely LFFF to which it fits. For each modeling attempt, the Helmholtz equation for $\mathbf{B}$ is solved with the aid of magnetic boundary data at that time from an LOS magnetogram in the half-space (Chiu & Hilton, 1977; Lothian & Browning, 1995). Constant-α fields are computed for an entire volume for 61 values of α equally spaced within the range [-0.05, 0.05] arcsec^{-1}. A coronal loop is manually traced with a smooth curve over an AIA image. With

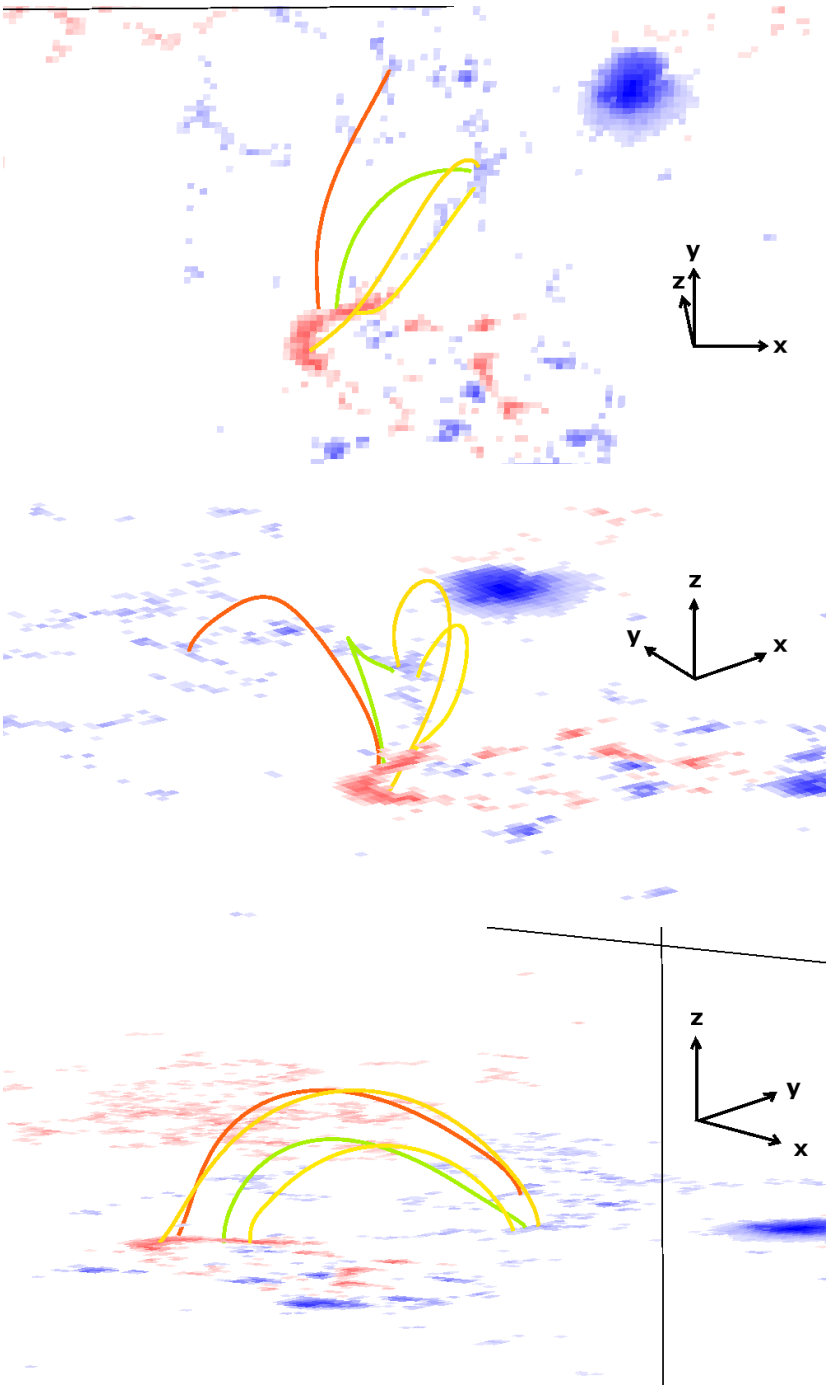


Figure 2.8: A 3D rendering of the loops at 2011 January 21T14:21 (compare to Figure 2.5) that were reconstructed from our LFFF models. The top figure shows a line-of-sight viewing angle, similar to how the loops are seen in AIA. The lower panels show the three-dimensional reconstruction of the loops at different angles.

this method, we need only trace a portion of the loop and the inclusion of visible footpoints is not required. The coordinates of the loop in the POS are known. The third coordinate, along the LOS, is unknown.

The coordinate along the LOS is determined by using field lines traced from various locations, h, along the LOS for various constant-α fields, and comparing their projections to the original coronal loop. The LOS along which the field lines are initiated is selected to cross the center of the traced loop in the POS. For every LFFF, a set of such field lines along the LOS are then projected onto the POS. An average distance between these projections and the original POS-loop, $d(h, \alpha)$, is then minimized. Determining the correct minimization is not intuitive, and is detailed in Malanushenko et al. (2009).

This modeling was done at 56 time intervals, shown by the crosses in Figure 2.7. These times were chosen to maximize the number of identified loops modeled using the fewest sample times (as building the volume-filling LFFF magnetic models is computationally expensive). Further, as the POS tracing and selection of the correct minimization is labor-intensive, we chose to prioritize modeling of loops that lasted for 10 minutes or longer. For each instance in time where the modeling is done, every field of view is cut to the same size. By doing so, we accounted for differences in time and the impact they would have on the model. The volume-filling field was created in a rectilinear domain whose bottom boundary was a plane tangent to the solar surface. We will reference z-positions with respect to the height above this tangent plane. We modeled 185 individual loops of the 205 that were identified in the stack plot from Figure 2.4 and also lasted 10 minutes or longer. Due to the manner in which we selected times in an effort to maximize the loops we modeled, there were occasions where a loop was modeled for more than one instance in time. Thus, there are 199 LFFF lines being modeled.

For each time when the LFFF model was constructed, all stack plot-identified loops present at the time and satisfying the lifetime criteria were traced to determine their

structure. One such modeling instance is shown for reference in Figure 2.8. The value of α along the field line is a result of selecting the correct minimization of $d(h, \alpha)$. The distribution of these values for all of the loops we modeled is shown in Figure 2.9.

Of the 16 loops that were modeled at more than one time, most (but not all) of their subsequent modeling yielded their α trending closer to zero. This was true even for loops with negative α: those values trended less negative. Furthermore, α and emergence time have a Spearman rank-order correlation $\rho = -0.21$, indicating a correlation at a significance level of 99.8%. A linear fit of this data set had positive values with a negative slope. Because the values of α skew positive, this trend toward zero could show the positive wing of the α distribution trending to an equilibrium near zero.

The three-dimensional magnetic field line corresponding to an observed loop yields a value for its full length, as well as for the height and magnetic field strength at the point it crosses our slit. (The full length is used in the estimate of cooling time given in Section 2.3.2.) A height vs. field strength scatter plot of the modeled loops is shown in Figure 2.10 where the loops are grouped into different colored time intervals, chosen such that each bin has the same number of loops (34 for the red, 33 for the other colors). The magnetic field strength values obtained from the model are also shown in Figure 2.10. If one loop was alive for multiple instances of modeling, its field strength was found from the average of slit-crossing field strengths. We used a characteristic field strength of 30 G in Section 2.3.2, which was near the histogram's peak and thus a reasonable choice for a single characteristic value. However, the distribution skews to the positive side of the mode, and neglecting the skew may have resulted in an underestimation of the flux.

The interconnecting flux was recalculated using the computed field strength value for each loop (Figure 2.11, dotted-dashed red line). There were 116 loops not modeled individually, which could not be assigned a field strength informed by the LFFF modeling. To these, we assigned the median value $B = 39$ G of the modeled loops. The interconnecting

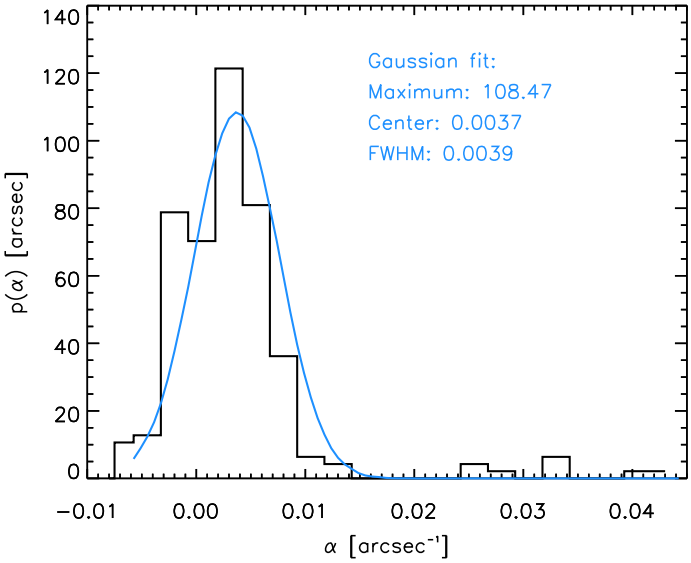


Figure 2.9: A histogram showing the α values for all the loops obtained through our LFFF model. The Gaussian fit and its parameters are plotted in light blue.

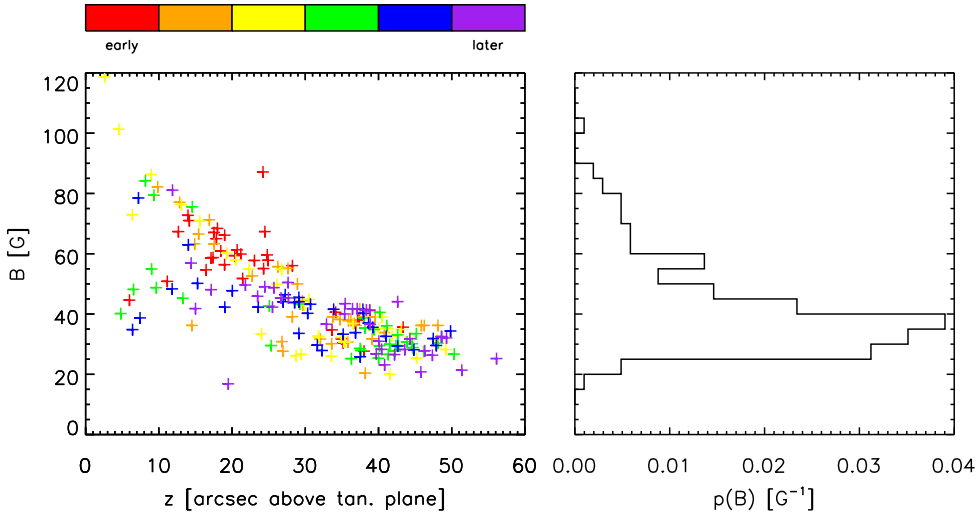


Figure 2.10: This combination scatterplot and histogram details the magnetic field strengths we obtain from our LFFF model. Crosses denote B strength vs. height, and colors correspond to different time intervals. The intervals were chosen to contain roughly the same number of loops; each color is a group of 33 loops (with red containing 34).
The histogram shows the B values for all the loops obtained through our LFFF model. Bins are 5G.

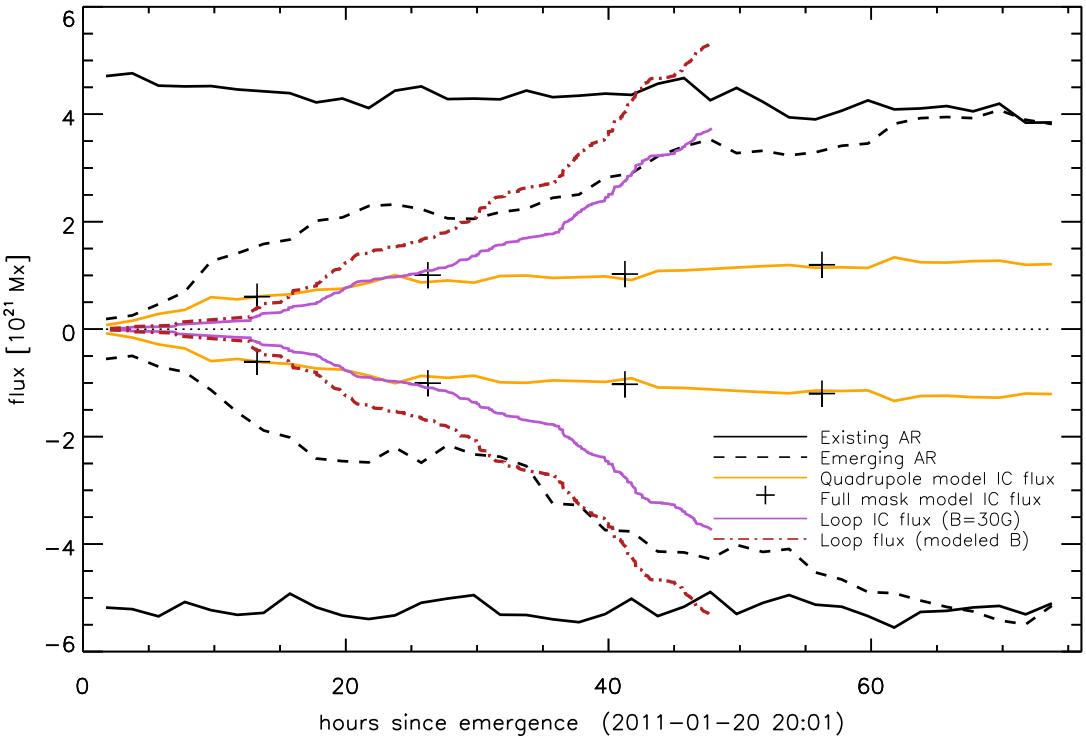


Figure 2.11: The same flux plot as in Figure 2.2, but with the interconnecting loop flux obtained from the loop diameter data from the stack plot with a characteristic (purple) or LFFF modeled (dotted-dashed red) field strength.

flux calculated with this method is approximately 50% greater than when every loop was assigned a common characteristic value of 30 G. The mean value of field strength of our LFFF-modeled loops at the location of the virtual slit as determined from the LFFF model was 43.7 G, approximately 45% larger than the characteristic value used in Section 2.2, which may play a part in the discrepancy between using the median of the distribution and the mean. However, not only is the interconnecting flux determined from our stack plot in conjunction with our improved field modeling still larger than the maximum allowed by the MCT model, but the magnitude of interconnecting flux is comparable to the total emerged flux of the newly emerged AR and even surpasses the magnetic flux of the stronger, existing AR's polarities. This implies that more flux is reconnecting from the emerging positive polarity to the existing AR than is there to begin with. If this were true, then there would have to be an additional source of flux contributing to this interconnecting region that is not either of the two ARs. Therefore, more investigation is necessary.

2.5 MCT Model with Nonzero Twist

In an effort to find a better coronal magnetic model with which to compare the interconnecting flux, we revisit our initial assumption of a potential field. The updated flux calculation uses values of α informed by the LFFF modeling. In the modeling done in Section 2.2, the potential field used had an $\alpha = 0$ by definition. We find the interconnecting flux is larger for a nonzero α value compared with the potential field case (where $\alpha = 0$; see the orange lines in Figures 2.2, 2.7, 2.11, and 2.12). However, we find that this increase is $\approx 20\%$ and does not account for the large discrepancy between the interconnecting fluxes calculated in Section 2.3.2 and Section 2.4 (purple and dotted-dashed red lines in Figure 2.11) when compared to that from the potential field.

To perform this computation, we use values of α obtained from the modeling in Section 2.4, which definitely skew positive (see Figure 2.9). This positive skew in values

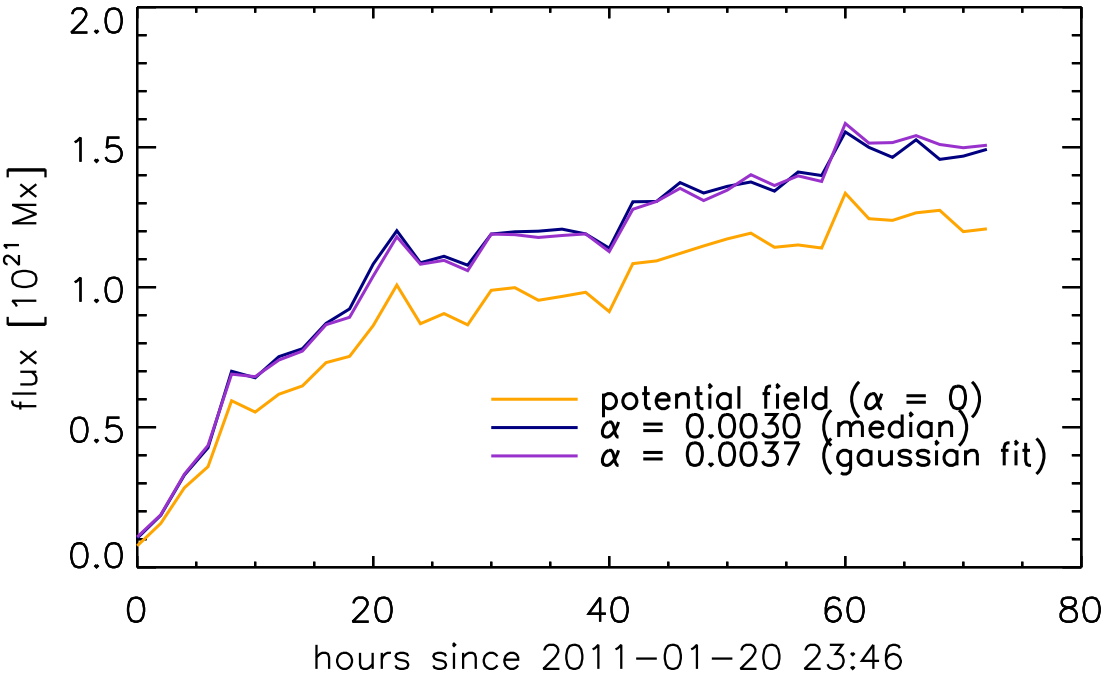


Figure 2.12: The interconnecting flux of the potential field (orange) is the same as Figure 2.2. We also repeated this analysis for α values that were the mean (navy) and Gaussian (mode) fit (purple) of the distribution in Figure 2.9.

of α may be responsible for the discrepancy between the high interconnecting flux we see in contrast to what a potential field allows. The nonpotentiality of the field, suggested by the modeled loops, might partition the flux in a different manner, such that there is more flux allowed in the interconnecting region than when compared to the lowest energy state of the field. We redid the interconnecting flux calculation using a nonzero α in the MCT model (these values are detailed below). The same quadrupole models from Section 2.2 were used to perform the extrapolation for these new fields and subsequent interconnecting flux, using the Green's function from Chiu & Hilton (1977). Unlike the modeling in the previous section, the global field in the MCT model detailed here is an LFFF.

Two extrapolations were done to calculate interconnecting flux in an LFFF model, for

two different values of α: one corresponding to the peak of a Gaussian fit to the histogram in Figure 2.9 ($\alpha = 3.7 \times 10^{-3}$ arcsec^{-1}), and the second one corresponding to the median of the same distribution ($\alpha = 3.0 \times 10^{-3}$ arcsec^{-1}). The results of these extrapolations are shown in purple and navy, respectively, with the original $\alpha = 0$ results shown in orange in Figure 2.12. There is an increase in the magnitude of interconnecting flux between the two ARs for a nonzero twist; however, it is nowhere near large enough to account for the results determined from the stack plot with AIA data.

2.6 Loop Locations in the Plane Defined by the Slit and the Line of Sight

With the benefit of three-dimensional loop information, we see that it is likely that some flux has brightened repeatedly during our 48 hr observation. Figure 2.13 shows a two-dimensional histogram depicting the location of the modeled loops in the plane defined by two vectors: along the LOS and along the slit. We assume a cylindrical loop, and that each cylinder intersects the plane of the virtual slit normally, so each intersection is a circle. The center of this disk lies at the position in the tangent plane determined from the LFFF modeling in Section 2.4. The pixel color denotes the number of different disks that overlap at that point. The loop cross sections lie on top of each other in the xz-plane, with three distinct locational hot spots and at least one empty pocket where there appear to be no loops. The most apparent empty pocket to which we refer is in the range 0″–50″ from the point of tangency, and at a height of less than 30″ above the tangent plane. Figure 2.14 shows a selection of modeled coronal loops from Section 2.4 with the separator from a similar time from the MCT model in Section 2.2. Figure 2.15 depicts a version of Figure 2.13, showing the time evolution trends of the loops in that plane. (An animated version of Figure 2.15 is available.) The discrete color bins used in Figure 2.15 are the same as those used in the left panel of Figure 2.10.

Due to the manner in which our interconnecting loops lie on top of each other in

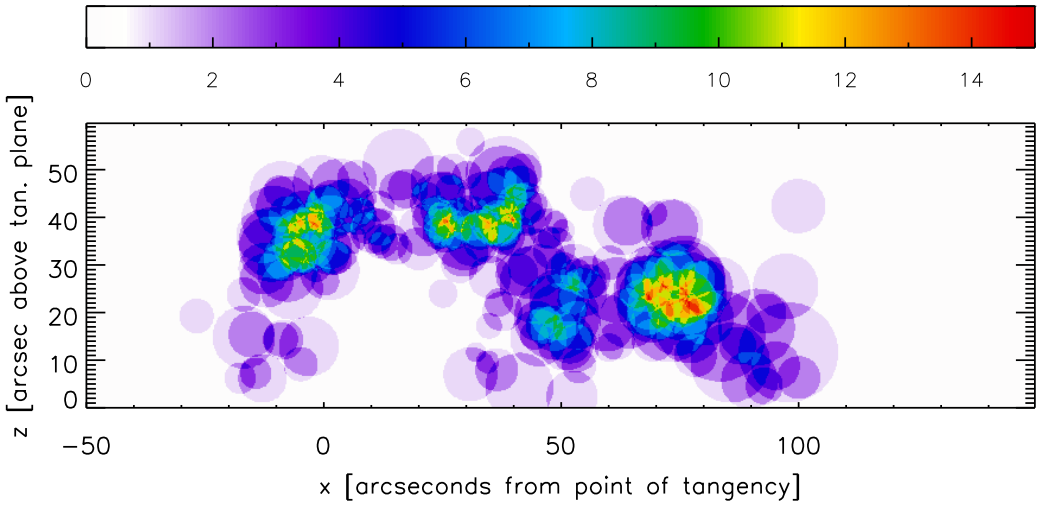


Figure 2.13: A 2D histogram showing the locations of loops in the plane that projects into the virtual slit. There appear to be distinct "hot spots" where many loop cross sections lie on top of each other, as well as "pockets" where no loops appear to be. The maximum value is 15 loop cross sections lying on one another in 48 hr of data, or 8.7×10^{-5} Hz.

the plane of the virtual slit, it may be that our assumption that a coronal loop brightens only when it is newly reconnected is faulty. Perhaps not all brightening interconnecting loops are independent samplings of new flux, and in assuming so we have substantially overestimated the flux linkage between the two ARs. Under this assumption, we neglected to consider any internal reconnection within the magnetic domain where the interconnecting loops are located. Loops in that domain reconnecting to achieve a lower energy state would be brightening loops that cross our virtual slit, but would not be newly reconnected flux from between the two AR.

Our data suggest that we are seeing a flux element brighten multiple times. We calculate the minimum amount of reconnected flux supported from our analysis by first considering an overlap percentage obtained from the 2D histogram in Figure 2.13. This percentage is that of the pixels with counts of more than one in the histogram, over the total number of

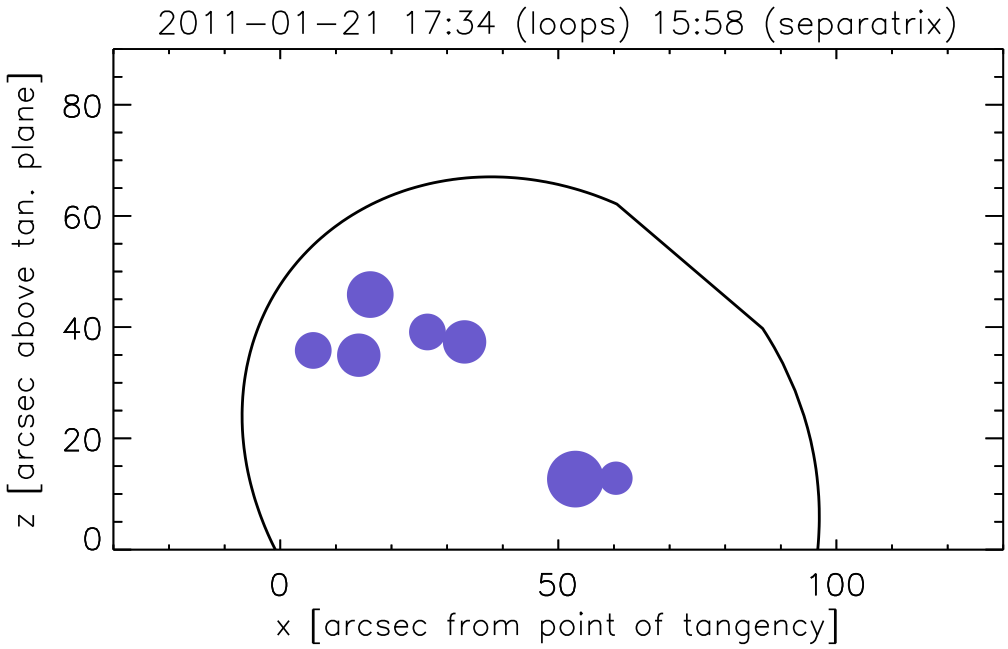


Figure 2.14: The intersection of the virtual slit with the separatrix (MCT model) and loops (LFFF model) from similar times. As in Figure 2.13, the loops are clustering in "hot spots."

pixels with nonzero counts. This yields a percent overlap of 70.77%. Applying the likelihood of non-overlap (29.23%) to the maximum interconnecting flux value from Figure 2.11 (red, dotted-dashed line) of 5.35×10^{21} Mx returns a scaled value that, to first order, corrects for the overlap we initially attributed to independent samplings of flux. This scaled value is 1.56×10^{21} Mx, which is much closer to the interconnecting flux predicted by the MCT models.

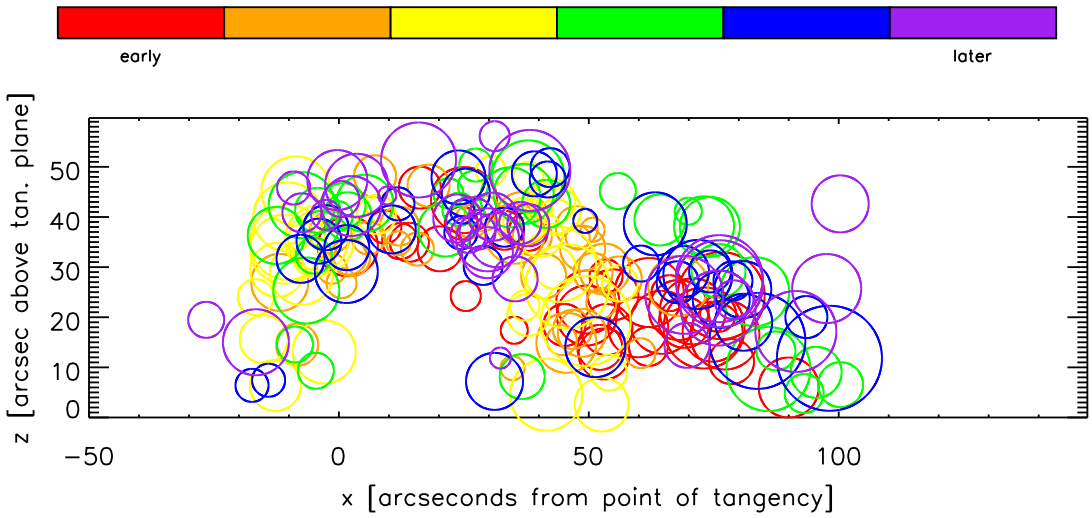


Figure 2.15: A version of Figure 2.13, wherein the time evolution is depicted by the different colored bins. The loops are binned in the same manner as in Figure 2.10. An animated version of this figure is available.

2.7 Discussion and Conclusions

Due to the advent of AIA and the subsequent increased availability of observations of emerging/existing AR pairs, we perform analysis to quantify the reconnection during one such emergence event between two distinct magnetic systems. We find we overestimate the amount of interconnecting flux we identify, despite potential undersampling of the loops with footpoints anchored in opposite ARs, due to our decision to not include loops with short lifetimes in our analysis. We assert that this may be due to seeing multiple brightenings of a single magnetic flux element throughout our observations (Webb & Zirin, 1981).

We propose that the repeated brightening of loops in similar spatial locations are the result of Taylor relaxation of the coronal field within the domain that connects the emerging positive polarity to the existing negative (Nandy et al., 2004; Taylor, 1986). Reconnection occurs within the domain in order to reach a lower energy state. The decay of a nonpotential

coronal field has been observed on timescales of tens of hours after new flux emerges (Schrijver et al., 2005). We assert that we see the field relaxing to one with constant α after an interconnecting loop is created through reconnection. As we see a distribution of α-values in our LFFF modeling of individual coronal loops, we know that the field between the two ARs is not in its lowest energy states. There is ample time for internal reconnection of the interconnecting loops, due to the slower pace of reconnection and flux evolution driven by the rate of emergence of AR11149 and the resulting topological evolution of the two AR system.

The result of the large interconnecting flux inferred from the data led to an artificially high reconnection rate. We found a rate of 2.13×10^{16} Mx s^{-1} (yielding a total reconnection time of 2.72 days when dividing the strength of the existing AR of $\sim 5 \times 10^{21}$ Mx by this rate) over two days. Tarr et al. (2014) examined quiescent reconnection within single NOAA AR11112 and inferred a reconnection rate of 0.38×10^{16} Mx s^{-1} over the same time interval. This is a reconnection time of ~ 16.74 days for an AR of similar strength, where our inflated reconnection time value is just 16% in comparison. Furthermore, although Longcope et al. (2005) concluded that they had underestimated the reconnection rate, their inferred rate was 3.97×10^{16} Mx s^{-1} (3.49 days), albeit over a substantially smaller time window of approx. 3.5 hr wherein there was an abundance of reconnection. The reconnection rate in this study peaked at approx. 7×10^{16} Mx s^{-1} (0.83 days), or $\sim 175\%$ larger than the reconnection rate of Longcope et al. (2005). The median diameter of our loop distribution 5.9 Mm is larger than the 3.7 Mm result of Longcope et al. (2005), a potential result of our boxcar smoothing during our peak finding procedure. Though these enhanced diameters could contribute to the excess of flux we see, we do not believe this is the source of significant overcounting of the interconnecting flux, as our median diameter result is comparable to those of other studies with maximum diameters of $\sim 5.6 - 6$ Mm with both *TRACE* and AIA (Aschwanden et al., 2013, 2000).

A particularly noteworthy difference between this work and that of Longcope et al. (2005), though the properties of loops obtained in both are similar, the discrepancy in number of loops cataloged (43 versus 301 in this work) may point to a significant topological difference between the two studies. MHD simulations have explored the parameter space regarding the favorability of an AR to reconnect with a neighbor. Such a difference in the amount of observed loops could be a result of the physical characterization of the polarities between these two regions (Toriumi & Takasao, 2017), or whether the field lines of opposite ARs are oriented parallel or antiparallel to each other (Galsgaard et al., 2007). This topological difference could manifest in many ways, including in the delay between an AR emergence and the onset of reconnection to the overlying field. The observed delay in reconnection, both in this study and elsewhere in the literature (Kobelski, 2014; Longcope et al., 2005; Zuccarello et al., 2008), might be a result of how inclined the fields are to reconnect given their α values — as in Linton et al. (2001) and Yamada et al. (1990), with regard to co- and counterhelicity. The evolution of the AR system may reach some critical point, allowing for reconnection that changes a property of the flux tube (like α) instead of the exchange of new flux between domains. The change in twist may cause some sort of cascade effect, wherein Taylor-like reconnection is able to take the field to an even lower energy state.

We aim to refine the methods detailed herein to improve the reliability of our loop catalog through a more a robust loop identification and selection technique. This is especially vital for a more thorough investigation of those loops with shorter lifetimes that are below our threshold in this work. Applying the improved method to a wider set of emerging/existing AR pairs will allow us to quantify what considerations, particularly with regard to cohelicity/counterhelicity between the two, play a role in this kind of coronal reconnection process.

The foregoing analysis has assumed the coronal loops observed in EUV had circular cross sections. While this is a fairly common assumption, it can be called into question

(Malanushenko & Schrijver, 2013). Doing so might offer additional insight into, or an alternative explanation for, the large flux values we have obtained.

This work was supported by NASA's HGI program.

We would like to thank the anonymous referee for helpful suggestions with regard to improving both this manuscript as well as the future work involving emerging/existing active region pair reconnection.

CHAPTER THREE

MULTISPACECRAFT OBSERVATIONS OF CORONAL LOOPS TO VERIFY A FORCE-FREE FIELD RECONSTRUCTION AND INFER LOOP CROSS SECTIONS

Contribution of Authors and Co-Authors

Manuscript in Chapter 3

Author: Marika I. McCarthy

Contributions: Developed and implemented study. Wrote manuscript.

Author: Dana W. Longcope

Contributions: Helped develop study. Provided feedback on methods, analysis, and manuscript.

Author: Anna V. Malanushenko

Contributions: Conceived of study. Provided feedback on manuscript.

Manuscript Information

Marika I. McCarthy, Dana W. Longcope, and Anna V. Malanushenko

The Astrophysical Journal

Status of Manuscript:
____ Prepared for submission to a peer-reviewed journal
____ Officially submitted to a peer-reviewed journal
____ Accepted by a peer-reviewed journal
_X_ Published in a peer-reviewed journal

American Astronomical Society
May 2021, ApJ 913, 56
10.3847/1538-4357/abf4d5

Abstract

Active region EUV loops are believed to trace a subset of magnetic field lines through the corona. Malanushenko et al. (2009) proposed a method, using loop images and line-of-sight photospheric magnetograms, to infer the 3D shape and field strength along each loop. McCarthy et al. (2019) used this novel method to compute the total magnetic flux interconnecting a pair of active regions observed by SDO/AIA. They adopted the common assumption that each loop had a circular cross section. The accuracy of inferred shape and circularity of cross sections can both be tested using observations of the same loops from additional vantage points as provided by STEREO/EUVI. Here we use multiple viewing angles to confirm the 3D structure of loops. Of 151 viable cases, 105 (69.5%) matched some form of visible coronal structure when viewed approximately in quadrature. A loop with a circular cross section should appear of a similar width in different perspectives. In contradiction to this, we find a puzzling lack of correlation between loop diameters seen from different perspectives, even an anticorrelation in some cases. Features identified as monolithic loops in AIA may, in fact, be more complex density enhancements. The 30.5% of reconstructions from AIA that did not match any feature in EUVI might be such enhancements. Others may be genuine loop structures, but with elliptical cross sections. We observe an anticorrelation between diameter and brightness, lending support to the latter hypothesis. Of 13 loops suitable for width analysis, 4 loops are consistent with noncircular cross sections, where we find anticorrelation in both comparisons.

3.1 Introduction

When viewed in extreme-ultraviolet (EUV) or X-ray wavelengths, the Sun's atmosphere is composed of narrow strands called coronal loops. Their enhanced density compared to the background causes these coronal loops to emit brightly in these wavelengths. The prevailing view is that the coronal plasma, aligned to the magnetic field, creates a cylindrical flux tube that is isotropic in the direction perpendicular to the field line (Reale, 2014). With each new generation of EUV and soft X-ray space telescopes (e.g., SXT, TRACE, Hi-C, and others; Handy et al., 1999; Kobayashi et al., 2014; Tsuneta et al., 1991), the observation of these loops and literature reporting their physical properties grow. However, the idea that these observed loops are monolithic objects, and that the cross sections of the flux tubes are indeed circular, has been called into question (Malanushenko & Schrijver, 2013).

Direct measurements of magnetic fields throughout the coronal volume are extremely difficult. Thus, one of the main methods to infer the coronal magnetic field is the traditional nonlinear force-free field (NLFFF) extrapolation method using vector field measurements taken at the solar surface (DeRosa et al., 2009; Wiegelmann & Sakurai, 2012). A volume-filling field is computed from the photospheric magnetic boundary conditions under the assumption that the magnetic force vanishes throughout. Alternatively, under the assumption that the loops are bundles of field lines that have been energized and made visible, mere observation of coronal loops provides insight into the coronal field.

The method of Malanushenko et al. (2009), however, uses both extrapolation and observation to determine the field structure in the corona. This method varies the value of parameters α (twist) and h (height above the solar surface along the line of sight (LOS)) to fit each coronal loop to its own linear force-free field (LFFF), using boundary conditions from an LOS photospheric magnetogram and tracing a portion of the loop in an EUV image. We will hereafter call this method α-h fitting. The loops are matched in the plane of the

sky (POS) by design, and this method yields a 3D structure from these 2D observations.

Following its development, the α-h fitting has been applied in several instances (Malanushenko et al., 2014, 2012, 2011; McCarthy et al., 2019; Valori et al., 2015) but has been exclusively used from one viewing perspective. By design, it is in that perspective that the model was fit. While this approach is novel in its combination of types of data it synthesizes to determine the coronal field, it has not been further tested. The way this work will test the α-h fitting is to get a second perspective in order to verify the validity of the 3D structure. The twin Solar TErrestrial RElations Observatory (STEREO) spacecraft (Kaiser et al., 2008) and the Extreme UltraViolet Imager (EUVI; Wuelser et al., 2004) aboard it provide the second perspective required for elucidating the elusive third dimension.

The STEREO mission has a fruitful history of using the twin spacecraft to do stereoscopic analysis (see Aschwanden, 2011, for a review). Typical usage of STEREO for such analysis first identifies a point of interest (POI) in the image from one instrument. This feature lies along some LOS from the first instrument. This LOS is then projected into the POS from the second viewing angle, and features along this line are identified as candidates corresponding to the POI in the first image.

This conventional usage of STEREO for stereoscopy relies, however, on the feature even existing (i.e., being observable) from this second viewing angle. If the feature does not exist (i.e., is not observed from the second perspective), it is possible that there is a false identification of correspondence between the features from both perspectives. This ties into a selection bias posited by Malanushenko & Schrijver (2013): potential asymmetries in the diameters of the loops lead to differing amounts of emitting loop plasma (and thus brightness) along these varying LOSs. In such a case, something appearing as a loop in one perspective would not even appear in another.

With the aid of the α-h fitting, we need not rely on the second perspective to construct the 3D information of the loop in which we are interested. The structure is extrapolated

from only a single perspective. It is now possible for a point along a loop reconstruction to be unambiguously mapped into the field of view (FOV) of the other instrument, without the need for triangulation.

In addition to verifying the loop reconstruction from the α-h fits, we can use the observation from multiple spacecraft to infer properties of loops. Specifically, we can add to the growing literature of investigations into loop asymmetries as proposed by Malanushenko & Schrijver (2013) using direct observations of loops (Klimchuk & DeForest, 2020; Kucera et al., 2019).

McCarthy et al. (2019) presented a case study that provides an ideal starting point for this investigation. The data set contained 301 loops that were cataloged between emerging active region NOAA AR 11149 and the adjacent AR 11147 for approximately 48 hr beginning 2011 January 20 at 22:01 UTC. A subset of these were fit at 56 instances in time using this α-h-fitting method. The EUV data were obtained from the 171 Å channel of the Atmospheric Imaging Assembly (AIA; Lemen et al., 2012) with LOS magnetograms provided by the Helioseismic and Magnetic Imager (HMI; Scherrer et al., 2012), both aboard the Solar Dynamics Observatory (SDO).

The LFFF models from this paper's data set have already proved useful in other instances, such as in investigating heating from localized reconnection at topological boundaries (Longcope et al., 2020). Further, the results of McCarthy et al. (2019) overcounted the flux interconnecting the two ARs, which may be attributed to the assumption in their analysis that coronal loops had circular cross sections.

This work will use the additional vantage points provided by STEREO/EUVI to achieve two related goals: first to assess the goodness of fit of the α-h fitting from a different instrument's LOS, and then to use the multiple viewing angles to analyze loop diameters from different POSs.

This investigation will be detailed in the following sections. We discuss the acquisition

of the EUVI data sets that complement that used in McCarthy et al. (2019) in Section 3.2 and alignment of the α-h fits with the new data set in Section 3.3. Due to limitations of the data, some analysis is best performed by a qualitative, visual inspection. That analysis is detailed in Section 3.4. A quantitative analysis is undertaken in Section 3.5. The details of the conclusions drawn from our results and future outlook are provided in Section 3.6.

3.2 Data Set Acquisition

The α-h fits presented in McCarthy et al. (2019) were constructed at 56 different time instances from 185 individual loops out of the 301 that were identified interconnecting the ARs. This is illustrated in Figure 3.1, which shows a 4 hr subset of the total 48 hr interval. Horizontal lines show the cataloged loops (with their extent representing their durations), and the dashed vertical lines are the times at which the α-h fitting was performed. The loops that were fit during this process are intersected by the dashed vertical lines. The purple star marks a time whose image, shown in Figure 3.2, includes five loops, shown as colored curves in the right panel. These loops correspond to the five horizontal lines crossing that one vertical dashed line in Figure 3.1. As the modeling times were chosen to maximize the number of loops fit, some loops were modeled at multiple times (e.g., the long-lasting loop #34 in Figure 3.1). Thus, the data set contains 199 different α-h fits representing 185 distinct loops.

The EUVI data were obtained from the Virtual Solar Observatory (VSO; Hill et al., 2009) using SolarSoft (Freeland & Handy, 1998). The angular separation from Earth was 86° and 92° for EUVI-A and EUVI-B, respectively, with a separation angle of 178° between them. The 171$\mathring{A}$ passband was chosen, as the α-h fitting used the same passband in AIA. For each of the discrete times at which the α-h fitting was done, we looked within a half-hour interval on either side of the desired time and sought the image taken nearest to that time. In Figure 3.1, the time of the EUVI-A data is denoted by a blue vertical bar, and the

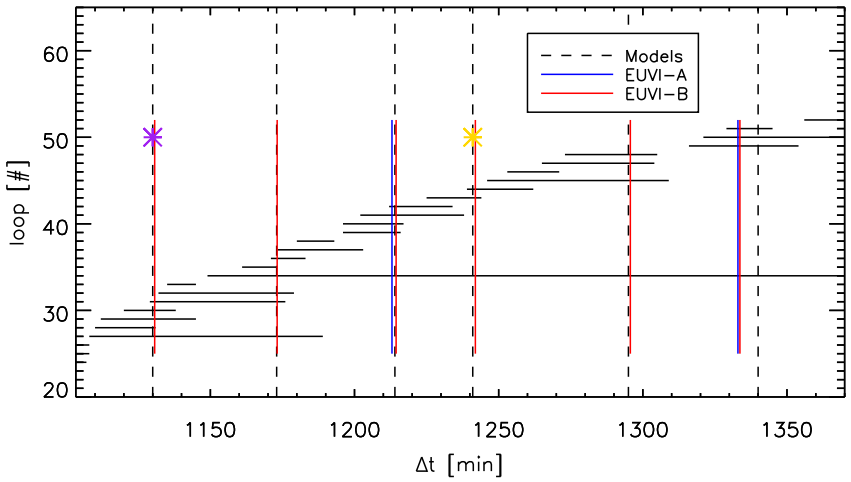


Figure 3.1: A subset of the data is shown to illustrate how the loops, α-h fitting, and STEREO data are related. Horizontal lines are the loops and their durations. The vertical dashed line is the instance at which the α-h fitting was done. The colored vertical lines are the data used from EUVI. Spacecraft A data are in blue and B data are in red. The purple and yellow stars correspond to the instances shown in Figures 3.9 and 3.10, with five and three loops respectively (corresponding to the intersections with horizontal bars). As the original data set was constructed from SDO/AIA images, each time step (in minutes) has a corresponding AIA image.

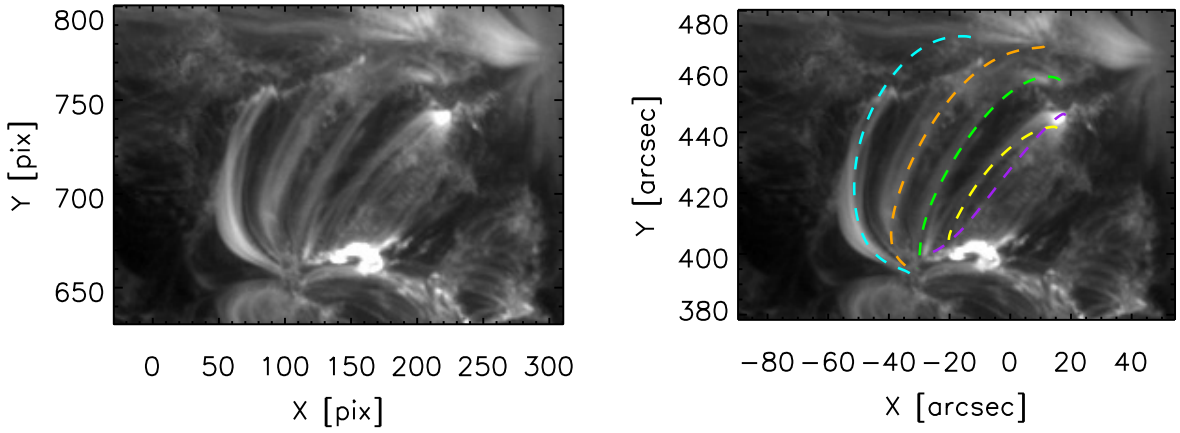


Figure 3.2: Image from AIA 171Å with the α-h fits overplotted. This corresponds to the time of the purple star and its five loops in Figure 3.1. This figure has been square root scaled with color table saturating at $70\sqrt{\mathrm{DN/s}}$ for clarity. Later, we denote this — and specifically the fit plotted in purple — as Example 1 (see Figure 3.9).

time of the EUVI-B data is in red. The vast majority of the EUVI images used are within 10 minutes of the corresponding model's time. This is within the median lifetime of these loops (McCarthy et al., 2019). These data were processed using the SolarSoft (Freeland & Handy, 1998) `secchi_prep` command with keyword `/dn2p_off` to preserve intensity units as DN s^{-1}. Some images were discarded for issues with data quality, primarily blank images. In total the data set contains 18 images from STEREO-A and 26 from STEREO-B, with 17 instances of both A and B observing simultaneously.

The SDO/AIA data used to compare with the EUVI images were previously downloaded through VSO via SolarSoft and prepped using `aia_prep` with exposure normalization. It is the same data set used in McCarthy et al. (2019) to perform the α-h fitting. Figure 3.2 shows an instance (denoted by the time of the purple star in Figure 3.1) of the α-h fits plotted over the top of the companion AIA image.

3.3 Alignment of Model with Data

The α-h fitting method of Malanushenko et al. (2009) builds a set of volume-filling LFFFs from a photospheric magnetogram and then uses a manually traced portion of an observed coronal loop from an EUV image to determine the LFFF to which it fits. An LFFF, or a constant-α field, is a particular case of a force-free field (FFF),

$$\nabla \times \mathbf{B} = \alpha(\mathbf{r})\mathbf{B}, \tag{3.1}$$

in which α is uniform in space, $\nabla\alpha = 0$, and thus serves as a parameter of the model. This condition on α and the condition $\nabla \cdot \mathbf{B} = 0$ allow us to transform Equation 3.1 into a Helmholtz equation for $\mathbf{B}$. The volume-filling fields were constructed in the half-space ($z \geq 0$) using the tangent plane approximation (i.e., in a rectilinear box tangent to a point on the solar surface) by solving the Helmholtz equation for $\mathbf{B}$ (Chiu & Hilton, 1977; Lothian

& Browning, 1995). An HMI LOS magnetogram (Schou et al., 2012) provided the boundary conditions used in the creation of these fields.

For this data set, LFFFs for 61 values of α were computed, with α equally spaced in the range [-0.05, 0.05] arcsec^{-1}. To link the information given by the photospheric extrapolation to that from the EUV data, a coronal loop is manually traced with a smooth curve. (Note that for this method we need only trace a portion of the loop. The feet of the loop need not be included.) The parameters α and h (height, distance along the LOS of a point at the center of the loop) are varied, field lines are extrapolated from the POS location of the midpoint of the trace for various values of h, and the extrapolated field line POS projections are compared to the trace. An average distance function between the extrapolation and the trace, $d(h, \alpha)$, is minimized to choose the correct model for that field line. The α-h fitting yields a 3D model of the LFFF line to which the observed AIA loop was fit, which we will hereafter call a "track." As these tracks are 3D, they can be rotated such that they can be observed from both AIA (by construction, see Figure 3.2) and STEREO (through a coordinate transformation).

As an independent verification of the α-h fitting method we now assess how well the tracks it produces match coronal loops seen from different viewpoints offered by STEREO. The track (i.e., the 3D curve produced from an AIA image by α-h fitting) is projected onto the image plane of STEREO and plotted over an EUVI image. The tangent plane approximation used in the modeling poses one difficulty in making this comparison. If the rectilinear box in which the tracks were constructed were directly transformed, then this box would still lie on a plane tangent to a point on the solar surface (see panel (a) in Figure 3.3). While near the point of tangency this was a good approximation, further away in the North-South direction we end up with the tangent plane's lower surface deviating from the true solar surface — that is, it should be on the limb.

To remedy the discrepancy in the location of the solar surface from the tangent plane,

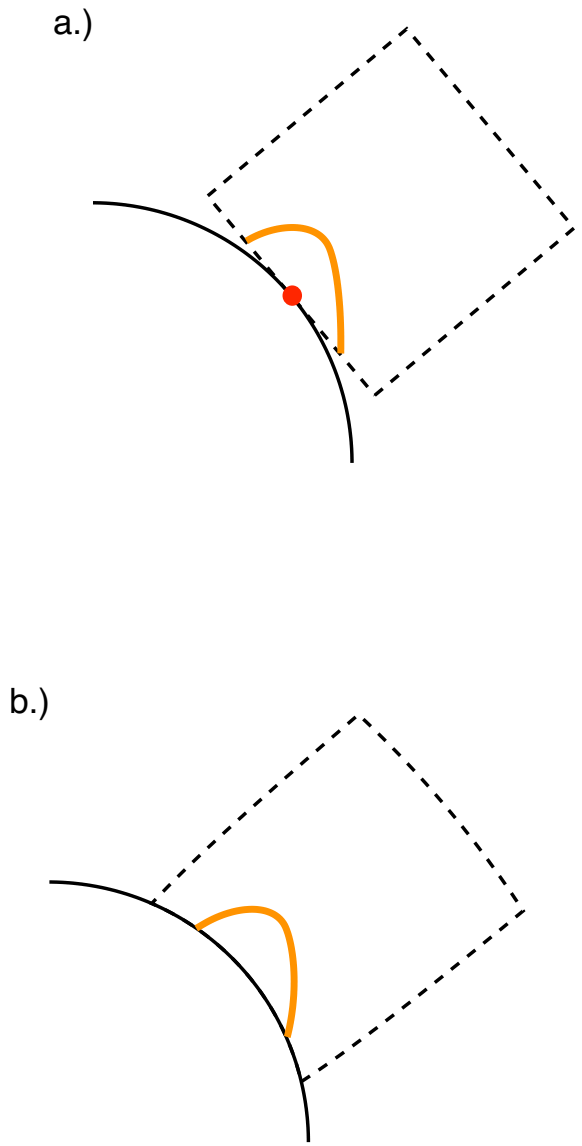


Figure 3.3: (a) Rectilinear box in which the α-h fits are constructed. The point of tangency (red circle) is the only location that lies on the solar surface. (b) Approximate shape of the box after the deformation is applied. The bottom surface of this volume now entirely lies on the solar surface, not just at the point of tangency. In both panels, a track constructed from the α-h fitting represents a coronal loop and is depicted in orange.

we apply a deformation of the rectilinear box, and therefore the track, before rotating into the new EUVI LOS. This transformation is described as follows: in the tangent plane, each point in a track is defined by the three Cartesian coordinates (x, y, z) with equivalent spherical coordinates (r, θ, ϕ). In the tangent plane model, the z-coordinate is the height above the solar surface ($z = 0$). However, only the point of tangency actually lies on the solar surface; the other points in the $z = 0$ plane lie above, $r > R_\odot$. We wish to define an r coordinate, $r_{\rm new}$, such that this new r coordinate gives the radial distance including height above the solar surface, $R_\odot$. The θ and ϕ coordinates remain unchanged while we do this adjustment. Thus, we define $r_{\rm new} = R_\odot + z$. We then transform $(r_{\rm new}, \theta, \phi)$ back into Cartesian coordinates (x', y', z') to be used subsequently. The resultant deformation is approximately shown in Figure 3.3(b), where the lower surface of the modeling volume (and the footpoints of the track) lies entirely on the solar surface.

3.4 Qualitative Comparison of Tracks to EUVI Images

To assess the fidelity of the α-h fitting, we compare the tracks with the EUVI observations to determine how well the two match in this different viewing angle. We first perform a qualitative assessment of all loops by visual inspection. The results are summarized in this section with some key examples for context[1]. Figures 3.4 and 3.5 show instances of tracks plotted on an EUVI-A and EUVI-B image, respectively. The full set of all EUVI images with the tracks overplotted can be found in the supplemental figures in the online journal[2]. Some α-h models were unable to be examined owing to the lack of EUVI data availability around the time of interest. (This is not explicitly shown in the subset of

[1]The examples in Figures 3.4–3.10 have been square root scaled with varying values for the color scale saturation for clarity purposes only. The subsequent data analysis in Section 3.5 uses intensities in units of DN s^{-1}.

[2]Note that in the supplemental figures the tracks are directly plotted over the EUVI image. As a result, in some of these figures (earlier in time for STEREO-A and later for STEREO-B) part of the track that would be behind the limb is shown on the image, and thus some observer intuition is required.

the data used to for illustrative purposes in Figure 3.1, but it would be a case of a vertical dotted line that has no red or blue vertical lines near it.) However, some models could also be viewed from both STEREO satellites. Thus, of the 199 tracks that were constructed, there are 173 to compare to EUVI images. We seek the closest underlying feature in the images to pair with each track. That is, we did not consider using one track to compare to more than one loop in EUVI. As a result, each track only gets put into one goodness-of-fit category per image. We define three categories in which we classify the goodness of fit: excellent match, maybe match, and no match. Note that one track can be placed into the no-match category when viewed in EUVI-A while still being an excellent match in EUVI-B, for example; we found 33 tracks with some variation of this. There were a total of 173 tracks that coincided with the EUVI dataset, with 8 that could not be compared to the data (i.e., some loops were entirely hidden behind the limb). As some saturation in EUVI data made fine structure unresolvable, 14 tracks were further removed from consideration owing to tracks being entirely within the saturated area. Of the 151 tracks that were viable for visual comparison, 40 (26.5%) were excellent match, 65 (43%) were maybe match, and 46 (30.5%) were no match.

To assign a track to one of our goodness-of-fit categories, we used the following reasoning. For an excellent match, a track would follow a loop in EUV along the loop's axis over at least enough of the visible structure for it to be convincingly and appropriately compared. In Figure 3.6, we classify both the green and orange tracks excellent matches from their close alignment with a coronal loop structure. This is despite the ambiguity in resolving the two structures individually. Since the two tracks are so close in this perspective, it is possible that the visible loop includes both, or only one.

If the track was on the low- or high-altitude edge of the structure, or otherwise did not align completely with the observed loop, we called this a maybe match. Maybe matches were also assigned if the track fit within saturation on the image reasonably but could not

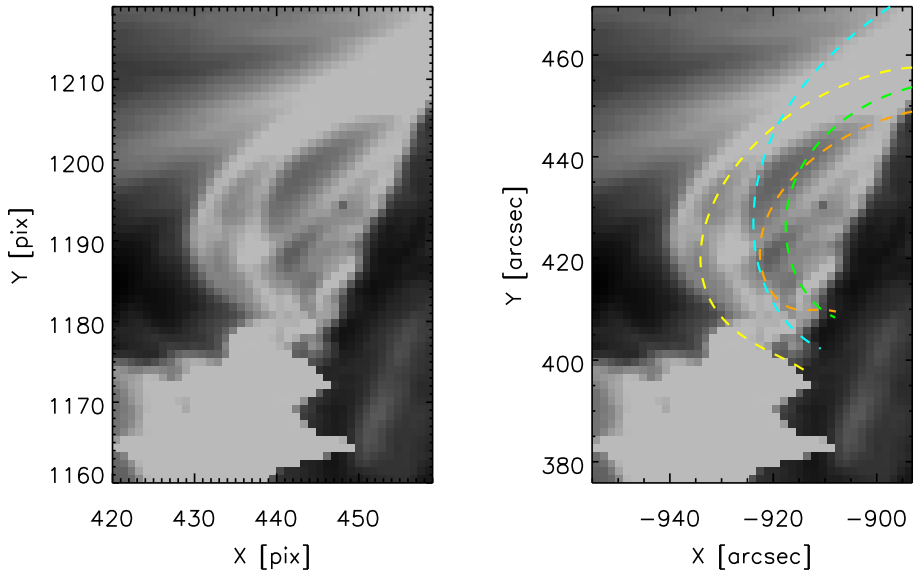


Figure 3.4: An image taken from EUVI-A 171Å with the corresponding tracks plotted over. The complete figure set (18 images) is available in the online journal.

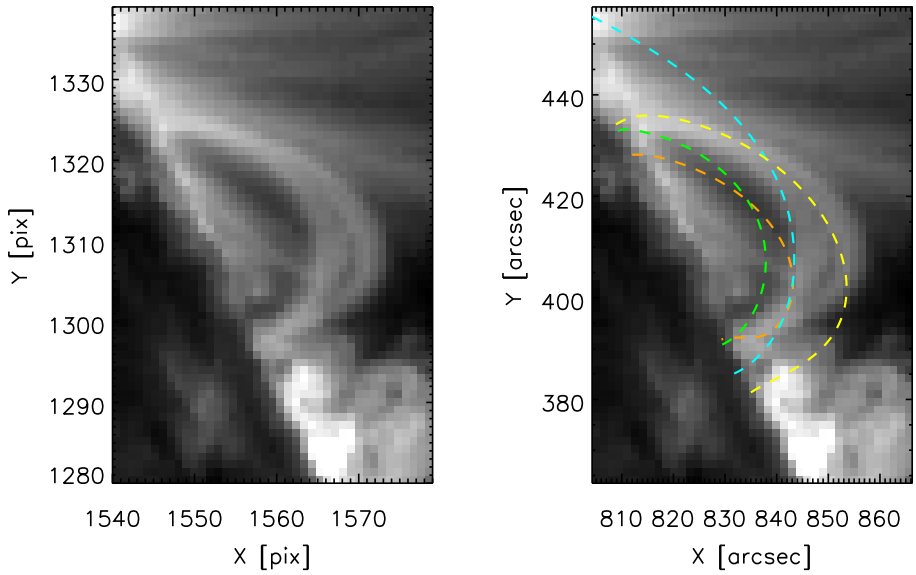


Figure 3.5: An image taken from EUVI-B 171Å with the corresponding tracks plotted over. The complete figure set (26 images) is available in the online journal.

be matched to finer structure. For an image with saturation in the region of interest, like in Figure 3.7, we assign the three tracks into the following categories. The cyan track fits believably within the saturation but is otherwise unable to be further resolved and was removed from consideration, while the others (green, orange) are considered maybe matches as they trace the low-altitude edge of the saturation and correspond to some of the other bright features. Other maybe match examples are also shown in the yellow tracks of Figures 3.4 and 3.5. These tracks are not quite aligned with the EUV structure, but they are aligned enough to be maybe a match.

The no-match category was populated with tracks for which we did not see EUV features to which they corresponded. Not included in any category, nor in the total count, were tracks whose position relative to the LOS made it impossible to compare them with structure in the corona. An example can be seen in Figure 3.8, where the low-lying cyan track lives on the far side of the limb entirely and the disk blocks any view of it from this LOS. As in any sort of qualitative analysis, there is a level of subjectivity involved. Thus, we invite the reader to look at the supplemental figures and draw one's own opinion.

In general, the co-alignment of the tracks to the EUVI observations fits well. Together the set of excellent matches and maybe matches exceeds the amount of no matches. One might expect more discrepancy between the model and observation owing to the lack of temporal precision between the data from AIA (used in the fitting) and the data from EUVI (used to observe); that does not seem to be the case. We also find that the EUVI data (particularly from the A spacecraft) are very saturated. Without saturation in the data set, we might be able to turn maybe matches into excellent matches.

We find that certain types of loops are particularly well fit by the α-h fitting method. These loops share a similar-looking morphology, appear to have their feet anchored at similar locations, and rise to similar heights in the atmosphere. The green and orange tracks in Figure 3.6, the purple track in Figure 3.9, and the orange track in Figure 3.10 are examples

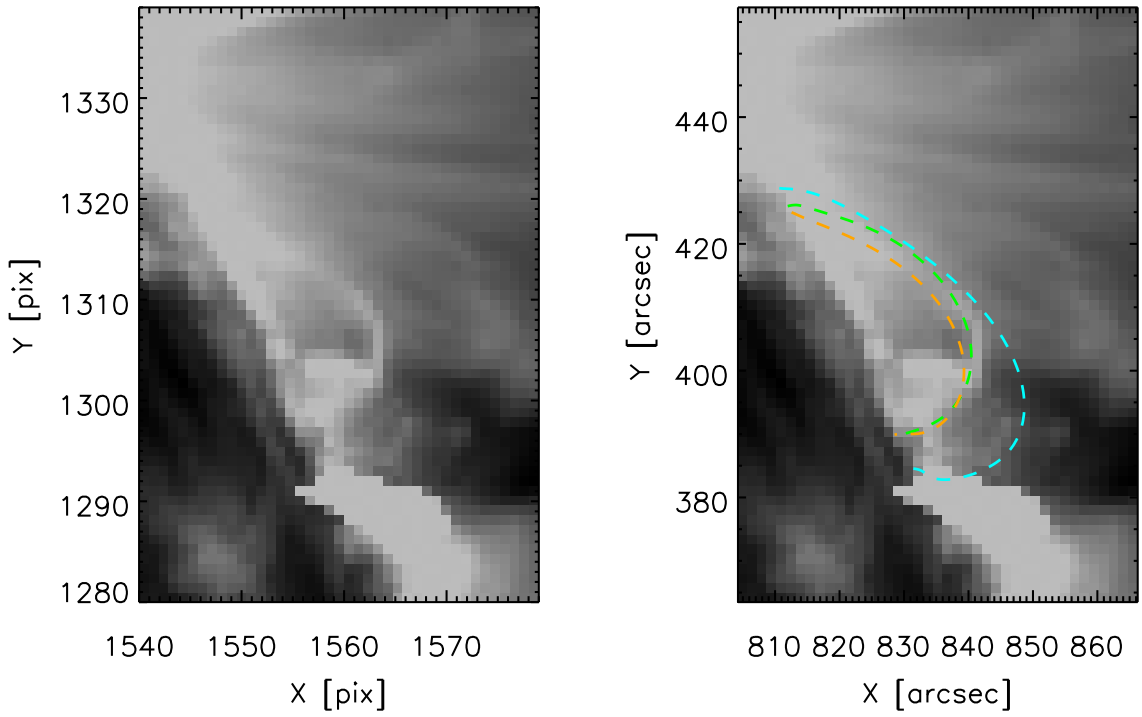


Figure 3.6: We call both the green and orange tracks excellent matches to the EUV features observed with EUVI-B 171Å, despite the possibility for ambiguity between them.

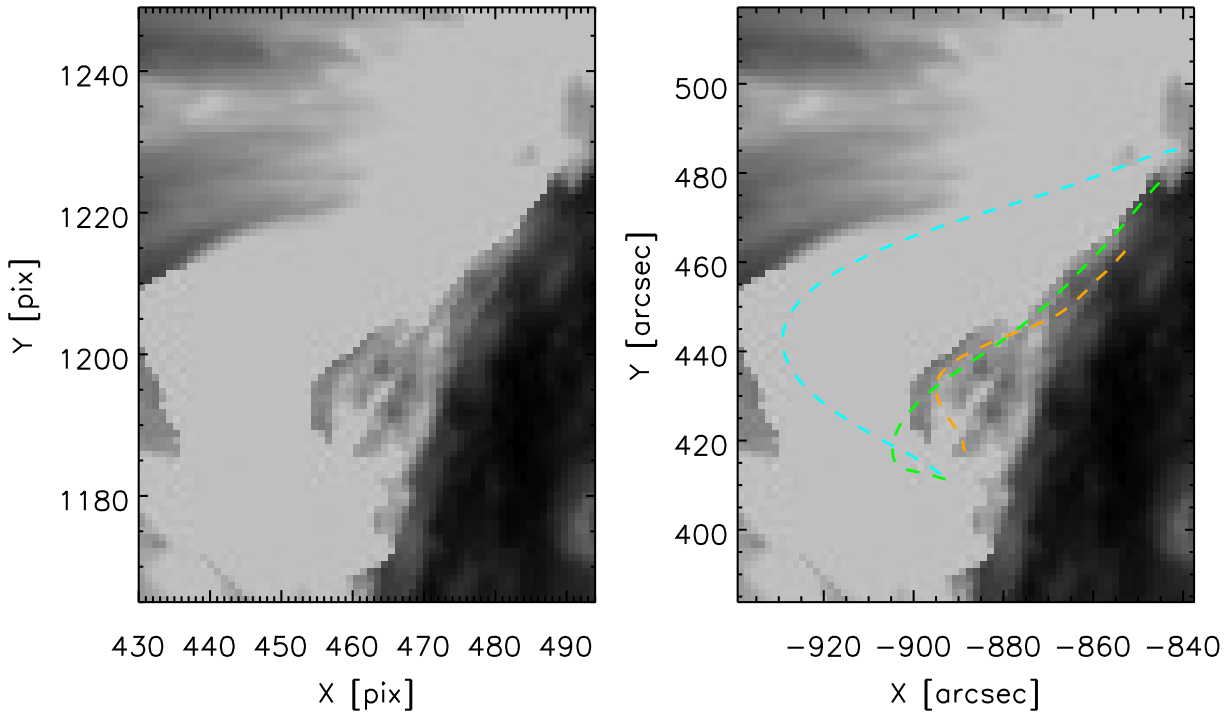


Figure 3.7: Two tracks in this example are labeled maybe matches to features in EUVI-A 171Å. The green track lies on the low-altitude edge of the saturation. The orange track also is on the low-altitude edge of the saturation, and there are some bright features to which it conceivably aligns. The cyan track lies believably within the saturation but is removed from our statistics, as features it might correspond to cannot be resolved.

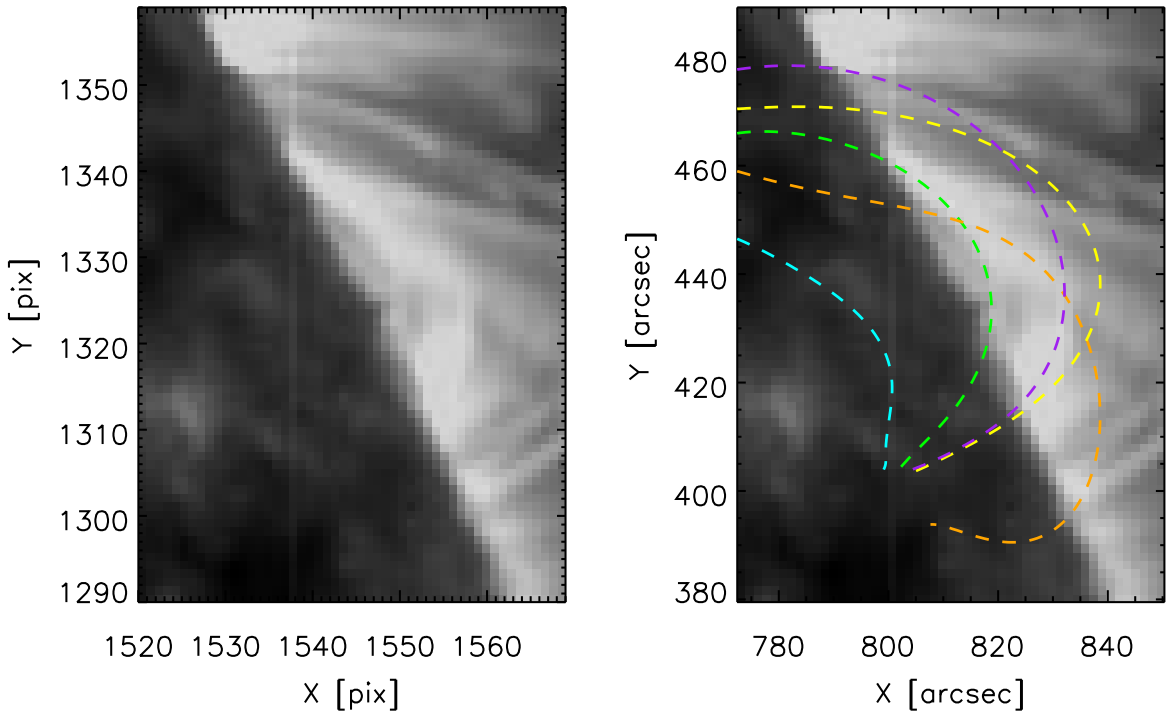


Figure 3.8: At this point in time, the feet of the loops lie on the other side of the limb. Therefore, the low-altitude portions of the tracks (including the entire cyan track) are obscured owing to the disk. Tracks like the cyan loop are then excluded from consideration in the visual analysis.

of this well-fit group. Their particularly good matching might be explained by the general topological structure of the 3D field. The aforementioned loops all lie in a similar location, and, more significantly, they belong to the same magnetic domain identified in the magnetic modeling of Longcope et al. (2020, see their Figure 4). These particular tracks connect between the polarities identified by Longcope et al. (2020) as P06, P07, and P08 (adjacent parts of the same photospheric flux) to N10 (see the purple track in Figure 3.2). The flux partitioning may occur in such a way that the domain that contains these morphologically similar loops has a very good fit to the LFFFs.

A loop's inclination with respect to the local vertical allows for the possibility that there is some dependence on how well it is observed as a result of the angle used to view it. Following this line of thinking, there might be some trends between inclination angle of the track and the goodness-of-fit category in which it was placed. We tested this by calculating the tracks' angle of inclination. Our analysis finds no such consistency, as most of the tracks — and, by inference, the loops to which they correspond — in this study were quasi-vertical. The aforementioned morphologically similar tracks (belonging to the excellent match category, and residing in the same domain) had a range of inclination angles, approximately 5° to 30° with respect to the local vertical. We found similar ranges in the maybe-match and no-match categories as well.

3.5 Quantitative Analysis of Loops Using Gaussian Fitting

Following the qualitative assessment of alignment, we select a subset of high-quality examples for more quantitative analysis with regard to the loop location and width. We would like to compare these quantities more precisely. We develop and apply a methodology in order to overcome analytical difficulties within our data. First, though we know the track's location in the POS, we do not know the exact axis of the loop and therefore its location in the POS as defined by the EUV emission. Additionally, we would like to measure both

the loop's location and its width without bias or error from an incorrect guess as to the axis direction as informed by the track. For example, it is likely that the direction perpendicular to the track is not the width we would like to measure for a misaligned track/loop in the maybe-match category.

Two particularly illustrative examples are given in Figures 3.9 and 3.10. The example in Figure 3.9 assigns the purple and green tracks to the excellent match category, orange is a maybe match, and the yellow and cyan tracks are assigned to no match. The purple track (hereafter called Example 1) and its underlying feature are particularly well suited to detailed quantitative analysis. Figure 3.10 has two no matches (cyan and green) and one maybe match (orange). The orange track seems to lie on the high-altitude edge of a coronal loop, and we will investigate this in further detail as well. We call the orange track Example 2. In Figure 3.1, the instance of Example 1 is denoted by the purple star, and the orange star is that of Example 2.

The data set contained a small sample of 11 tracks that we considered suitable for comparison to the observed loops in this sort of quantitative analysis. This was due to issues with the images in EUVI, including saturation and overlapping bright features making a particular trace not resolvable. Of these 11, 9 were observed from one EUVI and AIA and 2 were observed from EUVI-A, EUVI-B, and AIA simultaneously. In total, 13 track/loop pairs were examined. In this subset of the data, there is a one-to-one correspondence between a track and the matching loop.

3.5.1 Methodology

To address the concerns described above, the quantitative fitting for each EUV loop (which corresponds to a track) is conducted as follows. We begin with a point in the track called the POI (see the cyan star in Figure 3.11). We then identify a circle of radius r and extract the intensity values from the pixels along its perimeter. From this array of values

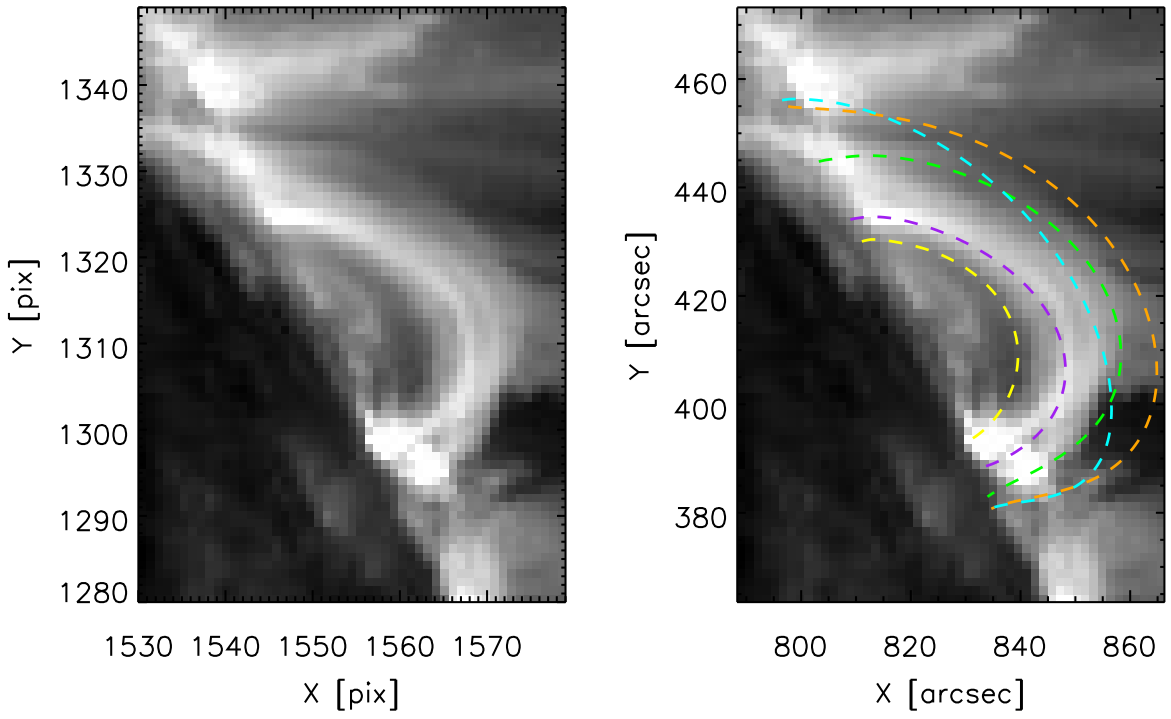


Figure 3.9: This instance of α-h fitting resulting in these tracks is denoted by the purple star in Figure 3.1. The purple and green tracks were categorized as excellent matches and trace out loop structures, though the corresponding feature to the green track is fainter than that which matches the purple. The purple trace and the EUV feature to which it corresponds are referred to as Example 1. Note that the colors in this figure correspond to the same track colors in Figure 3.2.

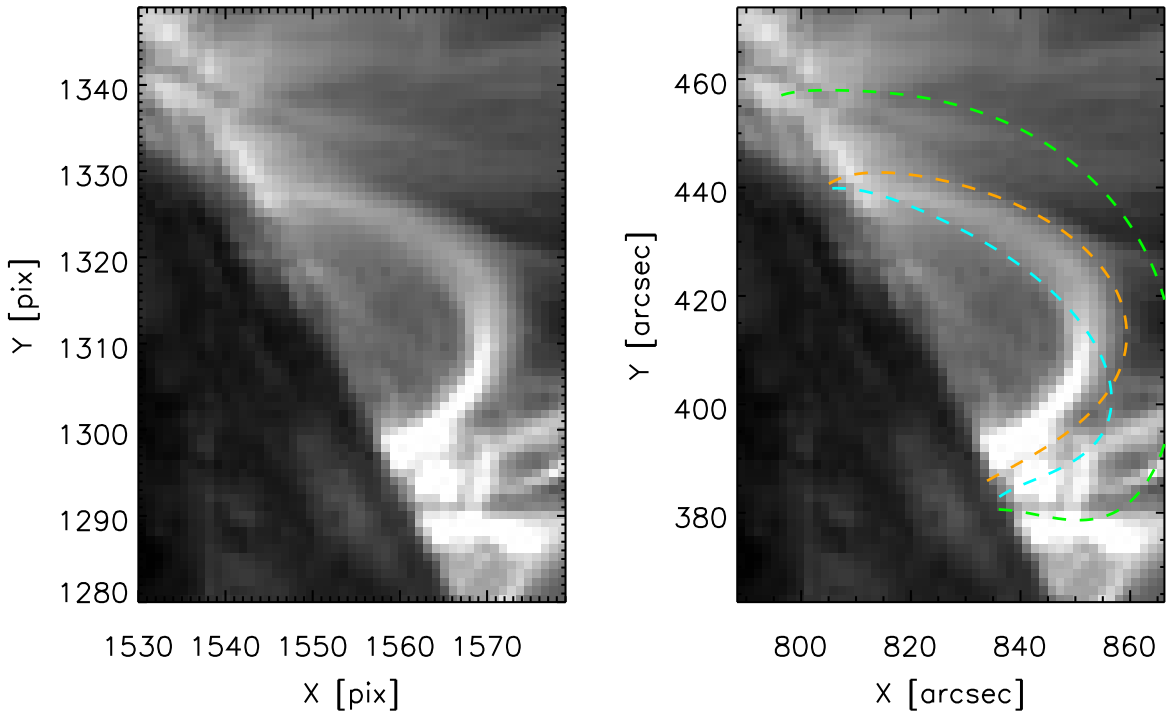


Figure 3.10: Both the cyan and green tracks for this example belong to the no-match category. The orange track is determined to be a maybe match. Though it does not align completely along the loop's axis, it consistently traces out the high-altitude edge of the feature. We refer to this orange track as Example 2. In Figure 3.1, this time is marked by the orange star.

we identify two local maxima as the axis or spine of the loop. Between pairs of maxima, on both sides, we then find the minimum intensity value in this range. These two minima we call the "edges."

We repeat this for circles with radii in the range from 1 to n pixels. The number of circles used, n, varied for each track based on the data around it. In Figure 3.11, the middle panel shows six of these circles over an EUVI image, with the cyan star designating the POI. The right panel of the figure shows the POI with the maxima locations plotted with green plus signs and the edges plotted with yellow plus signs.

The intensity values of the edges are then used to perform a Gaussian fit. As in Figure 3.12, for all the edges we plot the intensity value of the edges versus the radius of the circle used. The intensity of the POI is also on this plot at $r = 0$, plotted again with a cyan star. Each circle has two edges that we designate positive and negative and hereafter assign position $x = +r$ and $x = -r$. We perform the Gaussian fit to this plot using the IDL function `GAUSSFIT`. Five terms (A, B, C, D, E) were used for the Gaussian such that

$$f(x) = Ae^{-\frac{(x-B)^2}{2C^2}} + D + Ex \tag{3.2}$$

and with initial estimates of A = intensity of POI, $B = 0$, $C = 2$, D = mean of all the intensities, and $E = 0$. The estimates aided `GAUSSFIT` in fitting the Gaussian near the POI as opposed to centering the fit at larger values of r that may have large intensity values. The large intensities at larger radii are likely to be other structures, as we expected the loop to be centered around the POI. The centroid is given by the parameter B, which often differs from B=0 (the original POI). The full width at half maximum (FWHM) of the fit is what we call the loop diameter and is computed

$$2\sqrt{2\ln(2)}C.$$

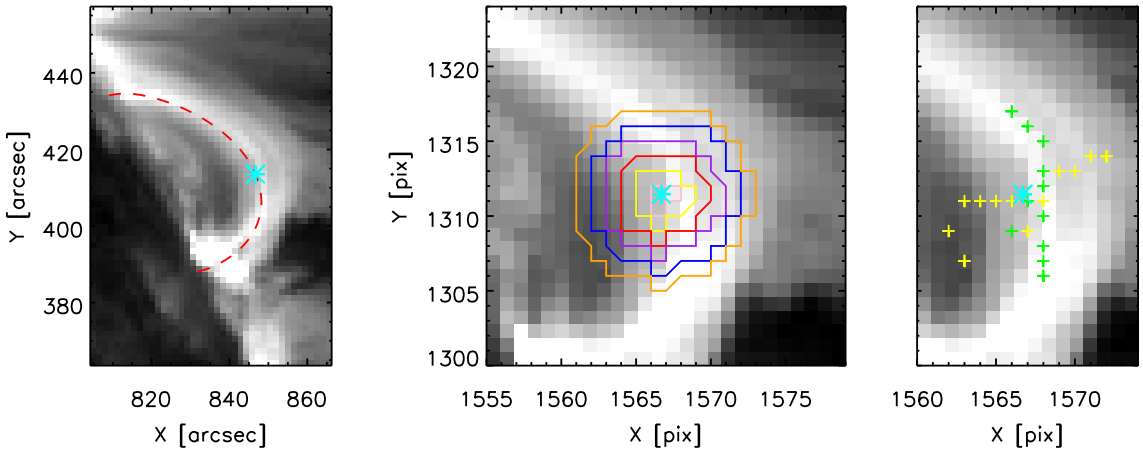


Figure 3.11: Left: the track (red line) shown here is the same as Example 1 (Figure 3.9, purple). A particular POI along the track is denoted by the cyan star. Middle: six concentric shapes are shown. These shapes are determined from drawing a circle and matching the perimeter of the circle to the nearest pixel. These pixels are the ones whose intensities are used to find the maxima and subsequent edges. Right: maxima along the perimeter of each of the six circles are shown with green plus signs, and the corresponding edges are plotted with yellow plus signs.

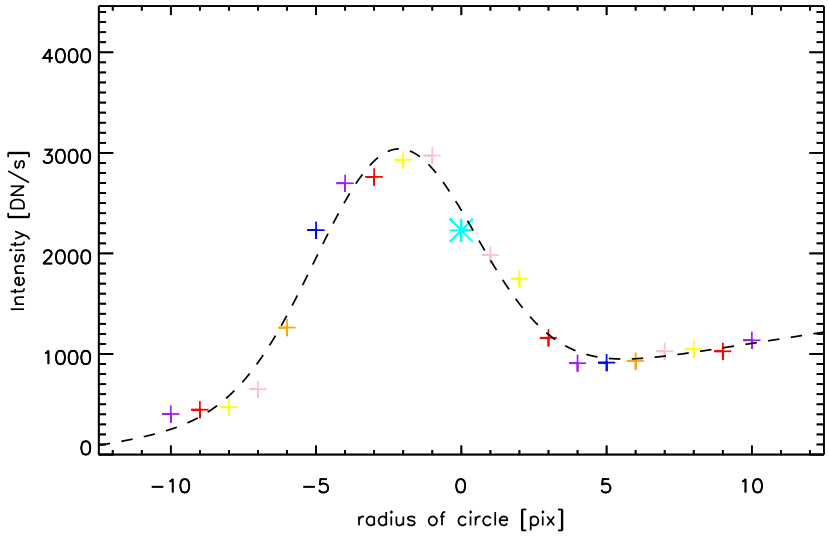


Figure 3.12: Example plot showing one instance of the intensity of the edges (plus signs) and the POI (cyan star) vs. radius of the circle used (different colors). This particular instance used 10 concentric circles and their edges. These data were then used to fit a Gaussian (dashed line).

This process — which has been described for a single POI — is repeated along the length of the track. As each track is defined by a set of (x, y, z) coordinates, each point along the track has its corresponding location in both the AIA and EUVI FOVs. We progress through all points that define the track, doing the Gaussian fitting using that point as the POI. For each point along the track, we have multiple values for observed diameter. Each value is from a different spacecraft/LOS, but they all correspond to the same 3D location along the track.

We find that this method is comparable to that of "straightening" the loop. In such an analysis (as in Aschwanden et al., 2008; Watko & Klimchuk, 2000; Winebarger et al., 2003) a curve is traced on the image and then the data are interpolated into an array in which the coordinate system has one vector that is locally parallel to the curve and a second that is perpendicular to the first. Figure 3.13 shows the diameter comparison between the two methods using similar parameters. The track was used as the curve to which the coordinate system ran parallel and perpendicular. The same Gaussian fitting method was performed for each row (intensity profile) in the interpolated array as in our concentric-circle method. There is good agreement between the two in the well-fit region. (The determination of this well-fit region is detailed in the next section.)

Our method provides us with two advantages over this other method. First, we do not have to interpolate the imaging data. Second, our method allows us to use our theoretically derived tracks, without requiring the identification of a more accurate loop axis independently. A track is based on a magnetic model of the field line and found in Section 3.4 to match reality imperfectly. Therefore, in order to apply the other method, we would need to take the additional step of tracing the actual loop axis through each image, defining a curve along the loop to be straightened.

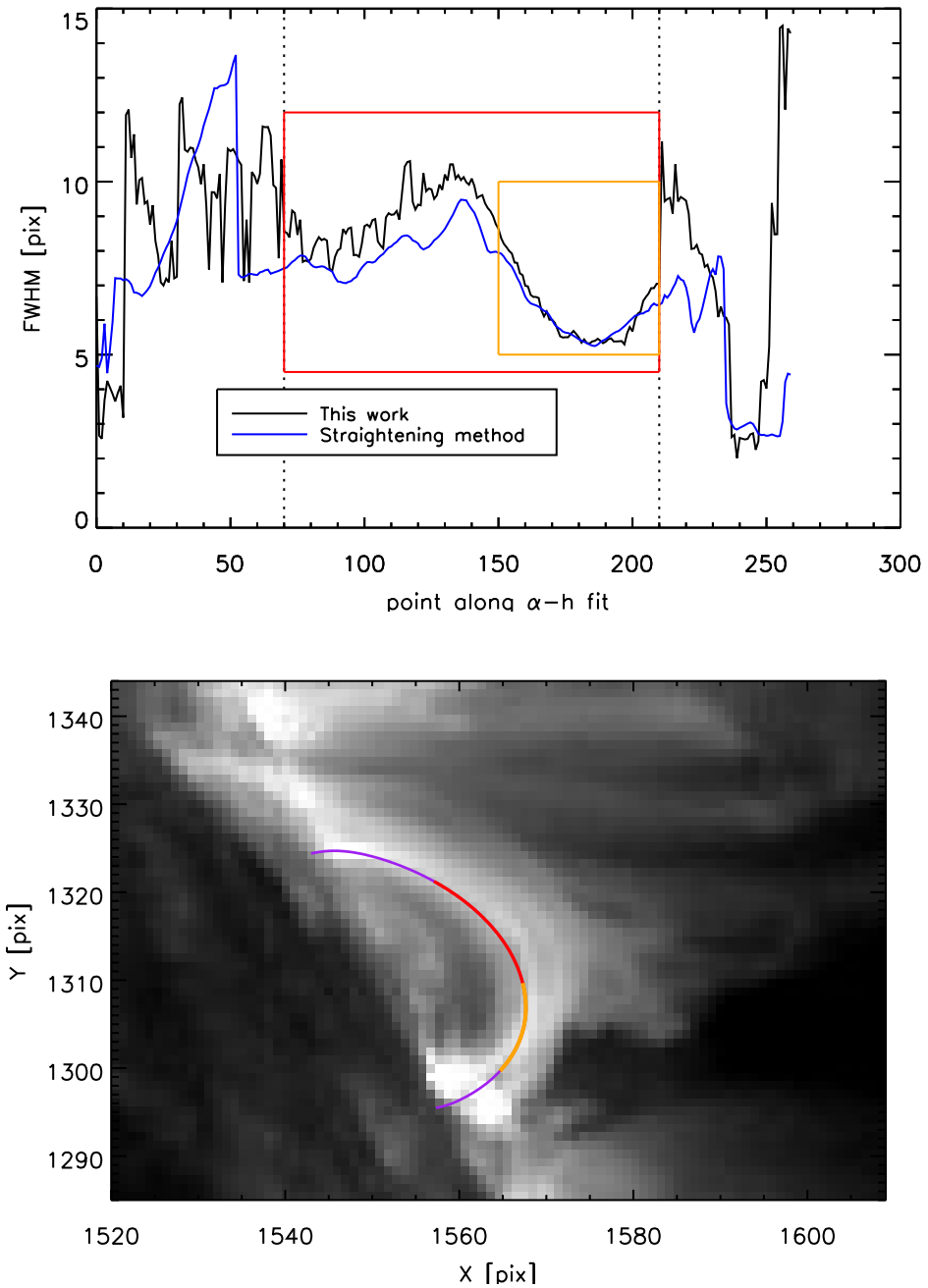


Figure 3.13: Comparison of this work's concentric-circle method (black) with that of straightening the loop (blue). The red box shows original region of good fit, and the orange box encloses a region of excellent agreement between the two methods. The regions in the red and orange boxes in the top panel correspond to the same color of the track in the bottom panel.

3.5.2 Centroid

We use the centroid of the Gaussian fit to assess how well the tracks fit to features in EUVI. This analysis bolsters and quantifies the original visual evaluation. The position $r = 0$ (see Figure 3.12) corresponds to the POI, located where the AIA track is projected. If the Gaussian fit returns parameter $B = 0$, then the axis of the EUVI loop coincides with the POI exactly. Any nonzero value indicates a discrepancy. The centroid value was also used as a proxy in determining how well the Gaussian fit the data. For example, significant fluctuations in the centroid value (as a function of location along the track) indicated that the Gaussian fitting was not locked onto a consistent structure. We see this sort of fluctuation for Example 1 in the left panel of Figure 3.14, at both ends of the track. The companion image (Figure 3.9) shows bright features, which are not necessarily the loop in which we are interested, around the feet of the track. In the region in which the track was well fit (denoted by the region between the vertical dotted lines in the left panel of Figure 3.14), the median deviation from the POI was approximately -1.1 EUVI pixels. For Example 2 (Figure 3.10), the median deviation from the POI (in the region in which we believed the track well fit, between the dotted lines) was about 3.2 EUVI pixels (see the left panel of Figure 3.15). For the other tracks, in the regions of believable fit, the absolute median deviation from the POI was in the range of $[0.04, 4.5]$ EUVI pixels. The median of all medians was 0.77 pixels. These values are within typical loop diameters, which is further evidence in favor of the validity of the fitting. This confirms that this subset of tracks were very will fit to loops in the EUVI image.

3.5.3 FWHM

The diameters we obtain from the FWHM of the Gaussian fitting from multiple angles allow us to investigate how the diameters change at the same point along the track owing to the instrument and LOS. The diameters from the fitting were corrected for using the

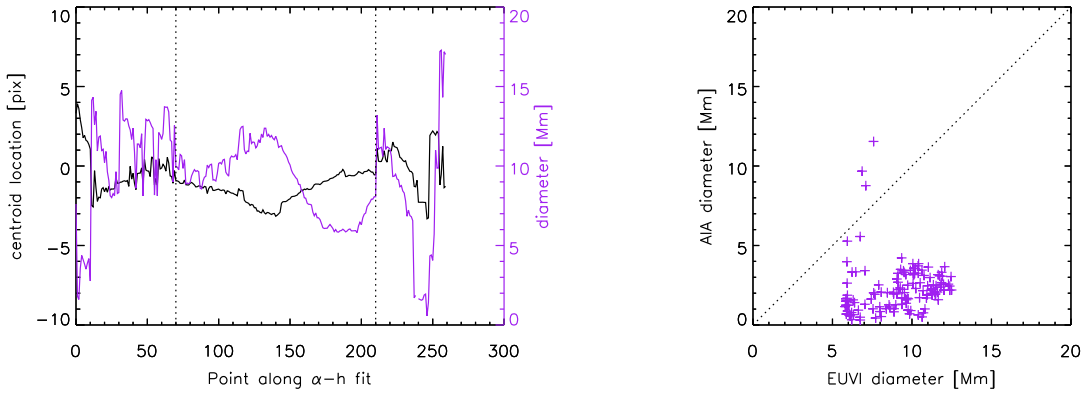


Figure 3.14: These plots correspond to the quantitative fitting methodology applied to Example 1 (purple loop in Figure 3.9). Left: plot from EUVI data of centroid deviation from POI location (black) and diameter of the loop (purple) as a function of the point along the track. The region between the dotted lines is the well fit region. Right: scatter plot of EUVI diameter vs. AIA diameter for the points within the well fit region. The statistic Spearman's ρ =0.226 ($p = 7.1 \times 10^{-3}$) for this distribution.

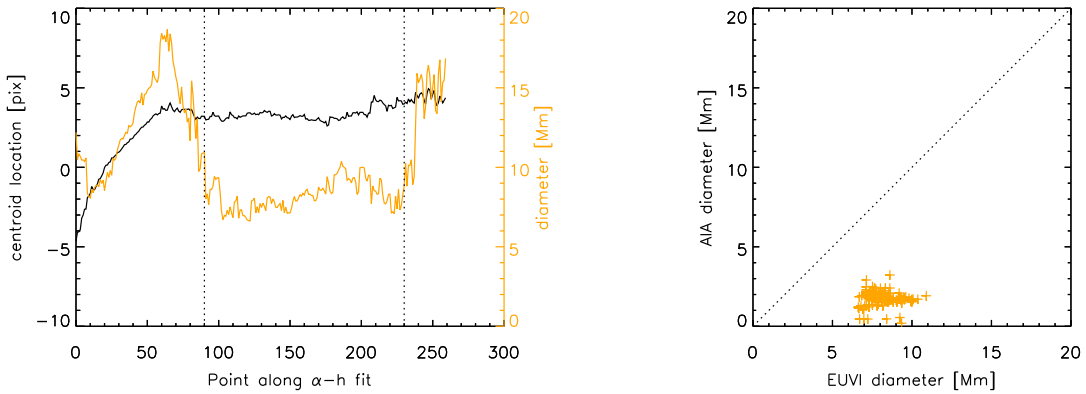


Figure 3.15: These plots correspond to the fitting method applied to Example 2 (orange loop in Figure 3.10). Left: centroid deviation from POI (black) and FWHM loop diameter (orange) as a function of the point along the track as viewed from EUVI. The region between the dotted lines is the well fit region. Right: scatter plot of EUVI diameter vs. AIA diameter for the points in the best fit region. The Spearman's ρ statistic is -0.13 ($p = 0.1$) for this distribution.

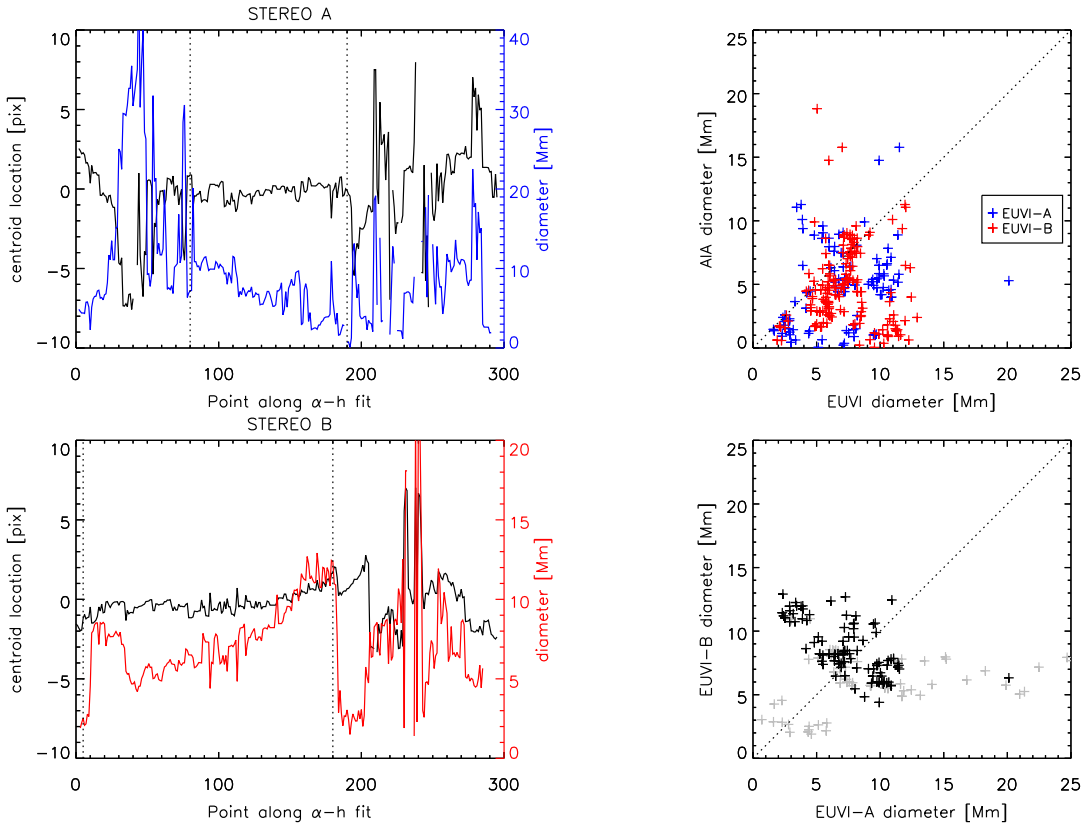


Figure 3.16: Example of our analysis for a loop viewed with EUVI-A, EUVI-B and AIA simultaneously. As in previous figures, the regions of good fit are between the dotted vertical lines. This example is the yellow track shown in Figures 3.4 and 3.5. Left: centroid deviation (black) and FWHM loop diameter (color) as a function of distance along the track for EUVI-A (top/blue) and EUVI-B (bottom/red). Top right: scatter plot of EUVI and AIA diameters in the region between the dotted vertical lines for both EUVI-A (blue) and EUVI-B (red). Bottom right: scatter plot comparing the diameters of EUVI-A vs. EUVI-B. The grey plus signs are in the well fit region in one instrument. Black plus signs are POIs that are well fit in both. The statistic Spearman's $\rho = -0.392$ ($p = 2.05 \times 10^{-8}$) for all plus signs, and $\rho = -0.647$ ($p = 2.55 \times 10^{-13}$) for black plus signs only.

instrumental point spread function (PSF; FWHM of 2.2 EUVI pixels and 2.4 AIA pixels, respectively; Aschwanden et al., 2008; Grigis et al., 2012) and converted to Mm. As in the previous section, the regions of good fit were informed by the behavior of the centroid. These regions of good fit are again between the dotted vertical lines in the left panels of Figures 3.14–3.16. For all POIs in the regions of good fit, the AIA diameters were plotted against the corresponding EUVI diameter. These are seen in the right panels of Figures 3.14 and 3.15, and the top right panel of Figure 3.16. In general, across all tracks in the set, we find no consistent trends in the observed diameter as a function of distance along the track. However, this could be attributed to the track-to-track variation in what portion was well fit to the data; trends may be obscured owing to looking at different portions between tracks.

For these examples and for the other cases in general, we find systematically larger diameters as determined from EUVI. We define a ratio of median EUVI diameters to that of the AIA diameters in the well-fit region. For Example 1 (Figure 3.14) this value is 4.52, and for Example 2 (Figure 3.15) it is 4.59. For all examples, the diameter ratio statistic is in the range $[1.36, 9.18]$ with a median value of 2.20. This median value is similar to the ratio of the EUVI to AIA plate scales, 2.65. Thus, though we find the values for EUVI diameters to be consistently larger than those from AIA, we cannot discount that the difference in the instruments themselves accounts for this discrepancy. However, we can propose another interpretation: though there is nothing special about the Sun–Earth line, the LOS from AIA aligns with the direction radially outward from the Sun while EUVI's LOS is perpendicular to that. As the loops (and tracks) have a significant portion mostly in the radial direction, it is possible that the viewing angle does play a role if the loop expands anisotropically with special consideration for the $\hat{r}$ direction. Further, the sparseness of the intensity information due to the resolution of EUVI with respect to the Gaussian fitting may lead to an overestimation of the diameters in EUVI. A slight dip in the intensity/radius curve (see Figure 3.12) that may be indicative of two different structures in close proximity

on the POS might be ignored by this particular fitting procedure.

Despite these possible shortcomings, we find loop widths in this study similar to others reported in the literature. The range of median loop diameters was $[0.72, 10.43]$ Mm, with median value of all median diameter values of 2.07 and 6.61 Mm for AIA and EUVI, respectively. In a study using the same loop catalog and AIA data, McCarthy et al. (2019) found that the median of all median diameters was 5.9 Mm. However, they noted that their method of boxcar smoothing the intensity profile from which the loop widths were found might lead to an overestimation of diameters and further neglected to account for the instrumental PSF. In other studies of loop widths with AIA and TRACE (as in Aschwanden et al., 2013; Aschwanden & Nightingale, 2005; Aschwanden et al., 2000; Longcope et al., 2005; López Fuentes et al., 2006, among others) the ranges of widths were comparable to those obtained in this study. The width distribution from Hi-C reported in Brooks et al. (2013) peaks at 0.272 Mm with range $[0.09, 0.973]$ Mm, but that instrument has significantly higher spatial resolution. There are some instances where some of the derived loop diameters are too large (as in Figure 3.14 or 3.16). Due to the limitations in loop selection by both the believability of track-loop matching and the quality of the data, some amount of outliers in deriving widths of loops could not be completely eliminated. However, we sought to insulate our results as best as possible by looking at overall trends instead of individual data points.

Though we derive some amount of diameter variation over the length of the loop, our results cannot say anything definitive about loop expansion overall. Previous studies using SXT (Klimchuk, 2000; Klimchuk et al., 1992) and TRACE (López Fuentes et al., 2006; Watko & Klimchuk, 2000) have concluded that there is a slight increase in a loop's width at its middle when compared to its ends. As our regions of good fit tended to include the middle of the loop and exclude the ends, we cannot make a direct comparison. Considering shorter segments of loops might put a lower limit on loop expansion. However, even within our well-fit regions we have changes in loop diameter of up to a factor of 2. Though some

amount of width fluctuation over short distances has been reported ($\sim$ 25% of the loops' average width; López Fuentes et al., 2008), what we find here is much larger. Other studies may make the decision in their selection of loops to choose those that are well isolated from the background. In this work, the trade-off for having our viewing angles almost in quadrature with loops above the limb in our second viewing angle means some compromise for possible overlap of these EUV features along the LOS. We also see through more of the solar atmosphere looking on the limb versus on the disk. This would be a factor in seeing variation in loop widths on the limb owing to the LOS passing through more material (as in the EUVI angles in this work), in comparison to looking straight down at loops (as in the AIA images). The AIA observations do, in fact, have only slight to negligible variation in their widths along the loop.

We find anticorrelations for the AIA versus EUVI diameter plots in 7 of the 13 track/loop pairs. For this subset, it would be difficult to explain this behavior were the cross sections circular. Therefore, the anticorrelated behavior opens the possibility that the loops are elliptical (Longcope et al., 2020). For two viewing angles approximately 90° apart, an elongated object would appear larger from one perspective than the other. Such a thing would produce the anticorrelation that we observe.

Figure 3.16 presents a special case, where the data from STEREO-A, STEREO-B and SDO are adequate for simultaneous analysis. The example analyzed in this figure is the yellow track from Figures 3.4 and 3.5. Both track/loop pairs belong to the maybe-match category. As such, we have the unique ability to compare the diameters not only between AIA and EUVI but also between the two STEREO spacecraft. The bottom right panel of that figure is a scatter plot of the EUVI-A diameter versus EUVI-B. As the regions of good fit are not exactly aligned for the track in the two different instruments, the gray plus signs are the well-fit locations along the track in one instrument, while the black plus signs are well fit in both. The median diameter ratio of A to B is 1.10 for all points and 0.88 for the

black plus signs only. We note that the ratio statistic for all points is larger in part owing to more saturation in the A image.

We find a negative correlation for both black plus signs and the set of all points. The previous discussion of anticorrelation would not apply if the spacecraft were 180° apart. Though the spacecraft are nearly out of phase, they are not precisely 180° apart. This leaves the possibility open that the slight difference in the respective LOS of the spacecraft and geometry of the coronal loops (i.e., the loop does not have an isotropic, cylindrical cross section) leads to the difference in diameters. Though this is one explanation for the anticorrelation between the diameters obtained from the two STEREO vantage points, there may be other mechanisms at work.

3.5.4 Diameter and Intensity Comparison

Additional evidence of elliptical cross sections can be found by comparing loop diameter to brightness. For a loop expanding nonisotropically along its axis but with a constant filling factor, we would expect narrower sections to be bright and for wider sections to be dimmer. That is, if we view one loop along the direction of its major axis, our LOS passes through more emitting material in the optically thin corona and appears brighter than if viewed along the minor axis. To elucidate this hypothesis, we examined how our Gaussian fitting parameters A (Gaussian peak, used as a proxy for intensity) and FWHM compared. A plot of this behavior for Example 1 as fit from the EUVI data is shown in Figure 3.17. Though this is the most dramatic example of this type of behavior, a significant fraction of loops exhibit an anticorrelation between FWHM diameter and intensity for EUVI. That being said, we note that Example 1 does not exhibit the anticorrelated behavior demonstrated in the diameter–diameter plot in the right panel of Figure 3.14.

Our result seems to contradict some previously reported results. Analysis of loops observed in 193Å with Hi-C by Klimchuk & DeForest (2020) found either uncorrelated

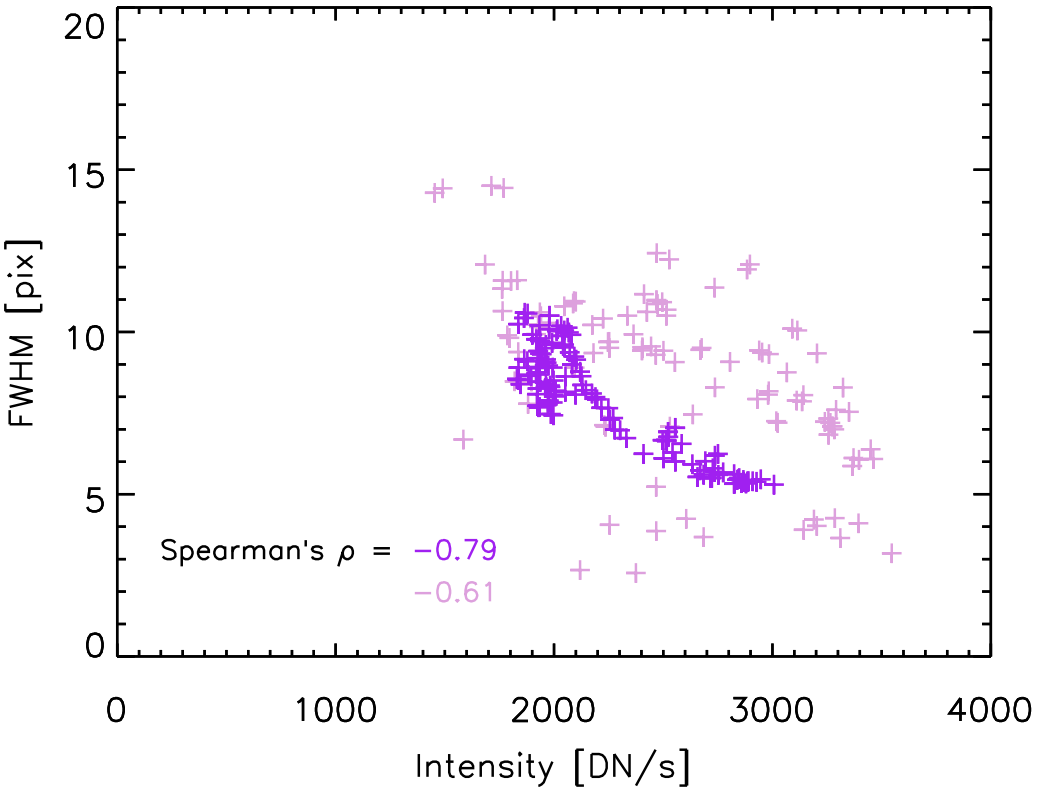


Figure 3.17: Scatter plot showing the relationship between the intensity and width of the loop at all POIs that define the track in EUVI for Example 1, for which there is a negative correlation. The dark purple plus signs are the points in the well-fit region with Spearman's $\rho = -0.79$ ($p = 7.4 \times 10^{-32}$). All fits along the track include the light-purple data points, and for the entire plot $\rho = -0.61$ ($p = 9.0 \times 10^{-28}$).

or positively correlated behavior of intensity versus widths. They cited these results as evidence of approximately circular cross sections in the examined loops but did not extend this inference to loops universally. The results we present in this section are the inverse of those results; we find that our intensity and width measurements are more likely to be uncorrelated or inversely related.

This discrepancy may be attributed to observational wavelengths (which itself would select different populations of loops on the basis of temperature) or to the nature of the loops of interest themselves. Observations in 193Å ($\log(T) = 6.2$ K) pick up hotter plasma than

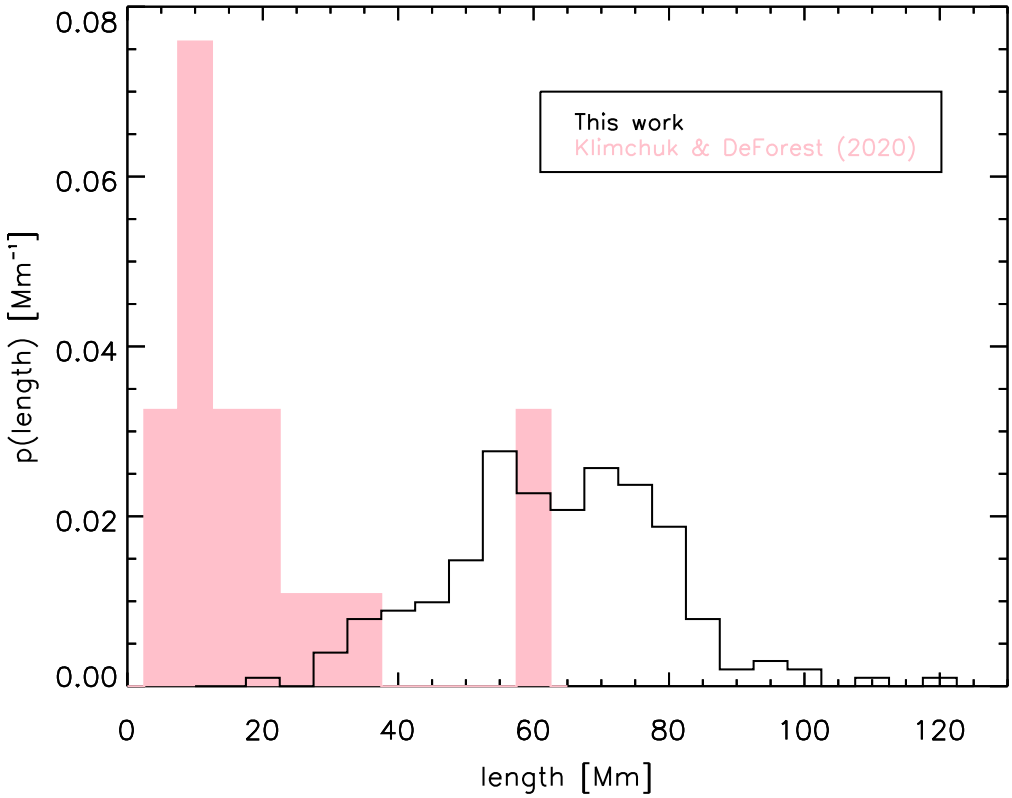


Figure 3.18: Histogram comparing the lengths of loops observed in this study (black) to those of Klimchuk & DeForest (2020, pink, see their Table 1). These data have been normalized such that the y-axis shows the value of the probability density function. Klimchuk & DeForest (2020) in general examined shorter loops (22 loops total) than those herein (151 loops).

those taken in 171Å ($\log(T) = 5.8$ K; Lemen et al., 2012). Further difference in these data sets might be attributed to the sizes of the studied loops. The length differences between the populations can be seen in the histograms plotted in Figure 3.18, where black shows loops from this work and pink show those from Klimchuk & DeForest (2020, pink; see their Table 1). Generally, Klimchuk & DeForest (2020) examined shorter loops when compared to this study. Both the Hi-C resolution was finer and the FOV was smaller than with AIA or EUVI.

In the respective well-fit regions of the 13 track/loop pairs viewed in EUVI, 6 had a negative value for ρ, and 4 had $\rho < -0.4$. Those cases with $\rho > 0$ covered the range $[0.007, 0.870]$, but tended to cluster around the range's minimum and maximum values. The instances of fitting from AIA do not exhibit such behavior consistently. The results of the diameter/intensity correlation were scattered enough such that we could not be conclusive about the trends observed with this spacecraft for these data.

The lack of an anticorrelation in the AIA intensity versus diameter on its own would not be evidence of anisotropic cross sections. When combined with the anticorrelated behavior of the EUVI observations, we see changing diameters from one perspective but not from the other. This might be further evidence of anisotropic expansion or some other mechanism in which a changing aspect ratio is observed.

3.6 Conclusions and Outlook

One of the primary aims of this study was the usage of a second perspective to confirm the veracity of the α-h fitting method. Of the 151 tracks that were viable for visual comparison, 40 (26.5%) were excellent match, 65 (43%) were maybe match, and 46 (30.5%) were no match. Overall, we find good agreement in the co-alignment of tracks to loops observed in EUVI; approximately 70% of our tracks had some feature to which we could align them. This finding lends a novel line of support in favor of the fidelity of the α-h fitting method. As to the remaining 30% that did not seem to correspond to any features in the corona, to first order we might expect these "missing" features to indicate that the α-h fitting went awry in the construction of tracks.

However, this conclusion relies on the assumption that loops in the corona are monolithic objects, existing and observable from varying vantage points. We cannot discount the possibility that the track is an accurate fit, but due to factors like anisotropic expansion, we do not see enough of a density enhancement in the alternate LOS for the loop to be visible.

We also contend that four of the 13 loops deemed suitable for the quantitative analysis of their diameters within this study are consistent with elliptical cross sections, as defined from having a negative correlation in the behavior in both the diameter–diameter and diameter–intensity comparisons. Of the remaining nine loops, four exhibited correlated behavior in both comparisons, and five had a combination of correlated and anticorrelated behavior.

The results of Section 3.5.3 point to systematically larger diameters observed from EUVI compared to those viewed from AIA. An optimist would point to this as evidence of smaller diameters from AIA compared to EUVI, similar to the idea from Malanushenko & Schrijver (2013) of preferential loop expansion along the AIA LOS for this case. We note the AIA LOS (and Sun–Earth line) is itself not particularly special; however, it corresponds to the $\hat{r}$ direction and both EUVI LOSs are perpendicular to that. This could be investigated in the future by looking at loops that lie at disk center in EUVI and on the limb from AIA. A more likely explanation, however, is instrumental effects between EUVI and AIA playing the more influential role in the diameter differences. This is evidenced by the median diameter ratio statistic for all tracks we analyzed quantitatively being comparable to the ratio of the two different instrument's plate scales. Further, the coarser resolution of the EUVI instrument, combined with the overlapping of loops due to the above-the-limb orientation of the region of interest, may have contributed to an overestimation of loop diameters that our methodology could not remedy. A small dip in the intensity/radius profile might indicate a "boundary" between two overlapping flux tubes but might be ignored by our straightforward Gaussian fitting. Improving on the techniques described in this study may remedy some of the issues described above, particularly, for example, by the application of a machine-learning or Markov Chain Monte Carlo method. These more complex techniques could, in theory, compensate for the sparsely gridded information and overlapping of fine, subresolution strands of flux.

We find a fair amount of anticorrelation (determined by a negative Spearman's ρ)

between EUVI and AIA diameters. One might expect some amount of correlation between the two properties if we were truly looking at a monolithic object, even for diameters consistently larger in one instrument than the other. That is, it might be expected that a loop's major and minor axes scale proportionally. However, this has not been the case for the track/loop pairs analyzed in this study.

One possible explanation is a type of mechanism wherein, during loop expansion, the major and minor axes change in an inversely proportional manner. This type of relationship between the axes is one that would would yield the anticorrelated diameter trend we have seen and point to a changing aspect ratio along these loops. It is also possible that the loop's cross section has a constant aspect ratio with the ellipse rotating about its center (e.g., as in a twisting ribbon). Either idea is bolstered by the findings of anticorrelated behavior between the intensity (Gaussian peak) and FWHM of our fitting procedure as detailed in Section 3.5.4. This is despite the conflicting results in the intensity–diameter comparison between this work and that of Klimchuk & DeForest (2020), which may speak to different populations of loops existing in the solar atmosphere. Indeed, the data differ between the two studies in both observational wavelength (193Å vs. 171Å) and length. Our results thus appear consistent with the hypothesis that some loops are monolithic objects with elliptical cross section, though we note that this is but one proposed explanation.

Nevertheless, this poses new questions for what physical process might lead to this behavior, if such behavior is even a real property of a structure that exists, or if we are — like in the traditional STEREO stereoscopy — identifying coinciding features merely because they are there. Perhaps the structure of loops in the corona are even more different than we might expect from the common conceptions in the field.

3.7 Acknowledgments

This work was supported by NASA's HGI program.

We would like to extend our thanks to the anonymous referees for the valuable input in regard to the improvement of this work.

CHAPTER FOUR

TEMPERATURE EVOLUTION OF CORONAL FLUX OBSERVED THROUGH MULTIPLE EXTREME ULTRAVIOLET WAVELENGTHS

Contribution of Authors and Co-Authors

Manuscript in Chapter 4

Author: Marika I. McCarthy

Contributions: Conceived, developed, and implemented study. Wrote manuscript.

Author: Dana W. Longcope

Contributions: Helped to conceive study. Provided feedback on manuscript drafts.

Author: Jada Walters

Contributions: Prepared data set of the 211 Å observations.

Manuscript Information

Marika I. McCarthy, Dana W. Longcope, and Jada Walters

The Astrophysical Journal

Status of Manuscript:
_X_ Prepared for submission to a peer-reviewed journal
____ Officially submitted to a peer-reviewed journal
____ Accepted by a peer-reviewed journal
____ Published in a peer-reviewed journal

Abstract

Coronal loops are the manifestation of magnetic fields in the solar corona. We assume that, in the environment of two adjacent active regions (ARs), each AR is itself its own magnetic system. Thus, the two can only come into contact post-emergence in the corona, and any newly formed flux linkage between the two should be observed as interconnecting loops. Therefore, by looking at loops between AR pairs we can quantify magnetic reconnection, the process believed to be behind those loops' formation. Further, loops are believed to be impulsively heated during their formation and should therefore be visible at progressively lower temperatures as they cool. This cooling behavior is well known through various light curve analyses (e.g., in flares) but would be present in quiescent loops if they are heated in this way, for example by nanoflares. Here we test this hypothesis by looking for each loop interconnecting a quiescent AR pair to cool through multiple temperatures. In previous work, we created a catalog of coronal loops interconnecting two ARs using AIA images in 171 Å. We perform our search by extending the previous catalog of coronal loops into other wavelengths. We find evidence for two different populations of loops. One population contains those newly reconnected. The other, whose loops have subsequently become bright once more, perhaps having undergone a relaxation process.

4.1 Motivation and Background

The coronal heating problem — the dramatic increase in temperature when rising from the solar surface into the atmosphere — is well-known within solar physics. One proposed heating mechanism is through small scale heating events called nanoflares. These are named in part after the traditional solar flare. A feature of a typical flare that these nanoflares would be expected to mimic is cooling of the plasma (after an impulsive heating phase), perhaps observed through successively cooler observational wavelengths. Analysis of the Bastille Day flare event by Aschwanden & Alexander (2001) revealed cooling behavior from temperatures of 30 MK to 1 MK. The analysis therein relied on the premise that the light curve from the aggregated behavior of many coronal loops over the observational field of view would behave like that of a single loop.

This cooling behavior has been documented outside of solar flares, as well. Viall & Klimchuk (2011, 2012, 2017) have made extensive use of the Atmospheric Imaging Assembly aboard the Solar Dynamics Observatory (AIA/SDO; Lemen et al., 2012) in their investigation of cooling in active regions. AIA is particularly well suited for this kind of study, due to its ability to take data (images) in many different wavelengths simultaneously. Seven of these wavelengths are in the extreme ultraviolet (EUV), which is particularly useful for observing the hot coronal plasma. Viall & Klimchuk (2011) used light curves of various locations in the active region and analyzed the peaks across different passbands, which resulted in evidence of cooling at these locations. Subsequent work found similar behavior in the light curves on a pixel-by-pixel basis in a time series of images for an entire active region (2012), and that this behavior is widespread throughout active regions (2017). They attributed their results to nanoflare heating, perhaps by so-called storms.

These nanoflare storms would heat many sub-strands that comprise a single coronal loop at non-constant intervals (Viall & Klimchuk, 2011). In fact, the idea of nanoflare

heating in coronal loops is intimately related with the underlying substructure. The solar corona is a regime in which the plasma is directly aligned to the magnetic field, and as a result loops are considered direct manifestations of the coronal field (Rosner et al., 1978). A mismatch between observations of loop lifetime (i.e., how long they are visible) and the theorized cooling time for a monolithic (not composed of smaller parts) loop have led to the belief that loops are not actually monolithic, but are multi-threaded (Klimchuk, 2006). These sub-resolution threads, or strands, are heated impulsively, but not all at once. The superposition of these strands lead to observations of a single loop lasting longer than if it were a single object with a constant temperature across its cross section.

The work presented herein, in contrast to other studies, seeks to observe the cooling behavior of active regions not through light curves, but through the identification of individual loops as they are formed through reconnection. McCarthy et al. (2019, hereafter Paper 1) first cataloged a series of coronal loops using the 171 Å band pass of AIA. These loops connected an emerging active region with an existing one (AR11149 and 11147, respectively), and were first believed to be newly populating the magnetic domain of this interconnecting region in the corona post-emergence by reconnection. The overcounting of flux reported therein was then attributed to some of these loops undergoing Taylor relaxation, and becoming bright again as a result. This hypothesized re-brightening was caused not through their initial formation, but by a reconnection process internal to this sub-volume of the corona. This hypothesis seemed to explain the behavior in a single band, but needs to be tested using complementary observations from other temperatures in bands other than 171 Å. Through adding loops from other passbands to the the catalog presented in Paper 1, we aim to observe the cooling behavior of individual, reconnected coronal loops, and to perhaps obtain evidence that allows us to differentiate between flux that is newly reconnected and that which is undergoing relaxation.

This work is detailed in the following sections. Section 4.2 discusses the acquisition

of the complimentary data that supplements that of Paper 1, and the expectation of what we might see from these data based on a comparison of emission measure. We make the comparisons across the band passes in Section 4.3, using a variety of methods. A summary of our results and conclusions drawn are then detailed in Section 4.4.

4.2 Data Set Compilation

The initial data set in Paper 1 was compiled from the 171 Å channel of AIA. We apply the same methodology detailed in that work in order to add loops from the 193 Å and 211 Å AIA channels. Briefly, a strip of pixels was extracted along a virtual slit from a time series of images. Peaks in the intensity profile along the slit were used to identify loops that cross it. The peak intensity and full width at half maximum are used to characterize the loop. We also obtain information about the time of the loop's first and last appearance, from which we have its location and extent in time. Due to the complex nature of the active regions, we are unable to subtract a consistent background value from each of the many hundreds of loops in our sample. Most peaks are sufficiently strong that we do not expect this to pose a problem. Visual confirmation is the final step in our catalog compilation, to eliminate bright artifacts that are not interconnecting loops. (See Paper 1, for more details.) As in Paper 1, here we denote the time of emergence as 11 January 2011 20:01 UTC and consider an approximately 48 hr time interval post-emergence in which we wish to quantify newly reconnected coronal loops. We also retain the same cadence between successive images (1 min), and the same slit location across the three data sets.

In this study, we chose to limit our analysis of loops (across all three band passes) to those whose lifetimes were 10 min or longer. This duration cutoff is well under the RTV equilibrium (Rosner et al., 1978) cooling timescale of a loop observed in 171 Å that is 60 Mm in length (the median length found in Paper 1, from their modeling work) of $\tau_{171} = 50.3$ minutes. For a loop of the same length, these timescales are $\tau_{191} = 30.8$ minutes

and $\tau_{211} = 27.6$ minutes for the 193 Å and 211 Å wavelengths, respectively. We note however, there exists the possibility of loops which we will not include in this data set (see the shoulder to the lifetime histrogram in Paper 1, Figure 6). We find that choosing a minimum lifetime cutoff is an appropriate trade-off, considering the manual confirmation step (see Section 3.1 in Paper 1). Further, it is the primary aim of this work to make meaningful comparisons across passbands and we do not think a lifetime cutoff poses a large threat to that goal.

Though AIA contains seven EUV band passes (see Lemen et al., 2012), we limit this work to 171 Å ($\sim$ 0.6 MK), 193 Å ($\sim$ 1.6 MK), and 211 Å ($\sim$ 2 MK). The inclusion of the other channels would indeed extend the temperature coverage. However, the analysis would be complicated by the responses of these other band passes. If we are interested in seeing cooling plasma, it would be hard to disentangle observations of cooling material if we are unsure at which temperature the passband is responsive. Figure 4.1 (top) shows the temperature response function of all seven channels, normalized to each's peak response. These were obtained with the SolarSoft routine `aia_get_response` using keywords `/temp, /dn, and /chiantifix` (Freeland & Handy, 1998). Some channel responses are doubly peaked (e.g., 94 Å, 131 Å) or have a wide temperature response (i.e., 335 Å). Isolating different components of these passbands is possible, for instance by the method presented in Warren et al. (2012) to isolate the hot, Fe XVIII emission from the 94 Å channel. That particular emission temperature is more suited for studies of the flaring corona (Lemen et al., 2012), and as such we chose not to apply this methodology to include the Fe XVIII emission in this study.

The normalized response functions of channels chosen for this work are isolated in the bottom panel of Figure 4.1. (Note that the colors assignment of gold, brown, and magenta for the 171 Å, 193 Å, and 211 Å channels, respectively, persist throughout the body of this work.) These were chosen for their relatively single-peaked nature, and — from their peak response separation being relatively close — they form a sort of "step ladder" in temperature.

Viall & Klimchuk (2011), in their proposal of possible ordering of peak intensities through different nanoflare storm parameters, note that the 211-193-171 order is maintained for all reported combinations therein. Thus, we expect this is a good combination for our goals of quantifying individual loops cooling. We note that 193 Å is also sensitive to hot flare plasma (Lemen et al., 2012). However, because we are looking at a non-flaring, quiescent AR pair we do not account for the contribution from a hypothetical higher temperature plasma.

4.2.1 Synthetic Emission Measure Comparisons

The intensity I_p observed in passband p from optically thin, isothermal plasma at temperature T is

$$I_p \;=\; EM\, R_p(T) \quad , \tag{4.1}$$

where EM is the column emission measure, $\int n_e^2\, d\ell$, and $R_p(T)$ is the temperature response of the passband shown in Figure 4.1. A lower bound can be placed on the emission measure using the peak value of the temperature response $R_{p,\max}$ (see Figure 4.1)

$$EM_{\min} \;=\; \frac{I_p}{R_{p,\max}} \quad . \tag{4.2}$$

For a cooling loop, we expect I_p to peak when its temperature passes the maximum of $R_p(T)$, called T_p. In this case Equation (4.2) will be the true EM rather than simply a lower bound. Figure 4.2(a) plots, along the top, histograms of the peak intensity of each loop observed in each bandpass. In Figure 4.2(b), these histograms are converted to $EM_{\min}$ using Equation (4.2). It is clear that loops with cooler temperature (211 Å to 171 Å) have comparatively lower EM.

The monotonic temperature/EM relation can be understood in terms of loop cooling. Loop temperature decreases during cooling, leading to successive observation in passbands, p and p', peaking at different temperatures, T_p and $T_{p'}$ respectively. Assuming density scales

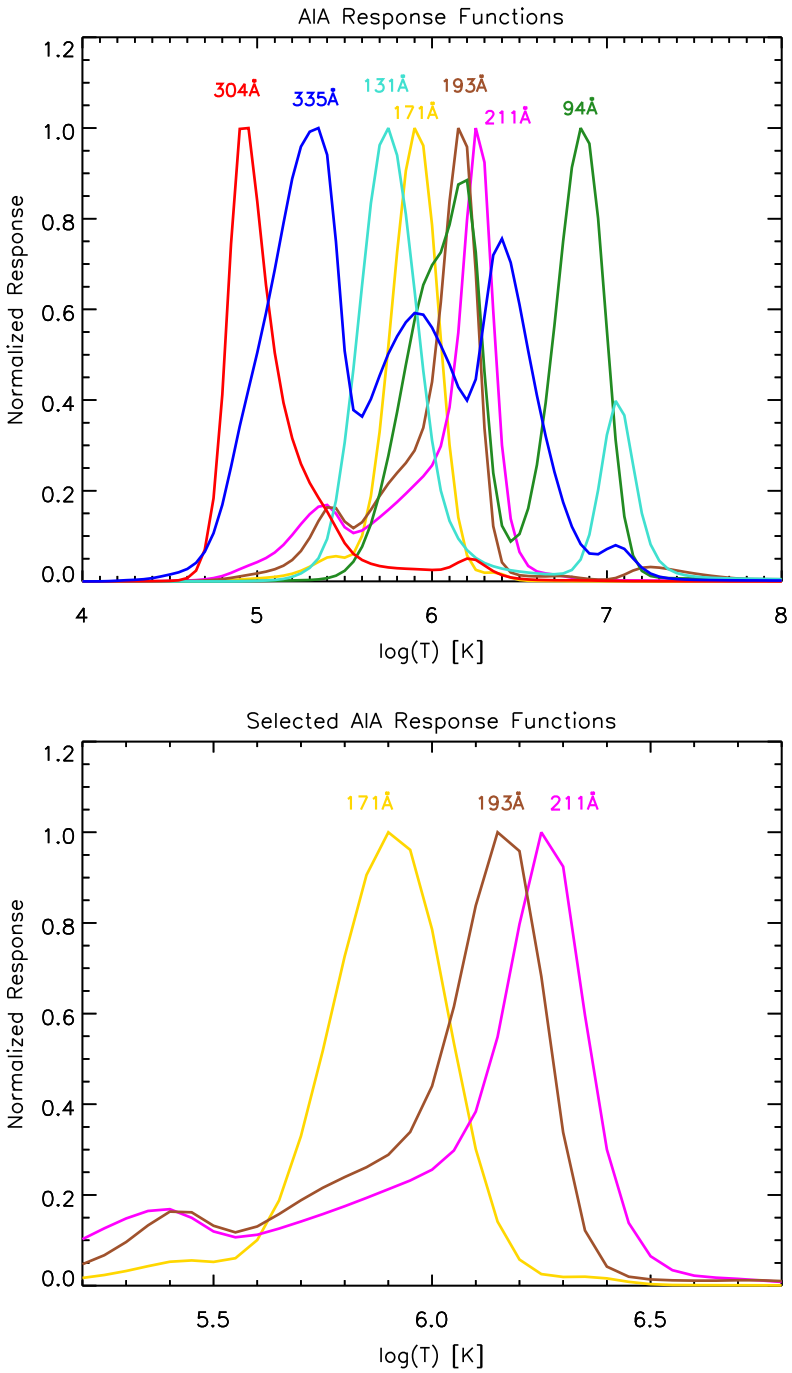


Figure 4.1: Temperature response functions of all AIA passbands (top) and those primarily used in this work (171, 193, and 211 Å; bottom). In both panels, the response functions has been normalized by peak response.

with temperature as $n_e \sim T^\nu$ leads to emission measure $EM_{p'} \sim T_{p'}^{2\nu}$. The observed intensity in pass band p' will be related to that observed in p according to

$$I_{p'} = \left(\frac{R_{p',\max}}{R_{p,\max}}\right)\left(\frac{T_{p'}}{T_p}\right)^{2\nu} I_p \quad . \tag{4.3}$$

Figure 4.2(c) shows all three intensity histograms converted using Equation (4.3) after choosing $\nu = 0.75$. That choice brings the histograms of 171 Å and 193 Å into reasonable agreement, meaning that they could be observations of the same loop population. It is notable, however, that the 211 Å histogram remains to the right of those two, suggesting a separate population of loops. The first population appears on the I_{211} axis (bottom) mostly below $I_{211} < 500$ DN/s, and would therefore be difficult to detect in that band even if they pass through that temperature ($T_{211} \simeq 2$ MK). Conversely, the 211 Å population appears above $I_{193} > 1000$ DN/s, and would be easily visible if they were there — they appear to be absent at $T_{193} \simeq 1.6$ MK. Further evidence of these two distinct populations is found from the histograms *vs.* x shown along the right of 4.2(a). The 171 Å and 193 Å histograms are relatively similar, spread mainly over $50 < x < 150$ arcsec, while the 211 Å loops are most visible over $120 < x < 180$.

The scaling exponent ν can assume different values depending on the nature of the cooling. Simulations of rapid, free cooling following flares (Cargill et al., 1995; Jakimiec et al., 1992) have been fit by $T \sim n_e^2$, meaning $\nu = 1/2$. On the other hand, if the loop cools slowly enough to maintain hydrostatic equilibrium its structure will conform to the RTV model (Rosner et al., 1978), $n_e \sim T^2$, meaning $\nu = 2$. The value $\nu = 0.75$, falling between rapid and quasi-static limits, was chosen empirically in 4.2(c) to bring the median intensities of 171 Å and 193 Å into agreement. The alternate choice $\nu = 1.5$, shown in Figure 4.2(d), brings together the median intensities of 193 Å and 211 Å, and in so doing brings the corresponding histograms into agreement. These are concentrated over $I_{171} < 500$

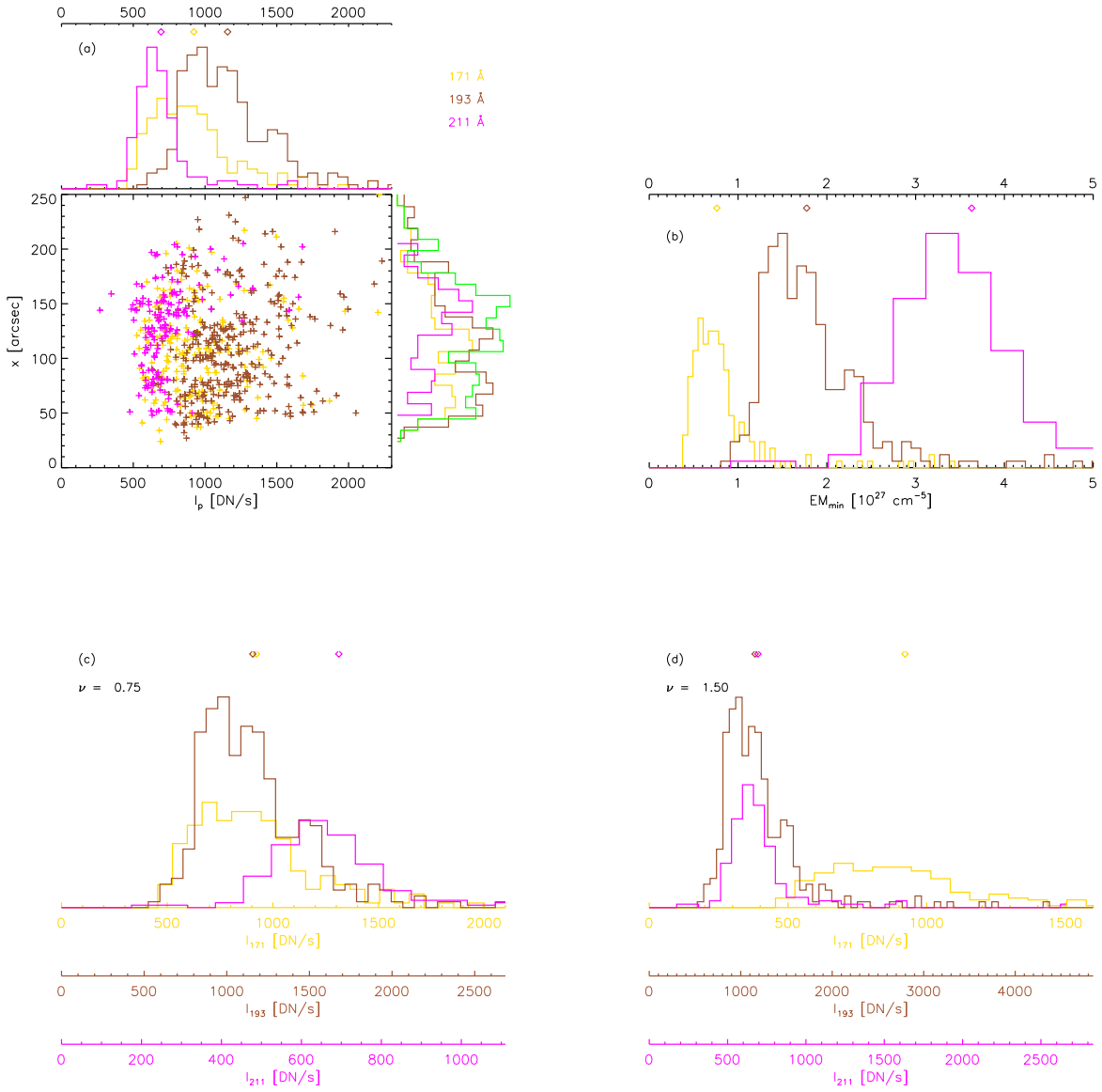


Figure 4.2: Characteristics of emission peaks identifying loops in each wavelength. (a) A scatter plot of the location (x) *vs.* peak intensity I_p, using colors for each AIA band. Histograms for each are plotted along the top (*vs.* I_p) and and the right (vs. x). Diamonds above the top histograms show the median value of I_p. A fourth histogram plotted in green along the right combines loops from the 171 Å and 211 Å observations. (b) The intensity histograms are converted to $EM_{\rm min}$ using Equation (4.2), plotted in units of $10^{27}\,{\rm cm}^{-5}$. (c) Histograms of each band, p (coded by the same colors), plotted against $I_{p'}$ using Equation (4.3) with $\nu = 0.75$. The same histogram can be read off each color-coded axis p'; doing so for $p = p'$ returns the original histogram shown atop panel (a). (d) Is the same presentation as panel (c), but for $\nu = 1.5$.

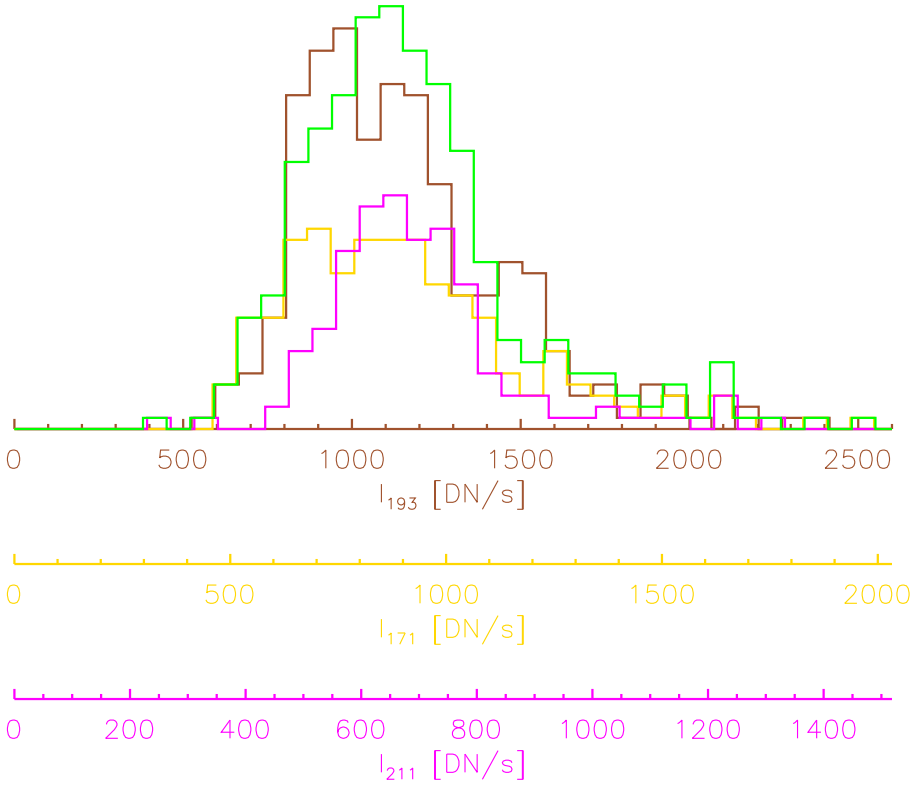


Figure 4.3: Histogram over I_{193} observed (brown) and synthesized from two population (green). The populations are found from loops observed only in 171 Å (gold) and 211 Å (magenta) and their intensities are converted to I_{193} using Equation (4.3) with $\nu = 0.75$ and $\nu = 1.5$ respectively. Reading these histograms against the axis of the matching color gives the version that appears along the top of Figure 4.2(a).

DN/s, and would thus be invisible in this cooler band. This alternate choice of cooling model appears to also argue for two distinct loop populations, although in this case, one population is visible only in 171 Å.

The discussion above motivates a synthetic histogram of 193 Å combining two distinct loop populations. Peak intensity values, I_{171} and I_{211} are converted to I_{193} using Equation (4.3) with $\nu = 0.75$ and $\nu = 1.5$ respectively. The histograms are shown in the colors of 171 Å, and 211 Å. We assume that loops identified in 171 Å are not observed in 211 Å, and *vice versa*. Paradoxically, both absences are explainable by low intensity ($I_p < 500$ DN/s) in that band. Based on this assumption we can sum the two population histograms to obtain the histogram plotted in green, which matches the observed 193 Å histogram reasonably well. The green histogram plotted along the right of Figure 4.2(a) shows that the spatial distribution of the combined distribution of the combined populations roughly conforms to that observed in 193 Å alone.

4.3 Comparisons Across Passbands

There are some straightforward comparisons we can make from the data obtained during cataloging. These data can be seen in Table 4.1, where we have listed the number identified, diameter (median value of all loops' median diameters; in arcsec), and median lifetime (time observed; in minutes).

We first compare the number of identified loops between each band pass, and find that there is an uneven distribution of identified loops across the three. The hot (193 Å) channel contains the most loops, followed by the warm (171 Å) channel, with the very hot (211 Å) one containing the least. If we are still operating under the assumption that each loop is impulsively heated, perhaps what we are seeing are two populations in temperature. The first population consists of loops that are heated to above 2 MK and either never cool to 0.6 MK or are invisible when they do. The second includes loops that are heated above

Wavelength	Temperature (MK)	Number	Diameter (median; arcsec)	Lifetime (median; minutes)
171 Å	0.6	205	9.0	21
193 Å	1.6	322	8.4	20
211 Å	2.0	151	11.4	22

Table 4.1: Properties of loops identified in each of the three band passes, as determined from the cataloging procedure.

1.6 MK (but not 2 MK) and then cool to temperatures below 0.6 MK. The idea of two populations is interesting, and could explain the overcounting of flux identified in Paper 1 that was attributed to Taylor relaxation. One population might be newly reconnected flux that first populates this interconnecting domain, while the other is that which has already undergone reconnection but is now moving towards a lower energy state. When putting the identified loops and their locations onto a time-space stack plot (i.e., built from stacking the virtual slits from images into one plot) as in Figure 4.4, the 171 Å and 193 Å loops appear at concurrent locations, in both time and space. This is also evident at other instances, where a separate set of loops appear at the same locations and times in both 193 Å and 211 Å. In contrast, there are few instances of 171 Å and 211 Å loops existing together in this way.

There are similar trends in loop lifetimes across all channels. This is in both in extent and distribution of lifetimes as reported in Paper 1 (see their Figure 6). We also note that, as in Paper 1, the introduction of a minimum-lifetime cutoff might have some effect on our statistics.

We might expect loops to be thinner in the 171 Å channel. They appear "sharper" and better defined in this passband. In fact, there does seem to be a "smearing" in the diameters from the diffusivity of loops in the 211 Å channel. Puzzlingly, the 193 Å loops have a smaller median diameter than those in 171 Å. We note that this passband was

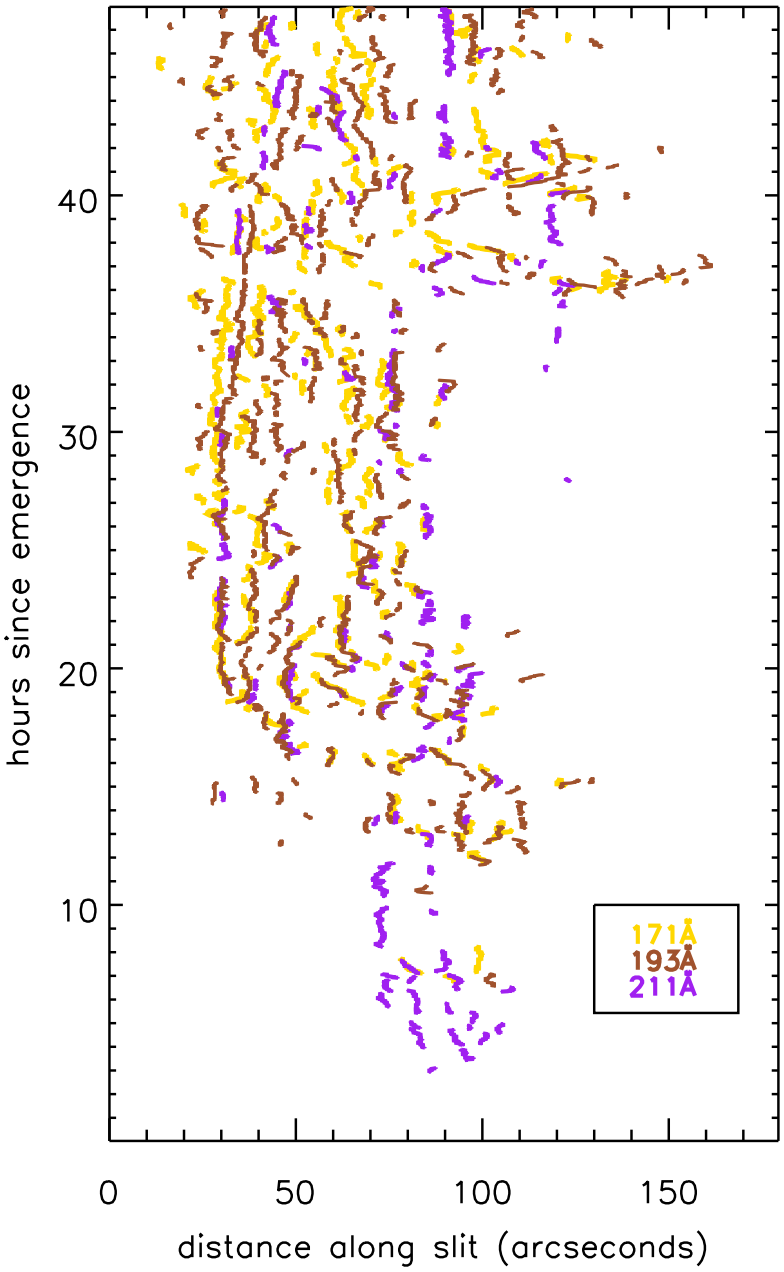


Figure 4.4: Time-space stack plot showing the loops identified from the 171 Å, 193 Å, and 211 Å channels (gold, brown, and magenta, respectively).

plagued by very diffuse emission, which in some ways might interfere with the fidelity of our cataloging procedure (e.g., considering the diffuse emission a persistent background, and the intensity peaks above that would seem narrower as a result). As a result, we might be underestimating this particular parameter in this wavelength. Thus, analysis of diameters (and those properties subsequently derived from them) must be undertaken very carefully.

The visual confirmation step of the cataloging procedure revealed some differences in the general morphologies of loops observed across the three channels. These are demonstrated in Figure 4.5. We compare their footpoint locations, according to the labeling schema of Longcope et al. (2020, see their Figure 4(b)), which has been reproduced in the top panel of our Figure 4.6. In this panel, positive (negative) polarities have the label prefix P (N) and are shown in blue (red). Figure 4.6 also includes a schematic in the bottom panel that demonstrates the general trends we will now describe. The 171 Å image in the top panel of Figure 4.5 seems to connect between polarities P08 and N10/N37 (as labeled in Longcope et al., 2020, and Figure 4.6). This connection is well below the separatrix (see Longcope et al., 2020, Figure 7). The 193 Å image (Figure 4.5; middle panel) has similar loops to those mentioned previously, but consistently exhibit long-lasting features that interconnect P07 to N36. This is closer to the separatrix (see again Figure 7 in Longcope et al., 2020). There is a general diffusivity of the loops observed in the 211 Å band pass throughout this interconnecting region, with some enhancement at the location of the aforementioned P07/N36 loops. This band pass also contains loops that connect the large sunspot denoted N01 to P13 and P24 (Figure 4.5, bottom) which does not seem apparent in either of the other channels. These loops appear to arch over the location where the 171 Å loops (P08-N10/N27) might occur. It is not apparent, even in movies of these data, that those sorts of loops exist in the 211 Å band pass. This, however, may be attributed to the general diffusivity of the structures in these images. That is, they may exist, but are not immediately apparent in observations with this band pass.

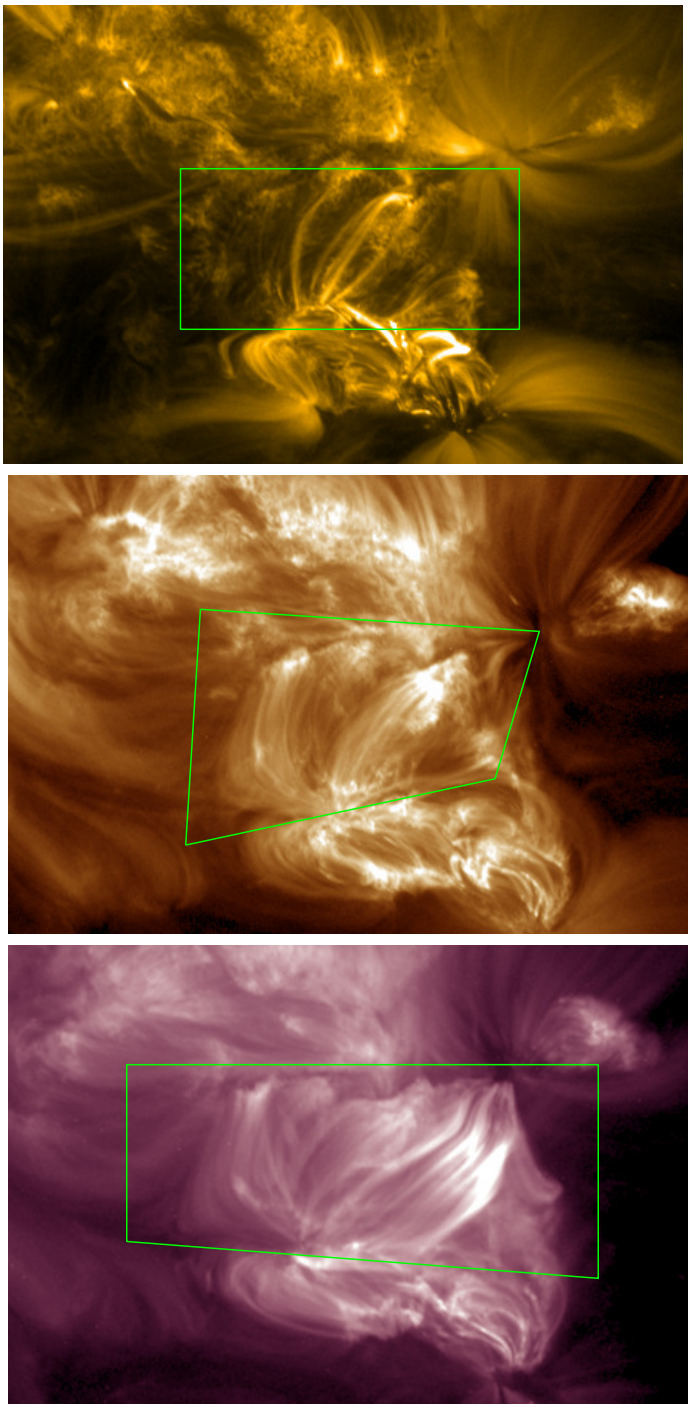


Figure 4.5: Some examples of the general trends with respect to morphological differences between the 171 Å (top), 193 Å (middle), and 211 Å (bottom) band passes. The loops of interest in this interconnecting domain are boxed in green for clarity. Note that these images are not taken concurrently, nor are the shape of the boxes meant to convey any information besides general area of interest.

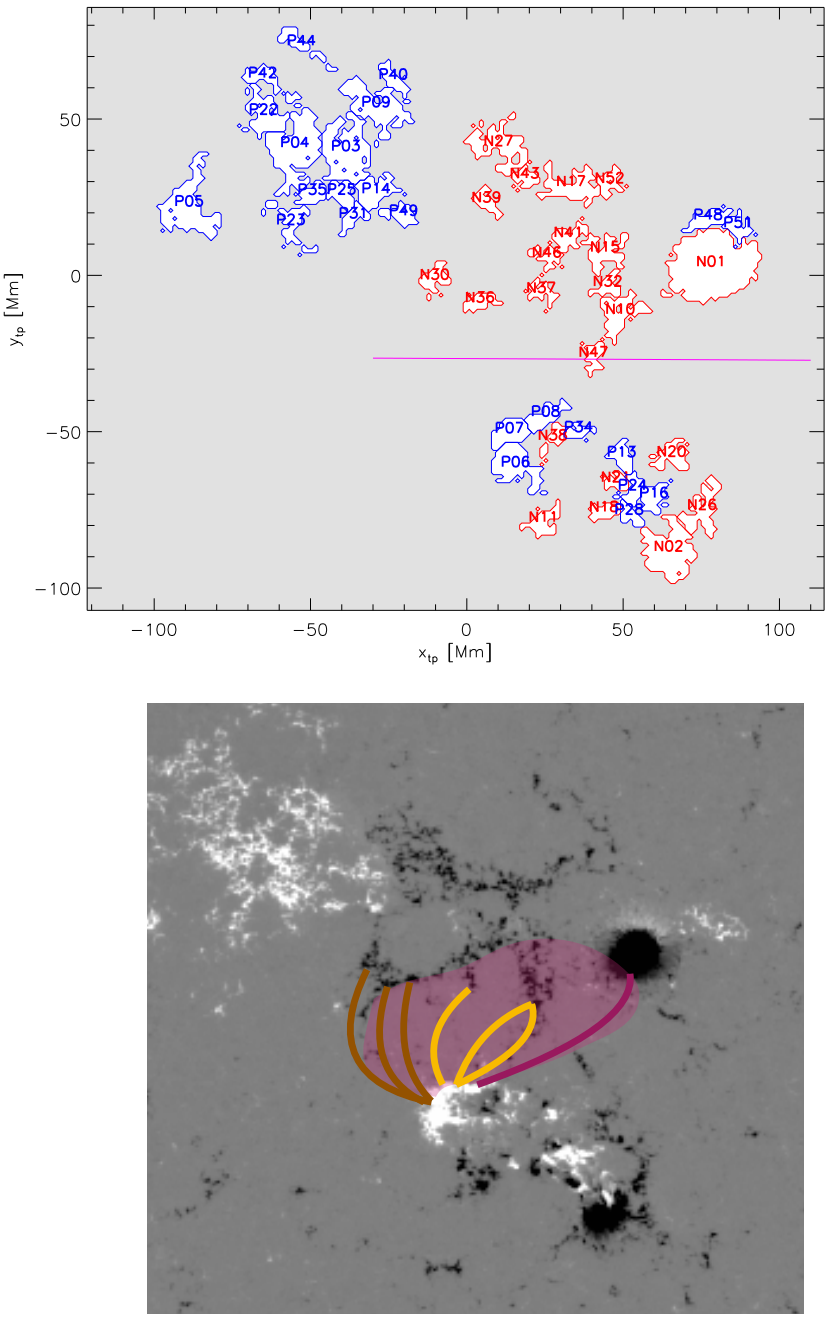


Figure 4.6: (Top) Labeling schema of Longcope et al. (2020, reproduced from that work's Figure 4b), used to identify the various polarities on this active region pair. The magenta bar shows the location of the virtual slit for this instance in time. Locations of strong positive (negative) photospheric flux are outlined in blue (red). (Bottom) Schematic example of the different morphological trends observed in Figure 4.5.

In these general observational trends of the EUV images there is additional evidence that the two populations of loops can be observed together in the 193 Å pass band. Loops between P08 and N10/37 (as in the 171 Å channel) are visible here, as are those that interconnect P07/N36 (also visible in 211 Å). Though there are these similarities in loop morphology between the hotter bands, there are still the loops viewed in 211 Å that interconnect P13/P24 to N01 which seem to be exclusive to this band pass.

4.3.1 Time Delay

From our data, we can also make comparisons of an apparent delay between emergence and reconnection. This delay was first studied by Longcope et al. (2005), who observed an approximately 24 hr time interval between emergence and the onset of the bulk of reconnection between a pair of ARs observed in 171 Å with the *Transition Region and Coronal Explorer* (TRACE; Handy et al., 1999). They attributed this to some threshold (e.g., a build-up of current) that must be reached before large amounts of flux can be transferred between magnetic domains. Zuccarello et al. (2008) also used the same TRACE band pass when they inferred a $\sim$ 12 hr delay after a new bundle of flux emerged amidst an AR. Tarr et al. (2014) analyzed a similar kind of event, of an AR emerging amidst a region of diffuse flux, but instead used a different wavelength (211 Å) and instrument (AIA) to obtain a delay of $\sim$ 11 hr. Kobelski (2014) used the *Sun Watcher with Active Pixels and Image Processing* (SWAP; Halain et al., 2013; Seaton et al., 2013), which had a band pass centered at 174 Å, to examine eight different adjacent emergence events. Those delays were around $\sim$ 25 hr, with a range from 13–72 (or more) hrs.

All of the studies cited above (and in Paper 1, as well) observed a delay informed by using a single EUV wavelength. The addition of the 193 Å and 211 Å data to that base catalog of Paper 1 adds a new layer of information. By looking at the appearance of loops in the time-space stack plot of Figure 4.4, we can quantify a delay between emergence and

loop formation (through reconnection) for each of the three channels. Paper 1 reported the delay observed in the 171 Å channel was $\sim$ 13 hr between emergence and the bulk of reconnection. The delay in this work for 193 Å loops is similar (see Figure 4.4). Again, this is more evidence of the relationship between the loops identified in the 171 Å and 193 Å channels, as first mentioned in Section 4.2.1 in regards to synthesized brightness. However, there is only a 4 hr delay when observing through the 211 Å channel. This difference in how soon loops appear could point to some fundamental partitioning of the loops in this study; e.g., related to the two-population idea proposed in Section 4.3.

Though the consensus in the literature seems to be time delays in reconnection are typically on the order of a day, a closer look lends credence to the idea that reconnection (loops) can be observed earlier with hotter wavelengths. The 211 Å observations support a shorter delay (4 hr here; 11 hr in Tarr et al., 2014) than those of 171/174 Å. In fact, the shortest delay reported by Kobelski (2014) is still longer than those reported with either of these 211 Å observations. Though we are limited by statistics, this does provide an avenue of investigation for future multiwavelength studies.

Both Longcope et al. (2005) and Kobelski (2014) described that the delays reported therein were between emergence and the *bulk* of reconnection; there did appear to be some signatures of reconnection earlier. This is also the case for the results of Paper 1. When supplementing those data with the two additional wavelengths herein, we find that the 193 Å data does exhibit some of that same behavior. That is, both the 171 Å and 193 Å observations exhibit some early evidence of interconnecting loops. These mostly solitary loops in the cooler channels appear at the same time as the bulk of reconnection has already begun in the 211 Å band pass. Longcope et al. (2005) did propose that they were not seeing hotter loops in their study to explain their undercounting of reconnected flux. The fact that hotter loops appear to consistently reconnect (and thus, appear) much earlier than loops in the other channels is again related to the idea of initial reconnection followed by relaxation,

as described in Paper 1.

Through this new lens, the buildup of electric current hypothesized by Longcope et al. (2005) to explain the observed delay may not have as high a threshold as first posited. Indeed, Kobelski (2014) notes that the results reported therein are an upper bound on this reconnection delay, due to temporal and spatial limitations of SWAP. Some studies have made efforts to characterize this threshold, including simulations by Galsgaard et al. (2007). That study found relatively constant rates of reconnection, but could not be directly compared to Longcope et al. (2005) as the simulation covered only ~ 20 minutes. They do note, however, that the rates found in that work provided a lower bound (Galsgaard et al., 2007). Though a possible delay in this simulation is still shorter than the four hour delay here (211 Å data), it might speak to the discrepancies between simulation and observation not being as vast a chasm as originally thought.

4.3.2 Flux Budget Comparison

By using the identified diameters of the loops in the catalog in conjunction with a characteristic magnetic field strength, we can compare the flux budget of the loops across each of the different AIA channels. Diameters of loops can be turned into cross sectional areas. Generally, the loops observed in this study intersect the virtual slit approximately perpendicularly. As a result, we choose not to consider projection effects on the diameter that might be due to the intersection angle of the loop and slit. Then, cross sectional area is obtained from diameter, d, by

$$\pi \left(\frac{d}{2}\right)^2, \tag{4.4}$$

assuming the cross section is circular. It is commonplace to assume loop cross section circularity (Reale, 2014). However, we note that this presumption has recently undergone scrutiny (Malanushenko & Schrijver, 2013), with observational results varying in their degree of support either for or against (Klimchuk & DeForest, 2020; Kucera et al., 2019; McCarthy

et al., 2021).

The characteristic magnetic field strength used across all three channels is obtained through the modeling work in Paper 1 for the 171 Å loops. They used the method of Malanushenko et al. (2009), that has been shown to have a 70% fidelity from a stereoscopic study (McCarthy et al., 2021). Here, we use the median value of the field strength of all loops crossing the slit: $B = 39$ G. The resultant flux budgets are shown in Figure 4.7. Because we are using just one characteristic magnetic field strength, this is essentially a comparison of cross sections.

We can make the comparison between these area values and the area within the interconnecting region. To make such a comparison, we use the intersection of the separatrix surface with a plane defined by the virtual slit and the observational line of sight. The separatrix is determined from the modeling work done in Paper 1 (see their Figure 14). The area under this curve for a selection of instances in time is shown in Figure 4.7 (dashed line). Towards the beginning of the event (prior to the 171 Å and 193 Å exhibiting reconnection *en masse*), this area seems similar to the accumulated areas of loops in the 211 Å channel. The fact that loops seem to occupy more area in this cross sectional slice of this domain than is available — during the time period in which the 171 Å and 193 Å channels begin to exhibit signatures of reconnection — further implies the existence of two populations of loops. In fact, this seems like a signature of the two phases of reconnection that is partitioning these populations. First, loops initially populate the interconnecting domain before relaxing within this region.

This area comparison may be improved upon in the future by more magnetic modeling, to obtain true flux values. The method of Malanushenko et al. (2009) used in Paper 1 was novel, in that each field line can be fit to its own three-dimensional model. Doing this fitting for loops in the 193 Å and 211 Å channels would give an individualized value of B for each loop at the location of the virtual slit, and thereby a more accurate flux comparison. Instead

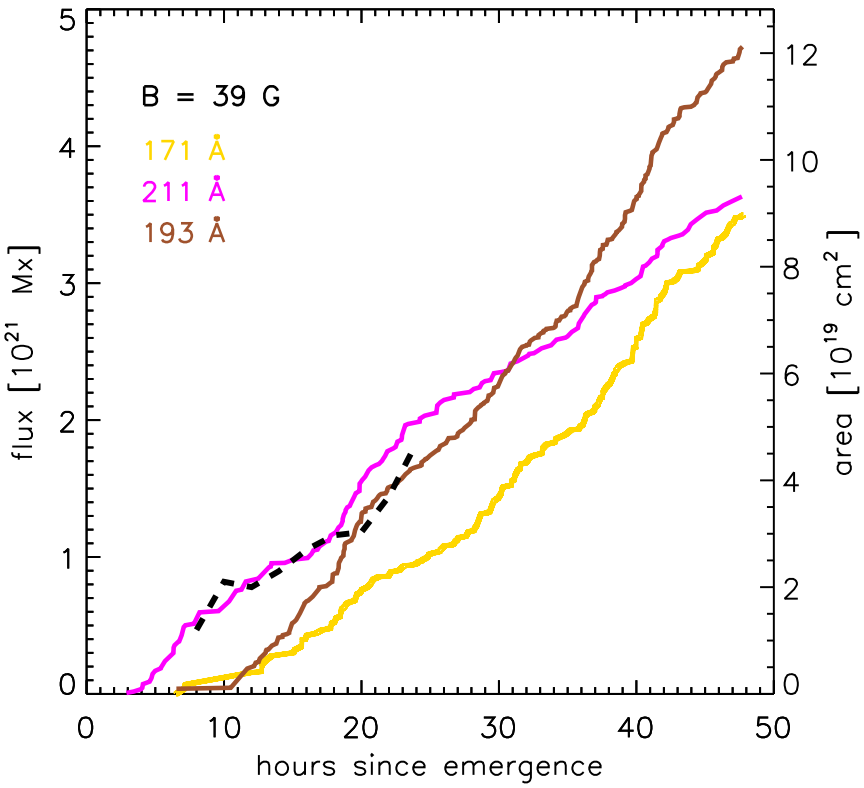


Figure 4.7: Flux budget comparison from the loops observed across the three different channels. These were obtained under the assumption of cross-sectional circularity with characteristic $B = 39$ G. The dashed line indicates the area under a cross section of the separatrix surface (informed by the modeling work in Paper 1, see that work's Figure 14)

of looking at trends in our flux budget, this would enable us to make direct, numerical comparisons. The real benefit of additional modeling lies in what differences may arise across our catalog, particularly with discrepancies between magnetic field strength of loops observed in different band passes. If it were found that loops observed with 193 Å and 211 Å have similar distributions of magnetic field strengths, we would not expect the results shown in Figure 4.7 to change significantly. Then, the additional modeling would be a minor improvement after extensive modeling. In a direct comparison of the 171 Å loops in the catalog, using the characteristic $B = 39$ G results a flux value that is approximately $80 - 90\%$ of the more sophisticated calculation.

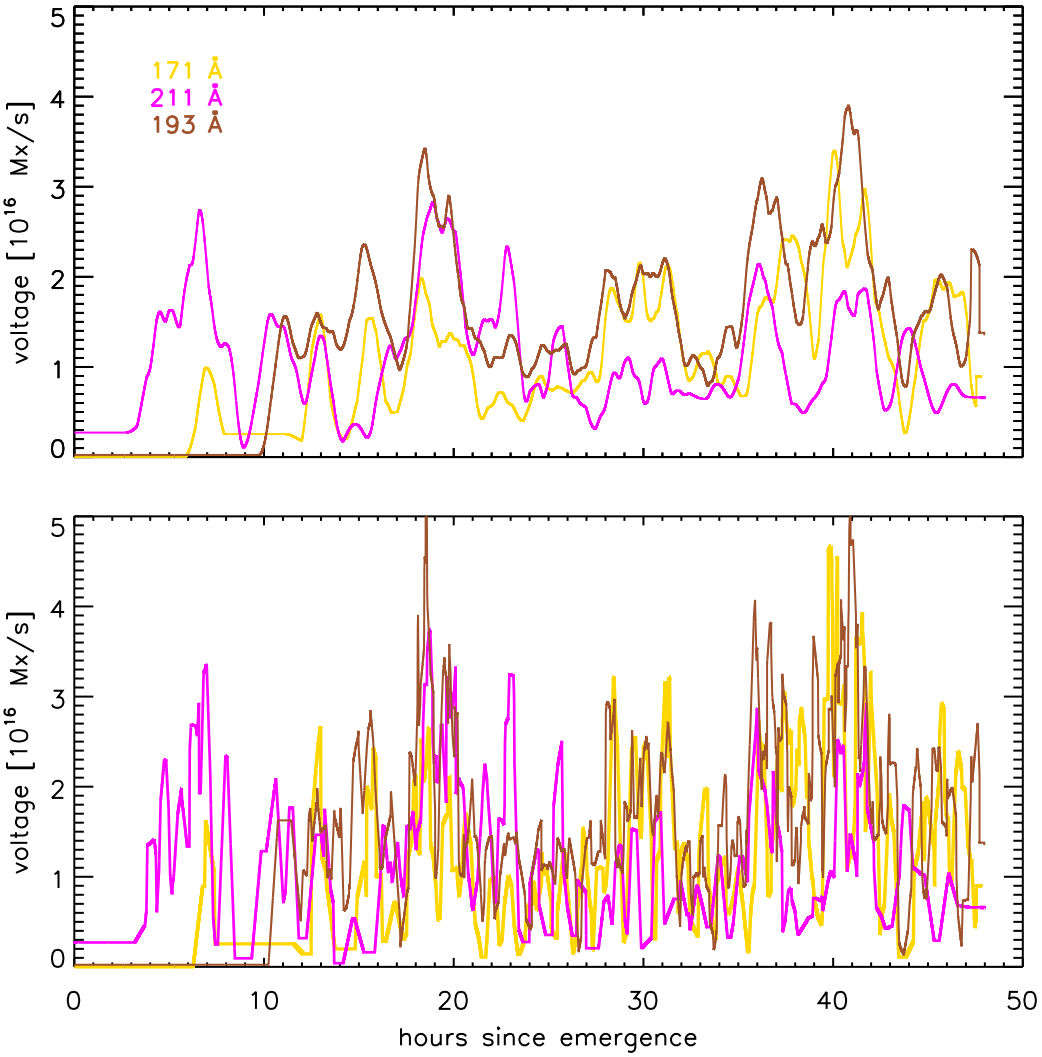


Figure 4.8: Voltage trends of the three band passes over the 48 hr time interval. The same data has been smoothed in two different ways, for clarity. The top panel was first smoothed over hour intervals and subsequently smoothed over the half hour. The data in the bottom panel was smoothed over the half hour only.

Comparisons of the flux budget confirms some of the initial conclusions about how the loops across temperature are related. It is not surprising that there is the most flux apparent in the 193 Å band pass; this wavelength observes the most loops. It may include loops also observed in one of the other band passes. As noted in Section 4.3, the uncertainties in the obtained diameters result in a careful and deliberate examination of the comparison between flux budgets. Thus, we note trends across each channel's flux budget rather than rely on quantitative comparisons. There are some similar phases in time, where there are particular bursts of apparent reconnection (e.g., 20 and 38 hr post-emergence). And, in further evidence for the related nature between them, the flux of 171 Å and 193 Å loops appear to trend together, starting about one day post-emergence.

Taking a time derivative of the data in Figure 4.7 gives us information about voltages over this event. Figure 4.8 shows such data. Both panels have boxcar smoothed the same data in different ways to eliminate some of the high-frequency variation. The top panel has been smoothed first over an hour interval and subsequently over an half hour, while the lower panel has been smoothed over an half hour only.

There are instances in which voltages from a certain channels react oppositely to the others. At $\sim$ 13 hr post-emergence (the delay identified in Paper 1 and Section 4.3.1) the voltages inferred from 171 Å and 193 Å data rise together while that from 211 Å acts inversely. Because of this inverse relationship, we can cite this as observational evidence of relaxing loops. Were we seeing loops that are initially populating the interconnecting domain and undergoing cooling, it would be expected that the voltages across all three band passes might trend together (e.g., as in 20 and 40 hr post-emergence in Figure 4.8). Similarly, there are also instances ($\sim$ 35 hr) where 193 Å and 211 Å rise together, slightly ahead of a voltage peak in 171 Å. In either of these instances, closer inspection could provide the additional insight that confirms the two populations as inferred from the voltage information. This closer inspection might be through detailed modeling of these loops, or by finer analysis of

a sub-selection of the data set.

4.3.3 Brightness Trends

If we expect one loop to be bright, and cool through all three of our identified passbands (an assumption that is, if not losing its credibility, at least starting to be questionable in this context), then we would expect brightening rates to look similar across the virtual slit. In order to perform this analysis, we create "brightness masks" from our stack plots. These brightness masks were made in order to combine the loops and their diameters to determine the extent of a loop's brightness throughout time and space. For these, we consider a pixel within our stack plot bright if it is within the loop's median radius from the identified loop location (i.e., peak in intensity) and assign it a value of 1. Then these plots consist of pixels that are valued at either 0 (not bright) or 1. Such masks can bee seen in Figures 4.9–4.11 (top panel) in black. The colored bars are the masked values for the loop's initial appearance. We sum the plots in the time direction to obtain the bottom panels of Figures 4.9–4.11. After summation of the black masks, the data is divided by the total number of rows in the plot to give a brightness fraction along the slit (e.g., the fraction of the event where a bright loop encompassed that location on the slit). We obtain a brightening rate across the slit by summation of the colored bars and division by the number of hours in our event.

In further evidence for their relatedness, we see similar distributions in Figures 4.9 (171 Å) and 4.10 (193 Å), particularly with regards to $40''$ and $60''$ along the slit (see Figure 4.12). The general trends in brightness are markedly different than in the 211 Å data (Figure 4.11), whose major peak in both fraction and rate is located around $90''$ across the slit. Note that there is a small bump similarly at $\sim 100''$ for the 193 Å data (see Figures 4.10, 4.12). There is still some evidence for the interconnectedness between the two hotter channels, though 193 Å data does not appear to be as intertwined with the hotter passband as it is with 171 Å.

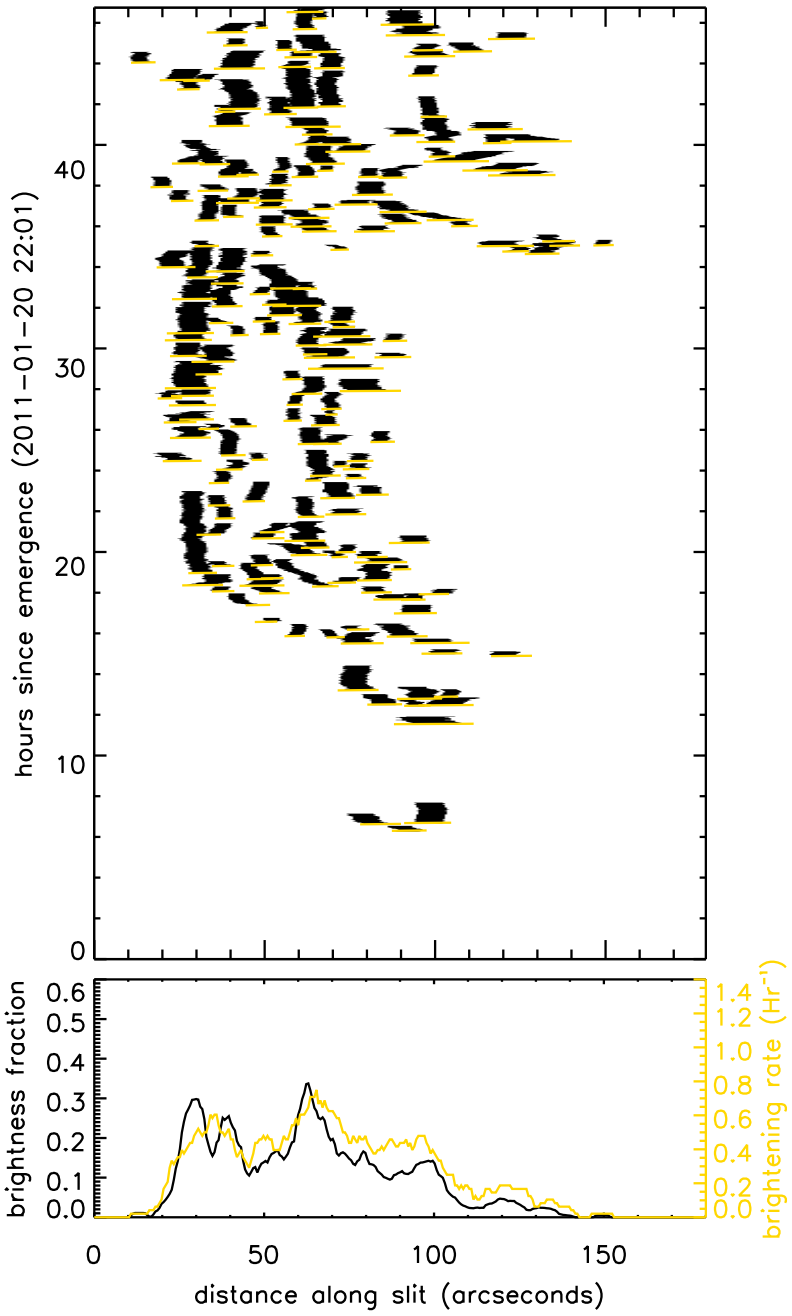


Figure 4.9: (Top) A version of time-space stack plot using the loops identified in 171 Å across the virtual slit. A mask of the data has been created (in black), to represent the spatial extent of each loop from its corresponding diameter information. The colored bars are the mask data for the instance of a loop's first appearance. (Bottom) Summation of the black and colored data in the top panel give the brightness fraction and brightening rate as a function of distance along the virtual slit.

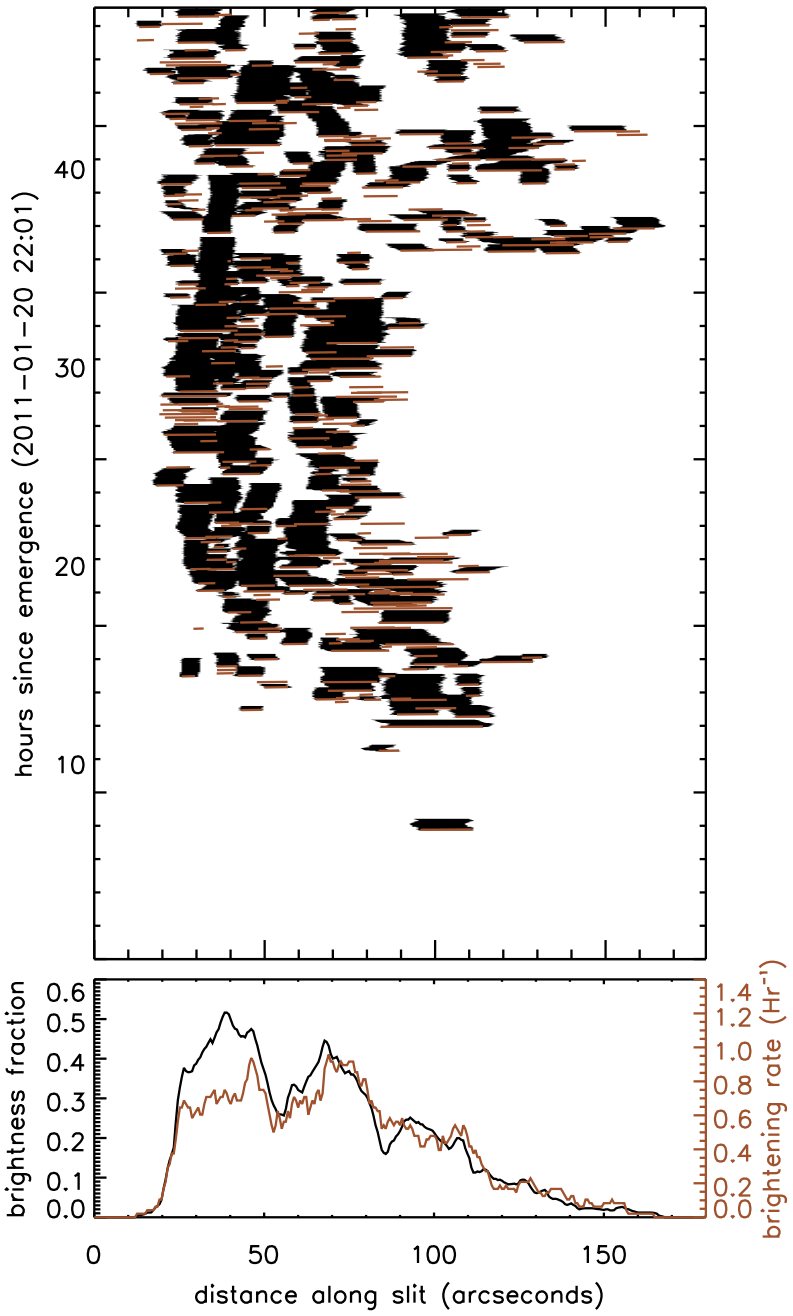


Figure 4.10: A figure similar to that of Figure 4.9, but for the 193 Å data.

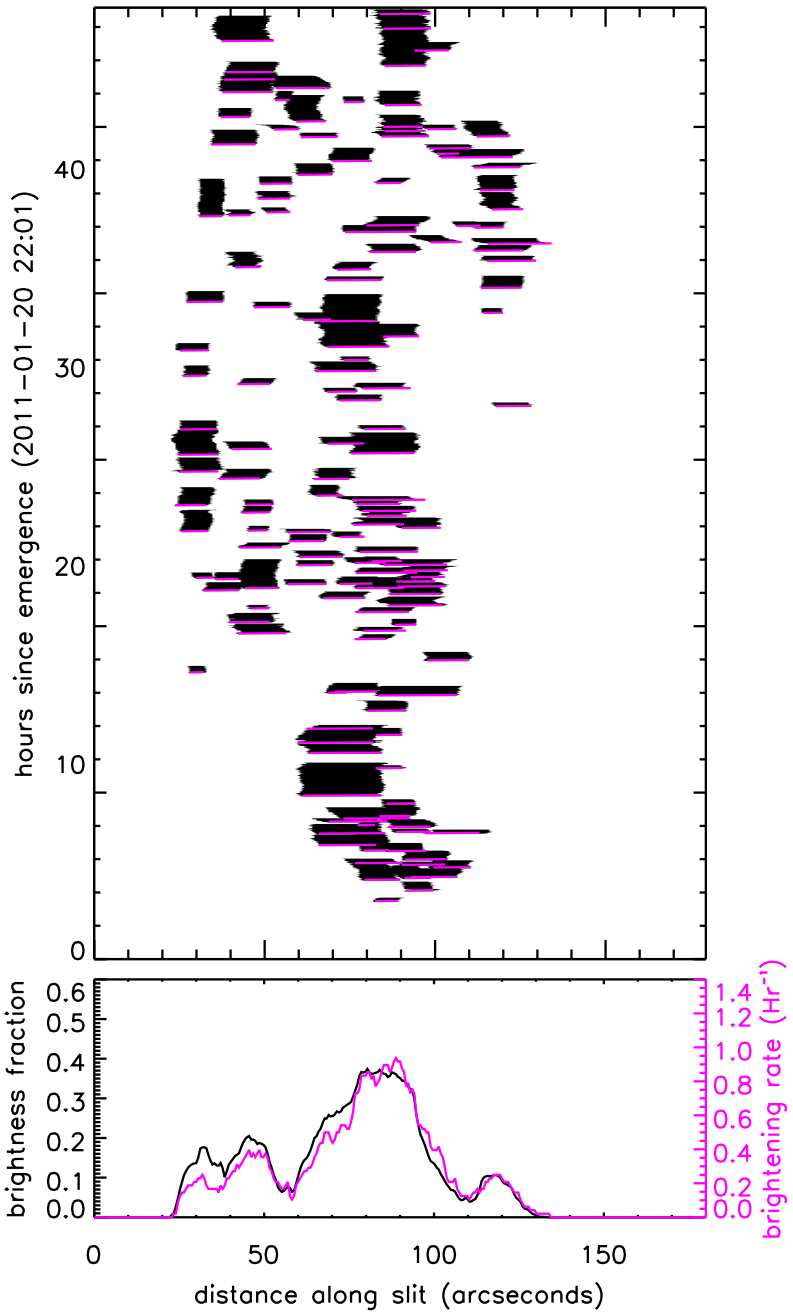


Figure 4.11: A figure similar to that of Figure 4.9, but for the 211 Å data.

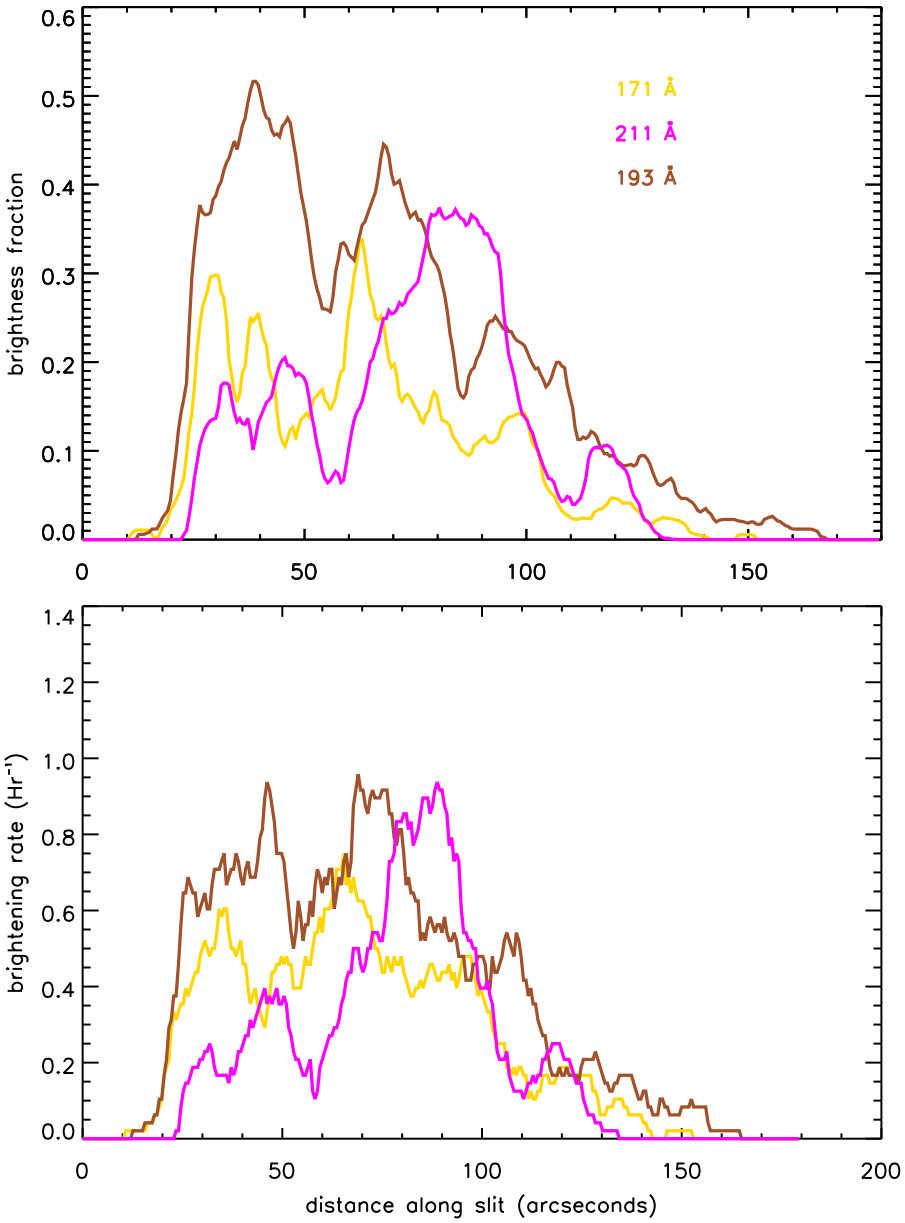


Figure 4.12: (Top) The brightness fraction from the bottom panels of Figures 4.9–4.11. (Bottom) The brightening rates found from Figures 4.9–4.11.

4.4 Discussion

The initial goals of this study focused on quantifying the cooling behavior of coronal loops, by attempting to identify individual loops as they cool through successive AIA passbands. The results presented herein speak to whether the temperature (cooling) trends are identifiable in individual loops. Namely, we do not see such clear cut cooling for whole structures as some studies do when focusing on either aggregates or smaller portions of the data. Instead we find evidence for two loop populations on the basis of temperature, lending credence to the idea proposed by Paper 1 of loops becoming bright after they have initially been reconnected to connect the two active regions.

Statistics compiled from our catalog support the two-population idea. Given that many more loops are found in the middle-temperature, the data suggest hot loops do not cool completely into 171 Å and cool loops do not get heated to 211 Å temperatures. This partitioning based on temperature of these two populations may be related to their morphologies. Differences in where loops from different temperatures appear to be anchored at the solar surface further extends the idea of loops that are initially formed between the active region pair, and can be subsequently reconnected (or, relax to lower energy state) to other domains that are also within the interconnecting region. Additional evidence is also found in comparison of the flux budgets, voltages, and trends in brightness across the three AIA band passes.

The creation and analysis of synthetic intensities presented in Section 4.2.1 also give credence to two populations of loops. The choice of scaling exponent, ν, can align the 193 Å data with the data from one (but not both) of the other channels. That is, there is no single choice that will bring the data in agreement across all three band passes. In fact, choice of either of the scaling exponents to bring the data from bandpass A in line with that from B leads to the synthetic emission of C being below the typical brightness enhancements seen

in A when cataloging these loops. In this way, evidence for the partitioning of loops in our data set is enhanced through this modeling.

Though we have found compelling evidence for the two-population hypothesis for this event, any conclusions drawn herein would benefit from both depth and breadth of future work. More magnetic modeling work, particularly of the 193 Å and 211 Å portions of the catalog, would lead to a better flux budget comparison. The work here used a characteristic magnetic field strength, as informed by the work of Paper 1. Additionally, by looking at properties of the resultant fitted loops in the 193 Å and, particularly, the 211 Å channels, we would further investigate whether we really have two different populations of loops in this interconnecting region.

This work centers on the loops between only one pair of active regions. It would be valuable to perform a multiwavelength, statistical study of coronal loops between other pairs of this type. By choosing these loops specifically, we know that all loops must be formed through reconnection post-emergence in the atmosphere. It is then a separate task to identify the newly formed loops in this region. In this type of laboratory, the prevalence of rebrightened loops can be further analyzed. These results would allow us to elucidate whether these two populations possess differences in their fundamental properties, based on the whether they initially populate the domain or become bright through an internal reconnection process. These results may be extended to flux emergence and incorporation into the existing coronal field as a whole.

CHAPTER FIVE

CODA

The work described herein analyzed an active region pair to elucidate magnetic reconnection, using newly formed loops between the pair as evidence of that process. The close examination of these particular loops — through cataloging them, investigating them from two perspectives, and observing them through multiple wavelengths — have revealed some counterexamples to commonly-held beliefs in the field. These make one reconsider the assumptions we make about loops, like their intrinsic structure and the mechanisms believed to be behind their formation. Specifically, we have found support for non-circular loop cross sections and reached conclusions about impulsive heating of loops by reconnection. These include challenging the assumption that loops brighten only when newly reconnected; we have detailed that loops may also brighten as a consequence of internal reconnection processes (e.g., Taylor relaxation) and may lead to different loop populations.

At the inception of Chapter 2, we operated under the assumption that we observe loops brightening when a field line is newly reconnected and that flux first populates a domain. From the loops identified in the 171 Å channel of AIA in conjunction with a linear force-free field fitting performed on individual loops, we find more flux in this interconnecting region than is possible. As a result, we infer that we see flux brightening multiple times, including after it is initially reconnected. There is also the possibility that the fitting used was somehow faulty, which contributed to the overestimation of flux we observed.

The methodology detailed in Chapter 2 to identify coronal loops can further be refined for future studies. Advancement in data analysis techniques (e.g., machine learning, computer vision) allows for a more sophisticated extraction of loop properties from the image without reduction of the data.

Chapter 3 utilizes a second viewing perspective to perform stereoscopic observations of the same set of loops from Chapter 2. We sought to confirm the fidelity of our fitting in Chapter 3, and found good agreement (approximately 70%) between the three-dimensional tracks and underlying EUV features. Through this work, we also find evidence that challenges the common assumption of circular loop cross sections. The stereoscopic observations provide the opportunity to view loops from two vantage points, and we can compare their projected diameters. We find evidence of non-circular cross sections through several different anti-correlated behaviors. Thus, we posit that the remaining 30% of tracks that we could not assign to an EUV feature was not an obvious defect of our fitting method. Instead, we argue that it is possible loops' cross sections scale so anisotropically that they do not exist (i.e., are not observable) from this other perspective.

Though stereoscopic studies are common, the novelty of Chapter 3 is in usage of the second perspective to confirm our loop fitting, instead of construct it. There are many more events in the STEREO and AIA archives in which we can examine loops. This could include changing the angle between the LOSs. Further work would help illuminate which features the α-h fitting can reliably reproduce with high precision, as in the particularly well-fit track/loop pairs noted in Section 3.4

Chapter 4 tests the proposed idea that loops become bright not only when they are initially populating the interconnecting domain, but subsequently. To expand our loop catalog, we applied the methodology of Chapter 2 to data from the AIA 193 Å and 211 Å band passes. One might expect — if a loop is impulsively heated before cooling through different passbands — some commonalities across the entire catalog, no matter the wavelength used to observe. However, we find discrepancies — particularly that differentiates the 211 Å loops from the rest — which suggests the catalog is comprised of two different populations. This reinforces the idea introduced in Chapter 2, of observing a loop becoming bright once again.

The aforementioned improvements to extend the work of Chapter 2 would also benefit

from more multiwavelength studies. In fact, applying such techniques to wavelengths in which loops are not as well defined would be a great improvement, provided that the results can be believed.

Though this work has centered on a particular pair of active regions, these sorts of adjacent emergence events provide a laboratory that is rife with opportunity to investigate newly formed flux that is created through magnetic reconnection. Knowledge of flux emergence and of incorporation of this new flux into the existing coronal field would benefit from a series of follow-up studies. This new era of solar observations (with instruments like DKIST, PSP, and SO) can provide complimentary data, and might allow us to elucidate mechanisms behind these results. Further, though there is abundant data from Solar Cycle 24 that can be examined, there might be interesting new emergence events identified as we emerge from solar minimum into Cycle 25. Perhaps some combination of all these advancements will allow future studies to further challenge conventional assumptions of the field.

REFERENCES CITED

Alfvén, H. 1942, Nature, 150, 405

Aschwanden, M. J. 2011, Living Reviews in Solar Physics, 8, 5

Aschwanden, M. J., & Alexander, D. 2001, Sol. Phys., 204, 91

Aschwanden, M. J., Boerner, P., Schrijver, C. J., & Malanushenko, A. 2013, Solar Physics, 283, 5

Aschwanden, M. J., & Nightingale, R. W. 2005, ApJ, 633, 499

Aschwanden, M. J., Nightingale, R. W., & Alexander, D. 2000, The Astrophysical Journal, 541, 1059

Aschwanden, M. J., Nitta, N. V., Wuelser, J.-P., & Lemen, J. R. 2008, ApJ, 680, 1477

Barnes, G., Longcope, D. W., & Leka, K. D. 2005, The Astrophysical Journal, 629, 561

Berger, T., De Pontieu, B., Fletcher, L., et al. 1999, Solar Physics, 190, 409

Brooks, D. H., Warren, H. P., Ugarte-Urra, I., & Winebarger, A. R. 2013, ApJL, 772, L19

Cargill, P. J., Mariska, J. T., & Antiochos, S. K. 1995, ApJ, 439, 1034

Carroll, B., & Ostlie, D. 2017, An Introduction to Modern Astrophysics (Cambridge University Press)

Charbonneau, P. 2020, Living Reviews in Solar Physics, 17, 4

Chiu, Y. T., & Hilton, H. H. 1977, ApJ, 212, 873

de Ferrer, J. J. 1809, Transactions of the American Philosophical Society, 6, 264

DeRosa, M. L., Schrijver, C. J., Barnes, G., et al. 2009, The Astrophysical Journal, 696, 1780

Domingo, V., Fleck, B., & Poland, A. I. 1995, Sol. Phys., 162, 1

Eddy, J. A. 1976, Science, 192, 1189

Fan, Y. 2009, Living Reviews in Solar Physics, 6, 4

Fan, Y., Fisher, G. H., & McClymont, A. N. 1994, ApJ, 436, 907

Fisher, G., Fan, Y., Longcope, D., Linton, M., & Pevtsov, A. 2000, Solar Physics, 192, 119

Freeland, S. L., & Handy, B. N. 1998, Sol. Phys., 182, 497

Galsgaard, K., Archontis, V., Moreno-Insertis, F., & Hood, A. W. 2007, The Astrophysical Journal, 666, 516

Gary, G. A. 2001, Sol. Phys., 203, 71

Golub, L., & Pasachoff, J. M. 1997, The Solar Corona

Grigis, P., Su, Y., & Weber, M. 2012, AIA PSF Characterization and Image Deconvolution, Tech. rep.

Halain, J. P., Berghmans, D., Seaton, D. B., et al. 2013, Sol. Phys., 286, 67

Hale, G. E. 1908, ApJ, 28, 315

Hale, G. E., Ellerman, F., Nicholson, S. B., & Joy, A. H. 1919, ApJ, 49, 153

Hale, G. E., & Nicholson, S. B. 1925, ApJ, 62, 270

Handy, B., Acton, L., Kankelborg, C., et al. 1999, Solar Physics, 187, 229

Hathaway, D. H. 2015, Living Reviews in Solar Physics, 12, 4

Hawkins, G. S. 1963, Nature, 200, 306

Hayakawa, H., Owens, M. J., Lockwood, M., & Sôma, M. 2020, ApJ, 900, 114

Hill, F., Martens, P., Yoshimura, K., et al. 2009, Earth Moon and Planets, 104, 315

Jackson, J. D. 1998, Classical Electrodynamics, 3rd Edition

Jakimiec, J., Sylwester, B., Sylwester, J., et al. 1992, A&A, 253, 269

Kaiser, M. L., Kucera, T. A., Davila, J. M., et al. 2008, Space Sci. Rev., 136, 5

Klimchuk, J. A. 2000, Sol. Phys., 193, 53

—. 2006, Sol. Phys., 234, 41

Klimchuk, J. A. 2009, in Astronomical Society of the Pacific Conference Series, Vol. 415, The Second Hinode Science Meeting: Beyond Discovery-Toward Understanding, ed. B. Lites, M. Cheung, T. Magara, J. Mariska, & K. Reeves, 221

—. 2015, Philosophical Transactions of the Royal Society of London Series A, 373, 20140256

Klimchuk, J. A., & DeForest, C. E. 2020, ApJ, 900, 167

Klimchuk, J. A., Lemen, J. R., Feldman, U., Tsuneta, S., & Uchida, Y. 1992, PASJ, 44, L181

Kobayashi, K., Cirtain, J., Winebarger, A. R., et al. 2014, Sol. Phys., 289, 4393

Kobelski, A. R. 2014, PhD thesis, Montana State University

Kucera, T. A., Young, P. R., Klimchuk, J. A., & DeForest, C. E. 2019, The Astrophysical Journal, 885, 7

Lang, K. 2008, The Sun from Space, Astronomy and Astrophysics Library (Springer Berlin Heidelberg)

Lang, K. R. 2001, The Cambridge Encyclopedia of the Sun

Lemen, J. R., Title, A. M., Akin, D. J., et al. 2012, Sol. Phys., 275, 17

Linton, M. G., Dahlburg, R. B., & Antiochos, S. K. 2001, ApJ, 553, 905

Longcope, D., McCarthy, M., & Malanushenko, A. 2020, The Astrophysical Journal, 901, 147

Longcope, D. W. 1996, Sol. Phys., 169, 91

—. 2005, Living Reviews in Solar Physics, 2, 7

—. 2009, in Heliophysics: Plasma Physics of the Local Cosmos, ed. C. J. Schrijver & G. L. Siscoe (Cambridge University Press), 77–112

Longcope, D. W. 2017, Hydrodynamics and magnetohydrodynamics for solar and stellar applications

Longcope, D. W., & Magara, T. 2004, ApJ, 608, 1106

Longcope, D. W., McKenzie, D. E., Cirtain, J., & Scott, J. 2005, ApJ, 630, 596

Longcope, D. W., & Silva, A. V. R. 1998, Sol. Phys., 179, 349

López Fuentes, M. C., Démoulin, P., & Klimchuk, J. A. 2008, ApJ, 673, 586

López Fuentes, M. C., Klimchuk, J. A., & Démoulin, P. 2006, ApJ, 639, 459

López Fuentes, M. C., Klimchuk, J. A., & Mandrini, C. H. 2007, ApJ, 657, 1127

Lothian, R. M., & Browning, P. K. 1995, Solar Physics, 161, 289

MacTaggart, D. 2011, A&A, 531, A108

Magara, T., & Longcope, D. W. 2001, ApJL, 559, L55

Malanushenko, A., Longcope, D. W., & McKenzie, D. E. 2009, The Astrophysical Journal, 707, 1044

Malanushenko, A., & Schrijver, C. J. 2013, ApJ, 775, 120

Malanushenko, A., Schrijver, C. J., DeRosa, M. L., & Wheatland, M. S. 2014, ApJ, 783, 102

Malanushenko, A., Schrijver, C. J., DeRosa, M. L., Wheatland, M. S., & Gilchrist, S. A. 2012, ApJ, 756, 153

Malanushenko, A., Yusuf, M. H., & Longcope, D. W. 2011, ApJ, 736, 97

Maunder, E. W. 1904, MNRAS, 64, 747

McCarthy, M. I., Longcope, D. W., & Malanushenko, A. 2021, The Astrophysical Journal, 913, 56

McCarthy, M. I., Longcope, D. W., Malanushenko, A., & McKenzie, D. E. 2019, ApJ, 887, 140

Messer, R., & Straffin, P. 2006, Topology Now!, Mathematical Association of America Textbooks (Mathematical Association of America)

Moldwin, M. B., Siscoe, G. L., & Schrijver, C. J. 2009, in Heliophysics: Plasma Physics of the Local Cosmos, ed. C. J. Schrijver & G. L. Siscoe (Cambridge University Press), 139–162

Muñoz-Jaramillo, A., & Vaquero, J. M. 2019, Nature Astronomy, 3, 205

Nakagawa, Y., Raadu, M. A., Billings, D. E., & McNamara, D. 1971, Sol. Phys., 19, 72

Nandy, D., Hahn, M., Canfield, R. C., & Longcope, D. W. 2004, in IAU Symposium, Vol. 223, Multi-Wavelength Investigations of Solar Activity, ed. A. V. Stepanov, E. E. Benevolenskaya, & A. G. Kosovichev, 473–474

National Solar Observatory. 2020, NSF's newest solar telescope produces first images, `https://nso.edu/press-release/inouye-solar-telescope-first-light/`, NSO, AURA and NSF, accessed 24 April 2021

Parker, E. N. 1957, Phys. Rev., 107, 830

Parker, E. N. 1972, ApJ, 174, 499

Petschek, H. E. 1964, NASA Special Publication, 50, 425

Phillips, K. J. H. 1995, Guide to the Sun

Priest, E. 2014, Magnetohydrodynamics of the Sun, doi:10.1017/CBO9781139020732

Priest, E., & Forbes, T. 2000, Magnetic Reconnection: MHD Theory and Applications (Cambridge University Press)

Rachmeler, L. A., Winebarger, A. R., Savage, S. L., et al. 2019, Sol. Phys., 294, 174

Reale, F. 2014, Living Reviews in Solar Physics, 11, 4

Reeves, E. M., Noyes, R. W., & Withbroe, G. L. 1972, Sol. Phys., 27, 251

Rempel, M. 2009, in Heliophysics: Plasma Physics of the Local Cosmos, ed. C. J. Schrijver & G. L. Siscoe (Cambridge University Press), 42–76

Rosner, R., Tucker, W. H., & Vaiana, G. S. 1978, ApJ, 220, 643

Scherrer, P. H., Schou, J., Bush, R. I., et al. 2012, Solar Physics, 275, 207

Schou, J., Scherrer, P. H., Bush, R. I., et al. 2012, Sol. Phys., 275, 229

Schrijver, C. J., De Rosa, M. L., Title, A. M., & Metcalf, T. R. 2005, ApJ, 628, 501

Schrijver, C. J., & Siscoe, G. L. 2009, in Heliophysics: Plasma Physics of the Local Cosmos, ed. C. J. Schrijver & G. L. Siscoe (Cambridge University Press), 1–20

Seaton, D. B., Berghmans, D., Nicula, B., et al. 2013, Sol. Phys., 286, 43

Sheeley, Jr., N. R., Bohlin, J. D., Brueckner, G. E., et al. 1975, Sol. Phys., 40, 103

Solanki, S. K. 2003, A&A Rev., 11, 153

Space Weather Prediction Center. ????, Solar Cycle Progression, `https://www.swpc.noaa.gov/products/solar-cycle-progression/`, NOAA, accessed 25 April 2021

Spiegel, E. A., & Zahn, J. P. 1992, A&A, 265, 106

Sweet, P. A. 1958, Il Nuovo Cimento (1955-1965), 8, 188

Tarr, L., & Longcope, D. 2012, ApJ, 749, 64

Tarr, L. A., Longcope, D. W., McKenzie, D. E., & Yoshimura, K. 2014, Sol. Phys., 289, 3331

Taylor, J. B. 1986, Rev. Mod. Phys., 58, 741

Toriumi, S., & Takasao, S. 2017, ApJ, 850, 39

Tsuneta, S. 1996, ApJL, 456, L63

Tsuneta, S., Acton, L., Bruner, M., et al. 1991, Sol. Phys., 136, 37

Vaiana, G. S., Krieger, A. S., & Timothy, A. F. 1973, Sol. Phys., 32, 81

Valori, G., Romano, P., Malanushenko, A., et al. 2015, Sol. Phys., 290, 491

van Driel-Gesztelyi, L., & Green, L. M. 2015, Living Reviews in Solar Physics, 12, 1

Vaquero, J. M., & Vázquez, M. 2009, The Sun Recorded Through History: Scientific Data Extracted from Historical Documents, Vol. 361, doi:10.1007/978-0-387-92789-3

Viall, N. M., & Klimchuk, J. A. 2011, ApJ, 738, 24

—. 2012, ApJ, 753, 35

—. 2017, ApJ, 842, 108

Warren, H. P., Winebarger, A. R., & Brooks, D. H. 2012, ApJ, 759, 141

Watko, J. A., & Klimchuk, J. A. 2000, Sol. Phys., 193, 77

Webb, D. F., & Zirin, H. 1981, Solar Physics, 69, 99

Wiegelmann, T., & Sakurai, T. 2012, Living Reviews in Solar Physics, 9, 5

Winebarger, A. R., Warren, H. P., & Seaton, D. B. 2003, ApJ, 593, 1164

Wittmann, A. D., & Xu, Z. T. 1987, Astron. Astrophys. Suppl. Ser., 70, 83

Wuelser, J.-P., Lemen, J. R., Tarbell, T. D., et al. 2004, in Society of Photo-Optical Instrumentation Engineers (SPIE) Conference Series, Vol. 5171, Telescopes and Instrumentation for Solar Astrophysics, ed. S. Fineschi & M. A. Gummin, 111–122

Yamada, M., Ono, Y., Hayakawa, A., Katsurai, M., & Perkins, F. W. 1990, Physical Review Letters, 65, 721

Zeeman, P. 1897, Nature, 55, 347

Zuccarello, F., Battiato, V., Contarino, L., et al. 2008, A&A, 488, 1117